# *21th International Symposium on Plasma Chemistry*

*Cairns,* ***Australie, Aout 4 - 9, 2013***

***Précédentes éditions***

2011 : Philadelphia (USA)
2009 : Bochum (Allemagne)
2007 : Kyoto (Japon)
2005 : Toronto (Canada)
2003 : Tormina (Italie)
2001 : Orléans (France)

***Prochaine édition***

2015 : Antwerp (Belgique)

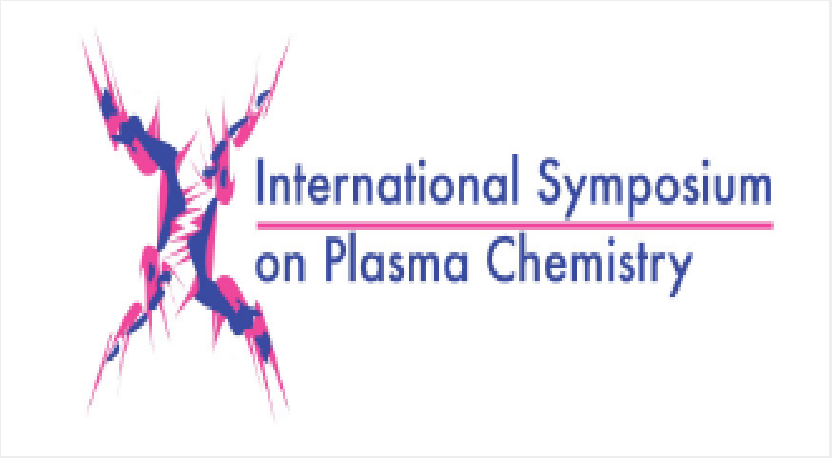


***Frais d'inscription*** : environ 580 €
***Durée du congrès :*** 5 jours

***1 école d'été***

***Fundamentals and applications of low pressure and high pressure plasmas (3 jours)***

1) Basics of arcs, Applications of arcs, Introduction to processing plasmas, Atmospheric pressure discharges
2) Bio-applications of plasmas, Plasma processing of polymers
3) Basic electric probes, Basic spectroscopy, Fast imaging spectroscopy, Bio-chemistry with ion beams, Advanced electric probes, Plasma Modelling techniques

# *La conférence en chiffres (Topics)*

***1 - Plasma Fundamentals, diagnostics, and modelling***
2 - Plasma Medecine
3 - Non-equilibrium Atmospheric-Pressure Plasma Processes
4 - Microdischarges and microplasmas
5 - Clusters, particles and powders
6 - Plasmas in Renewable Energies and Environmental Control
7 - Plasma Deposition and Treatment of Polymers
8 - Polymers for Biomedical Applications
***9 - Plasma spray and thermal plasma***
10 - Plasma-aided Micro & Nano-fabrication
**11 - Plasma sources: design and characterization**
12 - Plasmas in liquids
13 - Plasmas-Assisted Combustion and Aerodynamics

Plenary lectures (45 minutes) : ***6*** (6 en 2011)
Lecture invitées (30 minutes) : ***12*** (0 en 2011)
Présentations orales (15+3 minutes) : ***139*** (132) réparties sur 3 salles
Posters : ***188*** (490)
Auteurs : ***XX (X participants)*** (1752, 645 participants)
Thématiques : ***13*** (16)
Tables rondes : ***0*** (3)
Worshop industriel: ***0*** (1)

# *La conférence en chiffres (Topics)*

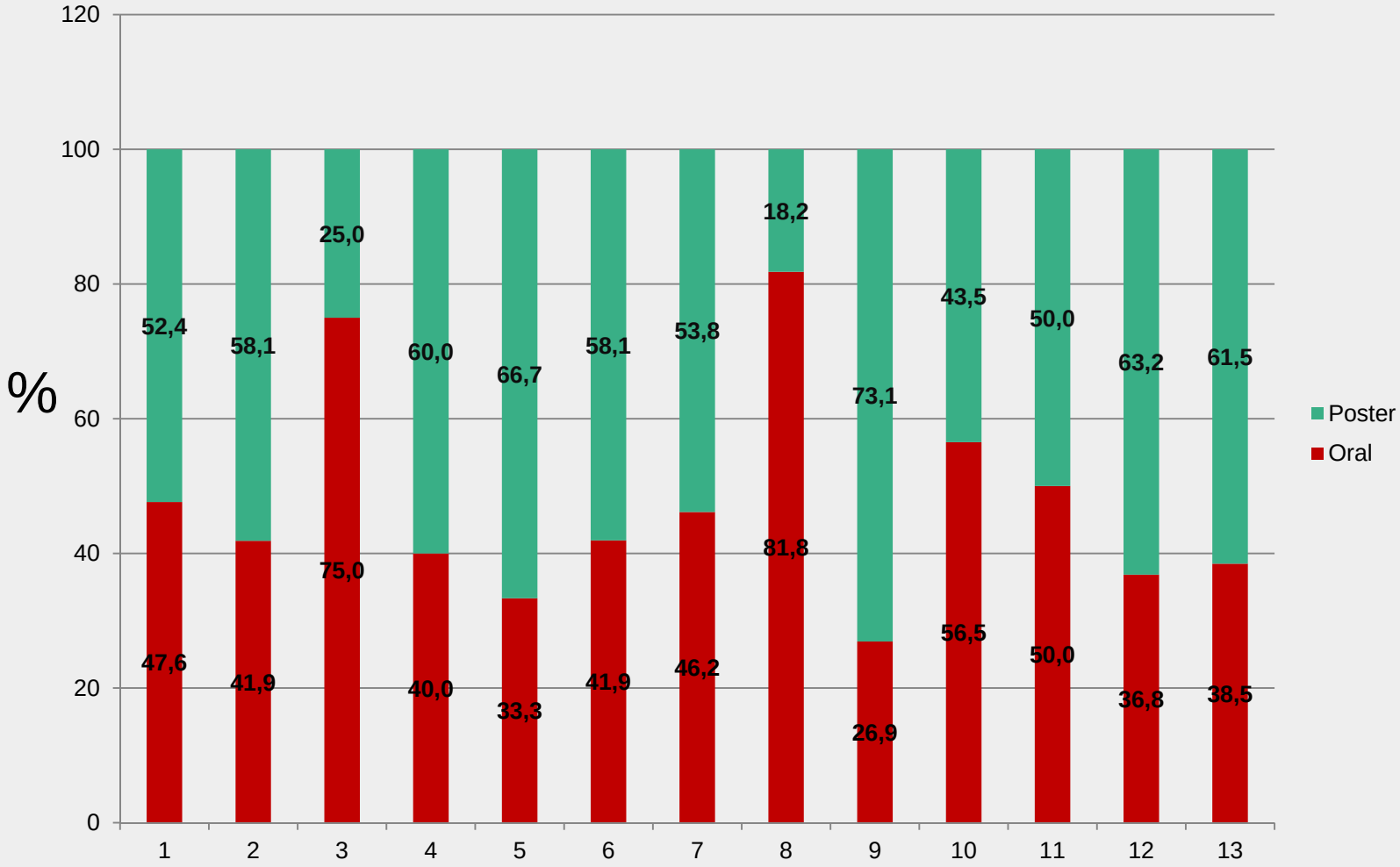


***1 - Plasma Fundamental, Diagnostics and modeling***
***9 - Plasma spray and thermal plasma***
***11- Plasma sources : design and characterisation***

# *La conférence en chiffres (139 présentations orales)*

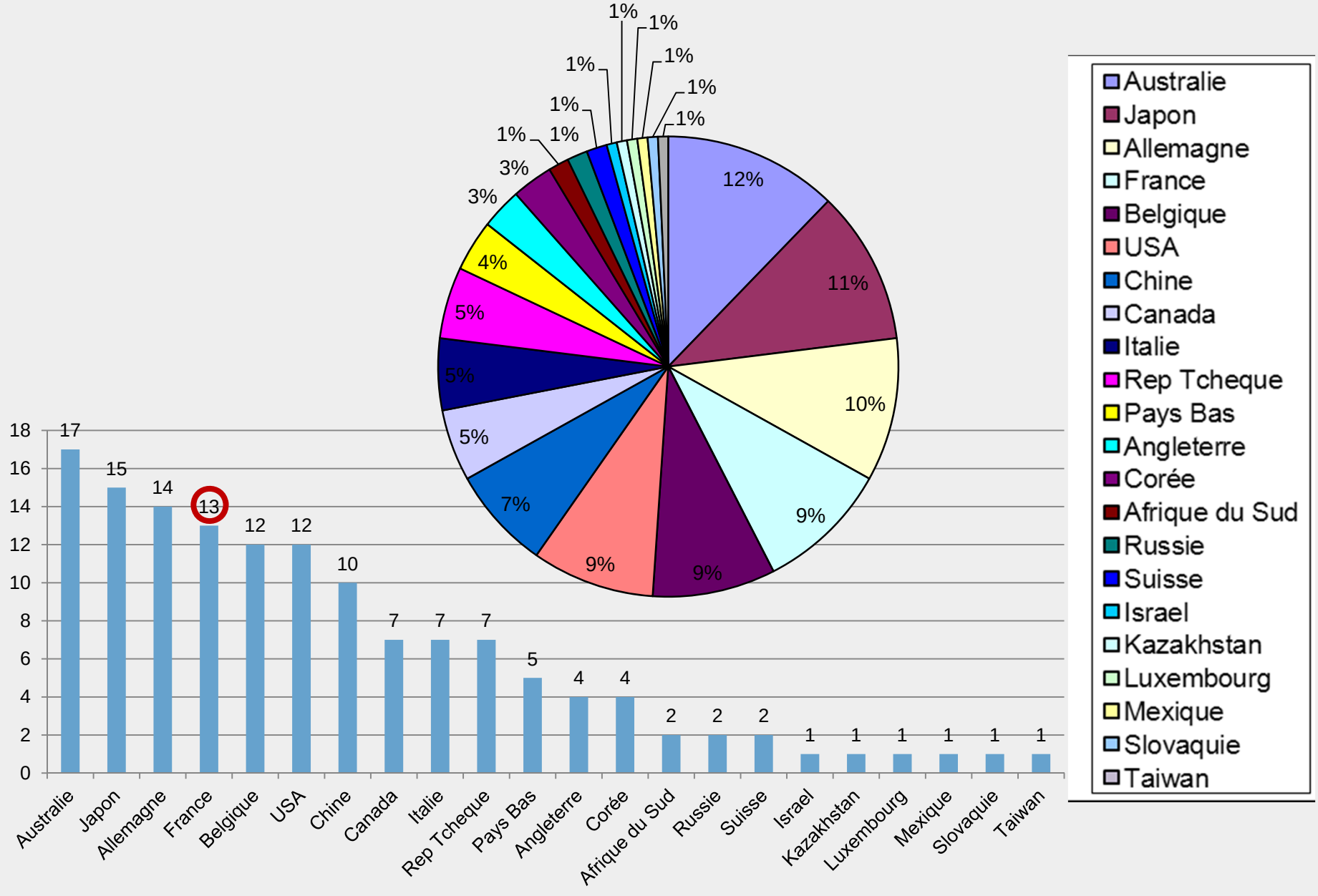

# *La conférence en chiffres (139 présentations orales)*

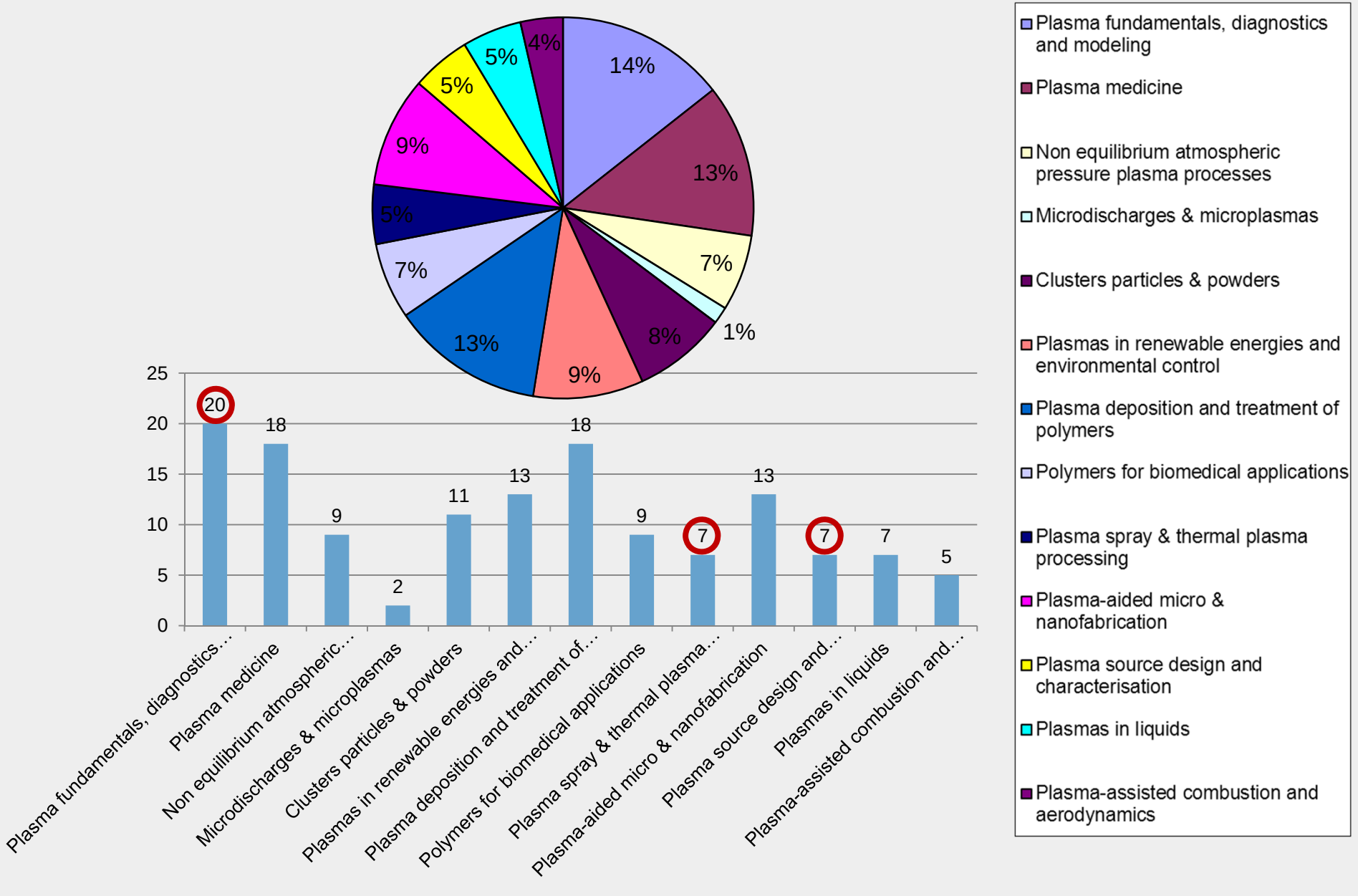

# *La conférence en chiffres (188 posters)*

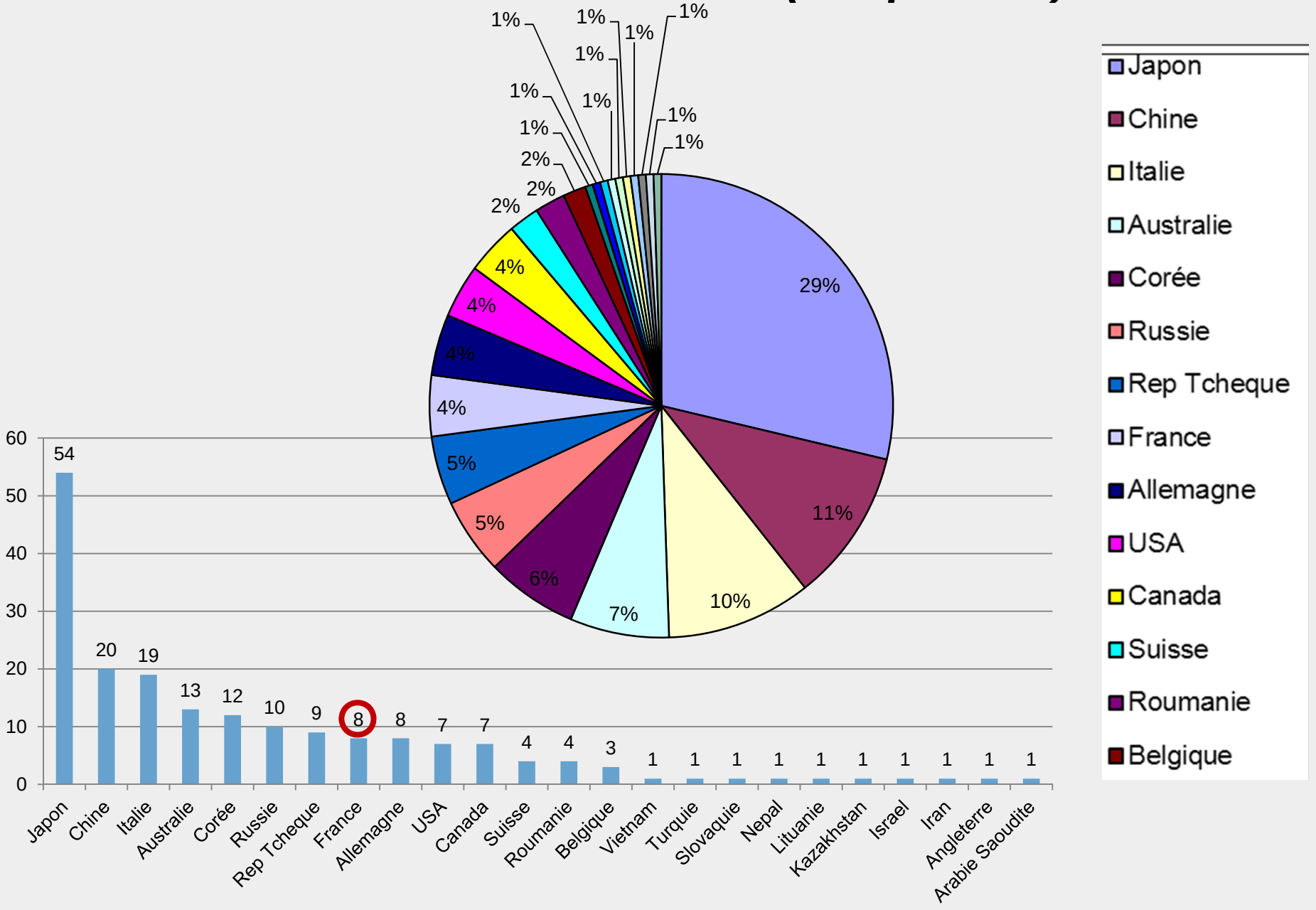

# *La conférence en chiffres (188 posters)*

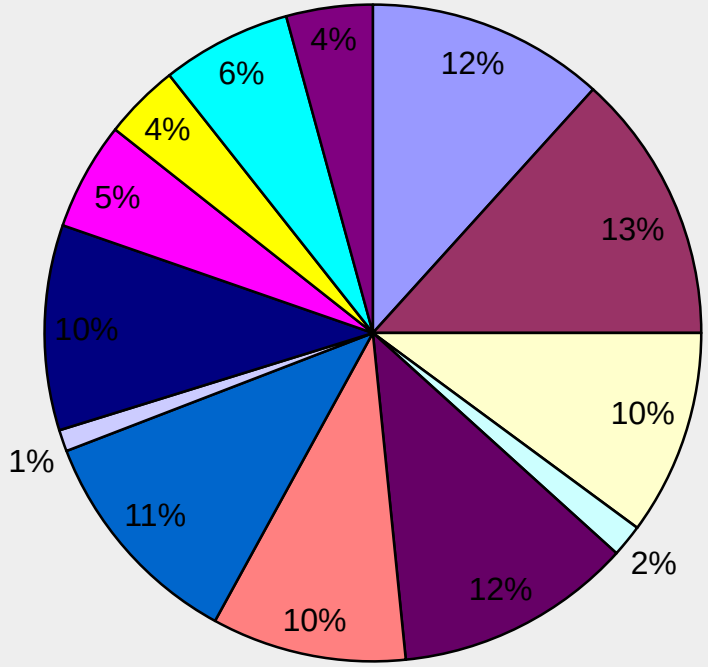


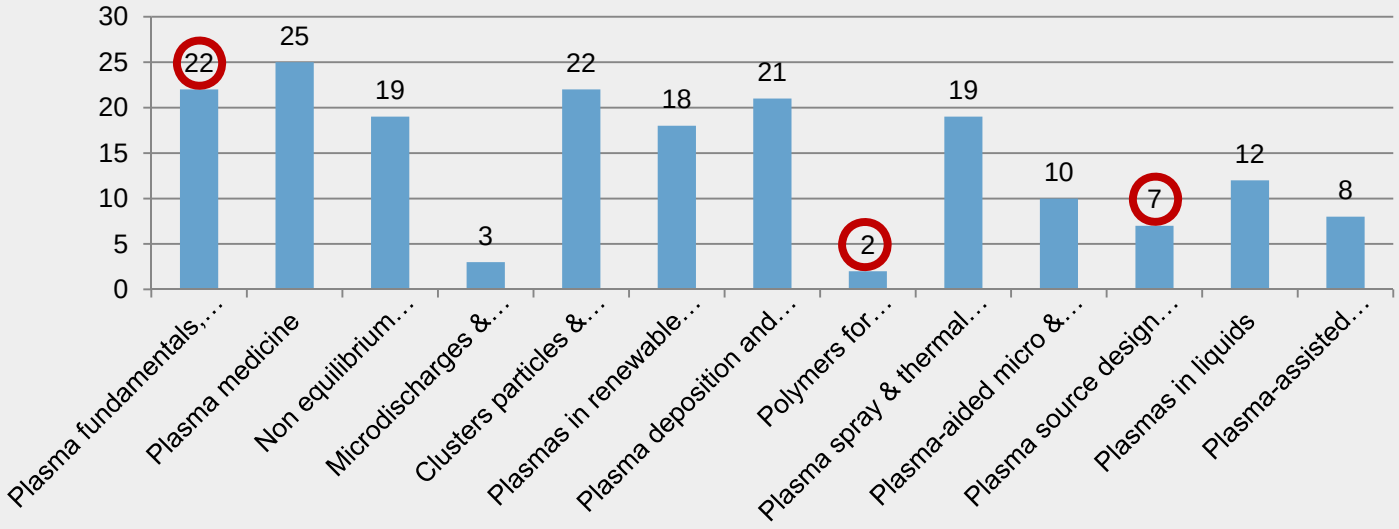


- Plasma fundamentals, diagnostics and modeling
- Plasma medicine
- Non equilibrium atmospheric pressure plasma processes
- Microdischarges & microplasmas
- Clusters particles & powders
- Plasmas in renewable energies and environmental control
- Plasma deposition and treatment of polymers
- Polymers for biomedical applications
- Plasma spray & thermal plasma processing
- Plasma-aided micro & nanofabrication
- Plasma source design and characterisation
- Plasmas in liquids
- Plasma-assisted combustion and aerodynamics

# *Compilation des conférences plénières*

- ***Plasma Polymers: Evolution, Prospects, Promises and Challenges***
Farzaneh Arefi-Khonsari (France)

- ***Plasma Processing Based Nanoscience and Nanocarbon Applications***
Rikizo Hatakeyama (Japan)

- ***Complex Plasmas at a Crossroad with Messy Medicine***
Michael Kong (UK)

- ***Low Temperature Plasma Processing System Design Using Plasma Modelling – An Industrial Perspective***
Shahid Rauf (USA)

- ***Innovative Thermal Plasma Processing from Fundamental Research***
Takayuki Watanabe (Japan)

- ***Plasmas Processes and Polymers: A Personal Perspective (P5)***
Michael Wertheimer (Canada)

# *Compilation des conférences invitées*

- Tailoring plasma properties using pulse-shaping technology, John Paul Booth
- Generation Mechanism of Reactive Oxygen Species in the Bio-solutions by Nonthermal Bioplasma and its Influence on the Microbial and Mammalian Cells, Eun Ha Choi
- Recent advances in the deposition of nanocomposite thin films by atmospheric pressure DBDs, Fiorenza Fanelli
- Numerical Modeling of the Spatiotemporal Behavior of an RF Argon-Silane Plasma with Dust Particle Nucleation and Growth, Steven Girshick
- **Thermal plasma production and functionalization of graphene nano-flakes as non-noble metal catalyst replacement for platinum, Jean-Luc Meunier**
- Tumor treatment by Pulsed Atmospheric pressure Plasma Streams (PAPS): recent developments and perspectives, Jean-Michel Pouvesle
- Dynamics of species generation in an rf-excited micro-scaled atmospheric pressure plasma jet, Volker Schulz von der Gathen
- Three-Dimensional Integration of Micro Solution Plasmas and Its Application to Material Processing in Large Volume Liquid, Tatsura Shirafuji
- Auto-assembly of a new aromatic silicon material in silane plasmas: over-coordinated silicon nanocrystals and their outstanding chemical, optical, and mechanical properties, Holger Vach
- Nanoengineered plasma polymer films for biomaterials, Krasimir Vasilev
- Modeling study on the nonequilibrium expansion process of plasma arc through a nozzle, Hai-Xing Wang
- Non-Thermal Plasmas for Environmental Applications: Fundamentals and Industrial Applications, Keping Yan

# *Compilation de quelques présentations orales / posters*

***Etudes fondamentales, données de base, mécanismes…***

- **W.Xia: Numerical simulation of magnetically rotating arc plasma**
- **V.Colombo:** Pressure dependence of line-by-line calculation of argon plasma net emission coefficient
- **X.Zhang:** Thermodynamic and transport properties of a non-equilibrium argon plasma
- **L.Hermette:**: Influence of copper vapors on thermal properties of $SF_6$/Cu mixtures existing in High Voltage Circuit Breakers
- **T.Billoux:** Emission spectrum of the electric arc discharge in $CO_2$ between copper electrodes
- **E.Safaei**: Arc Length Estimation in Non-Transferred Direct Current Argon Plasma Torch Using CFD Modeling and Experiment
- **F.Gao:** Changes of the electron dynamics in hydrogen inductively coupled plasma

***Multi-Phase Ac Arc***

- **M.Tanaka: Investigation on electrode erosion mechanism on multi-phase AC arc by high speed camera observation**
- **Y.Liu: Investigation of spatial characteristics of Multi-Phase AC arc combined with in-situ particle measurement**

***Procédés : welding, cutting, circuit breakers, LIBS***

- **T.Tanaka: Quantitative elemental analysis by laser-induced breakdown spectroscopy**
- **N.Phi Long: Reduction of heat flux on the Hafnium Cathode surface by changing the cathode holder shape in plasma arc cutting torch**
- **T.Ito: Understanding and suppression of magnetic arc blow in plasma arc cutting**
- **P.Sanibondi: Prediction of fume formation in a pulsed GMAW by means of 2D time-dependant arc model coupled with nanoparticle tracking**
- **P.Sanibondi: Investigation of a constant current plasma arc welding process by means of two-temperature modelling and OES**
- **L.Wang**: **3D modeling and simulation of arc deflection behavior in vacuum interrupters with consideration of external circuits**
- **Y.Goto: Distribution of driving forces in weld pool affected by temperature near anode in pulsed arc welding with iron vapor**
- **V.Colombo**: High-speed imaging investigation of transient phenomena impacting plasma arc cutting process optimization
- **J.Cao**: Coupling of high frequency oscillations in a dc plasma torch

***Plasma assistés : Combustion - aérodynamique***

- **Hrabovki: Steam plasma assisted gasificationof organic waste by reaction with water, CO2 and O2**
- **H.X Wang**: Modeling study on the nonequilibrium expansion process of plasma arc through a nozzle
- **H.X Wang**: Modeling study on plasma flow and heat transfer of low power helium arcjet

***Synthèses de nanoparticules***

- **J.L Meunier**: **Homogeneous nucleation of graphene nanoflakes (GNFs) in a thermal plasma: Tuning the 2D nanoscale geometry**
- **M.Boselli: Modelling for the optimization of the reaction chamber in silicon nanoparticle synthesis by a radio-frequency induction thermal plasma**
- **E.Tam: 3D modelling of DC atmospheric arc discharges for carbon nanotubes production**
- **L.Fulcheri**: Synthesis of fullerenes from carbon powder in an entrained flow 3-phase AC plasma reactor operating at atmospheric pressure

# Etudes fondamentales, données de base, mécanismes…

- **W.Xia:** **Numerical simulation of magnetically rotating arc plasma**
- **V.Colombo:** Pressure dependence of line-by-line calculation of argon plasma net emission coefficient
- **X.Zhang:** Thermodynamic and transport properties of a non-equilibrium argon plasma
- **Y.Cressault**: Influence of copper vapors on thermal properties of $SF_6$/Cu mixtures existing in High Voltage Circuit Breakers
- **Y.Cressault**: Emission spectrum of the electric arc discharge in $CO_2$ between copper electrodes
- **E.Safaei**: Arc Length Estimation in Non-Transferred Direct Current Argon Plasma Torch Using CFD Modeling and Experiment

# Numerical simulation of magnetically rotating arc plasma

W.Xia, X.Zhang, T. Chen, B.Bai, L.Ding (Pekin, Anhui, Chine)

**Objectifs:** simulation des phénomènes magnétique pour un arc tournant

**Mots Clés:** arc tournant, effets magnétiques, dispersion, diffusion

**Constat:** la présence de plusieurs spots sur la cathode (multi-spots, diffusive spots) modifie les propriétés du plasma et le comportement dd l'arc à l'anode selon le procédé étudié.

**Modèle:**
2D, LTE, MHD, Turbulent, Fluent Ansys
Anode + Cathode modélisée

***Equations classiques:***
+ potentiel scalaire, loi d'Ohm, champ magnétique
+ RNG k-ε équations
+ conduction thermique pour les solides (Anode/Cathode)

***Couplage plasma-cathode***
Plasma Coupling Cathode Model (PCCM)
Transfert énergie à la surface
Proche Cathode 0-0.1mm: eq. continuité «effective» des électrons (Lowke & Morrow)
Flux énergétique à la cathode: eq. Poisson
Refroidissement par émission thermoïonique: eq. Richarson
Refroidissement par rayonnement
Chauffage par rayonnement négligé.

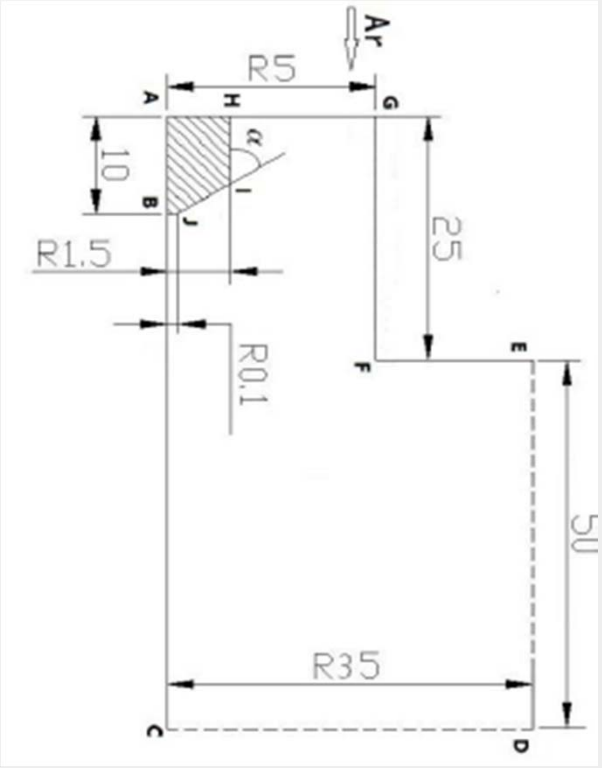

## Numerical simulation of magnetically rotating arc plasma

W.Xia, X.Zhang, T. Chen, B.Bai, L.Ding (Pekin, Anhui, Chine)

**Résultats : plusieurs application, plusieurs conditions limites…**

Le pieds d'arc cathodique dépend de la forme de la cathode, du gaz flow, du champ axial B, du courant…

Le pieds d'arc cathodique agit sur la colonne et sur le pieds d'arc anodique.

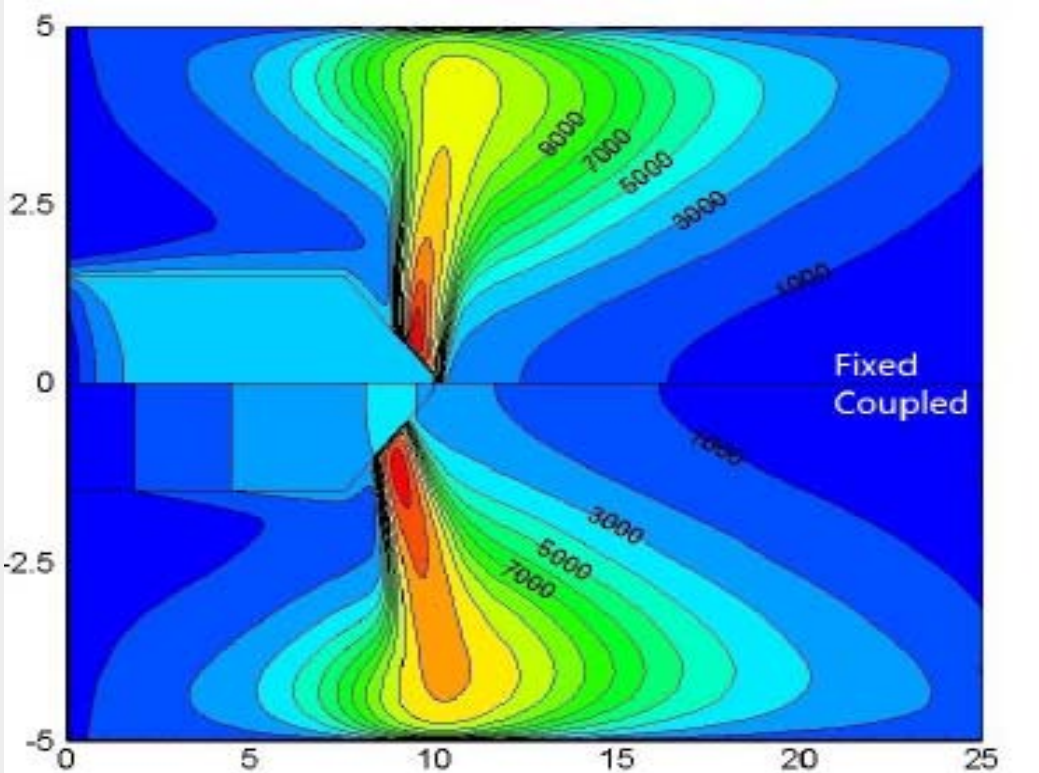


**Figure 2, temperature contour by using the model of arc coupled with cathode (coupled) and given cathode boundary conditions (fixed)**
**(arc currents 200A, gas flow: 0.5m/s , AMF: 0.15T)**

# Pressure dependence of line-by-line calculation of argon plasma net emission coefficient

E. Ghedini[1,2], M. Gherardi[1], F. Rotundo[2], P. Sanibondi[1], V. Colombo[1,2]

[1] Department of Industrial Engineering (D.I.N.)
[2] Industrial Research Centre for Advanced Mechanics and Materials (C.I.R.I.-M.A.M.)
Alma Mater Studiorum-Università di Bologna, via Saragozza 8, 40123 Bologna, Italy

ALMA MATER STUDIORUM
UNIVERSITÀ DI BOLOGNA

BUILDING OUR FUTURE TOGETHER

## SUMMARY OF THE WORK

Radiative processes often represent an important component in energy transport, and the calculation of the radiative flux is necessary in advanced modelling of thermal plasma systems. In order to fill the lack of detailed pressure dependent net emission coefficient data in literature a detailed line-by-line method was implemented to compute the net emission coefficient of Ar plasmas at temperatures ranging from 300 K to 30000 K and pressure ranging from 50 kPa to 500 kPa for optically thin and partially auto-absorbed (optically thick) plasmas. The model is suitable for performing calculation of the net emission coefficient at different plasma thicknesses, by considering the absorption over a large wavelength spectrum. Fractional contributions of different species and of emission mechanisms to the volumetric emission coefficient were determined and the influence of pressure on absorption is discussed.

## NET EMISSION COEFFICIENT (NEC) CALCULATION

NET EMISSION COEFFICIENT (NEC) for ISOTROPIC MEDIUM

$$\nabla \cdot F_{R\nu} = 4\pi(\varepsilon_\nu - J_\nu \kappa'_\nu) = 4\pi\varepsilon_{N\nu}$$

Mean radiation intensity $J_\nu = \frac{1}{4\pi}\int_{4\pi} I_\nu d\Omega$

Radiation Flux $F_{R\nu} = \int_{4\pi} I_\nu \cos\theta \, d\Omega$

Volumetric net emission $4\pi\varepsilon_{N\nu} = 4\pi(\varepsilon_\nu - J_\nu \kappa'_\nu)$

Volumetric absorption $4\pi J_\nu \kappa'_\nu$

For an **isothermal sphere** of radius R $\varepsilon_\lambda(T) = \int_0^\infty \varepsilon_\lambda \exp(-\kappa'_\lambda R) d\lambda$

$I_\nu d\nu = I_\lambda d\lambda$

SPECTRAL EMISSION COEFFICIENT

$$\varepsilon_\lambda = \varepsilon_{\lambda,l} + \varepsilon_{\lambda,fb} + \varepsilon_{\lambda,ff}$$

$\varepsilon_{\lambda,l}$ Line emission (bound-bound)
$\varepsilon_{\lambda,fb}$ Continuum emission (free-bound)
$\varepsilon_{\lambda,ff}$ Continuum emission (free-free) *Bremsstrahlung*

Absorption coefficient (Kirchhoff's law) $\kappa'_\nu = \varepsilon_\nu / B_\nu$ — $B_\nu$=Blackbody emission

### LINE EMISSION

SINGLE LINE EMISSION COEFFICIENT

$$\varepsilon_{ul}(\lambda) = \frac{hc}{4\pi\lambda_{ul}} A_{ul} n_u P_{ul,\lambda}$$

$\lambda_{ul} = \frac{hc}{E_u - E_l}$ Line center wavelength

$\frac{n_{u,0}}{n_l} = \frac{g_{l,0}}{Q_r} \exp\left(-\frac{E_{u,l}}{kT}\right)$ Boltzmann distribution of energy levels

Spectral line broadening $\int_\lambda P_{ul}(\lambda) d\lambda = 1$

Gaussian profiles — Voigt convolution — Lorentzian profiles

### FREE –BOUND CONTINUUM EMISSION

Radiative recombination $A^{n+} + e^- \Rightarrow A^{(n-1)+} + h\nu$

Free electron may assume **non-quantized kinetic energies** → its recombination with an ion will result in continuum radiation

Free-bound continuum emission:

$$\varepsilon_{fb}(\lambda) = \sum_q \frac{C_1}{\lambda^5} \frac{n_q n_e}{\sqrt{T_e}} z^2 \left[1 - \exp\left(-\frac{hc}{\lambda k T_e}\right)\right] \frac{g_{q,0}}{Q_r} \Xi_{fb} \qquad C_1 = \frac{32\pi^2\left(\frac{e^2}{4\pi\varepsilon_0}\right)^3}{3c^2\sqrt{2\pi(m_e k)^3}}$$

$\Xi_{fb}$ **Biberman Factor:** weighted sum of photoabsorption cross sections taking into account the **difference of the atomic energy level structure of argon as compared with that of hydrogen**

### FREE-FREE CONTINUUM EMISSION

**Braking radiation (Bremsstrahlung).** Free electrons loose part of their kinetic energy in the Coulomb field of positive ions. This loss in kinetic energy is converted into radiation.

$A^{n+} + (e^-)_1 \Rightarrow A^{n+} + (e^-)_2 + h\nu \qquad h\nu = \frac{1}{2} m_e (v_1^2 - v_2^2)$

Free-free continuum emission: Biberman factor for ff emission

Electron-ion

$$\varepsilon_{ff}^{ei}(\lambda) = \sum_q \frac{C_1}{\lambda^5} \frac{n_q n_e}{\sqrt{T_e}} z^2 \exp\left(-\frac{hc}{\lambda k T_e}\right) \frac{g_{q,0}}{Q_r} \Xi_{ff} \qquad C_1 = \frac{32\pi^2\left(\frac{e^2}{4\pi\varepsilon_0}\right)^3}{3c^2\sqrt{2\pi(m_e k)^3}}$$

Electron-neutral

$$\varepsilon_{ff}^{en}(\lambda) = \frac{C_1}{\lambda^5} n_e n_n \sqrt{T_e} q(T_e) \left[\left(1 + \frac{hc}{\lambda k T_e}\right)^2 + 1\right] \exp\left(-\frac{hc}{\lambda k T_e}\right) \qquad C_1 = \frac{32\pi^2\left(\frac{e^2}{4\pi\varepsilon_0}\right)^3}{3\sqrt{2\pi}}$$

## NEC AT ATMOSPHERIC PRESSURE

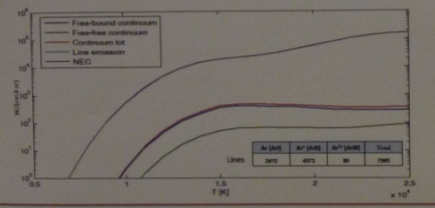


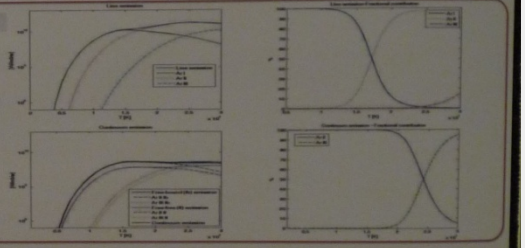

## INFLUENCE OF PLASMA PRESSURE

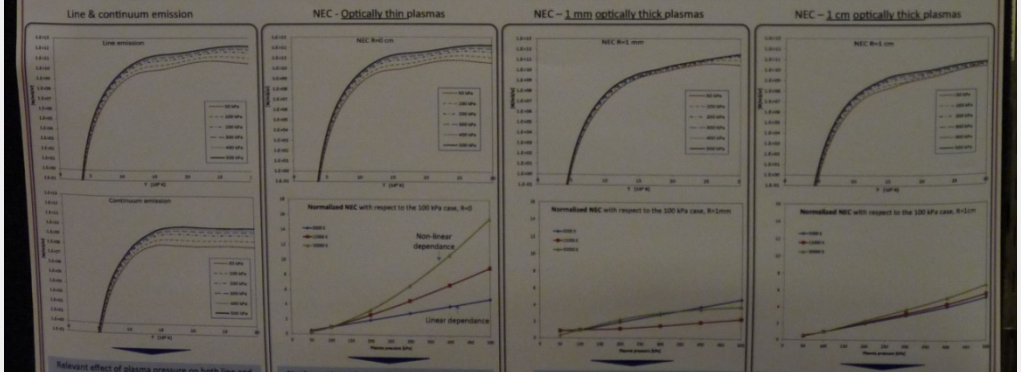


Relevant effect of plasma pressure on both line and continuum emission.

Nonlinear dependence of NEC from pressure over 10000 K in optically thin plasmas.

- The effect of plasma pressure on NEC is reduced for optically thick plasmas over 10000 K
- Linear dependance at all temperatures for the 1 cm thick plasma case

## CONCLUSIONS

In the present work the net emission coefficient of Ar plasmas in the temperature range 300 K - 30000 K and pressure range 50 kPa - 500 kPa was computed by a line-by-line method developed for optically thin and partially auto-absorbed plasmas.

The **dominating radiative mechanism was found to be line emission over the entire temperature and pressure range**. The main contributor is Ar I up to about 17000 K in the pressure range explored, while Ar II dominates up to 30000 K.

The net emission coefficient for optically thin plasma shows a nonlinear dependence from the pressure for **temperatures higher than 10000 K**. The **effect of plasma pressure on the net emission coefficient is generally reduced for optically thick plasma at high temperatures (over 10000 K) with respect to the optically thin case** due to increased absorption owing to the higher plasma density.

## SELECTED REFERENCES


- J. Lowke,J. Quant. Spectrosc. Radiat. Transfer **14** (1974) 111
- V. Aubrecht, J. Lowke, J. Phys. D: Appl. Phys. **27** (1994) 2066–73
- J. Menart, J. Quant. Spectrosc. Radiat. Transfer **67** (2000) 273–91
- V. Colombo, E. Ghedini, P. Sanibondi, Progress in Nuclear Energy **50** (2008) 921–933
- NIST atomic spectra database, available at: http://www.nist.gov/pml/data/asd.cfm
- A.L. Kuruzs, Atomic line database, available at: http://www.cfa.harvard.edu/amp/ampdata/kurucz23/sekur.html
- M. I. Boulos, P. Fauchais, and E. Pfender, Thermal Plasmas-Fundamentals and Applications, Plenum Press, NY (1994)
- J. Menart, J. Heberlein, E. Pfender, J. Quant. Spectrosc. Radiat. Transfer **56(3)** (1996) 377-388
- F. Cabannes, J. Chapelle, Reactions under plasma conditions, L. Chapter 7, Wiley-Interscience (1971)
- A.T.M. Wilbers, G.M.W. Kroesen, C.J. Timmermans, D.C. Schram, J. Quant. Spectrosc. Radiat. Transfer **45** (1991) 1-10
- D. Hofsaess, At. Data Nucl. Data Tables **24** (1979) 285, D. Hofsaess, Quant. Spectrosc. Radiat. **19** (1978) 339-52

# Multi-Phase AC Arcs

- **T. Watanabe:** Innovative thermal plasma processing from fundamental research

- **M.Tanaka:** Investigation on electrode erosion mechanism of multi-phase AC arc by high-speed camera

- **Y.Liu:** Investigation of spatial characteristics of Multi-Phase AC arc combined with in-situ particle measurement

- **C.Rehmet:** Experimental analysis of arcs behaviour in a 3-Phase AC arc plasma torch : comparison with MHD modelling results

- **C.Rehmet:** 3D unsteady state MHD modeling of a 3-phase AC hot electrodes plasma torch

**Présentation disponible**

# Innovative thermal plasma processing from fundamental research

T. Watanabe, Kyushu University (Fukuoka, Japon)

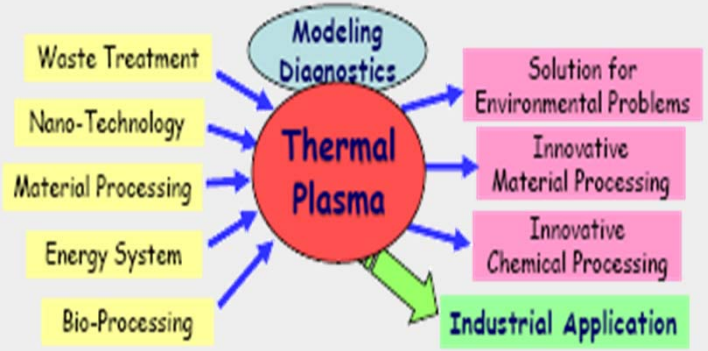


## *1 – Plan de la présentation*

- Innovative In-flight Glass Melting
- Electrode phenomena for nanoparticules
- Nanoparticules formation in plasmas
- Waste treatment using thermal plasmas

## *2 – Introduction sur la partie multi-phase arc*

- concept de fusion en vol pour la production de vitrifiât
- mesure de la température, vitesse et fluctuation de l'arc multi-phase
- caractéristiques des poudres après fusion par plasmas thermiques
- l'industrie du verre consomme près de 1% de l'énergie du Japon
- La fusion représente pour 70% de la production de verre

## *3 – Méthode classique de production*

- aucune innovation du procédé durant 150 ans, forte consommation d'énergie
- 3 à 5 jours pour former le verre à cause d'une forte viscosité, inhomogénéité

**3-5 Jours**

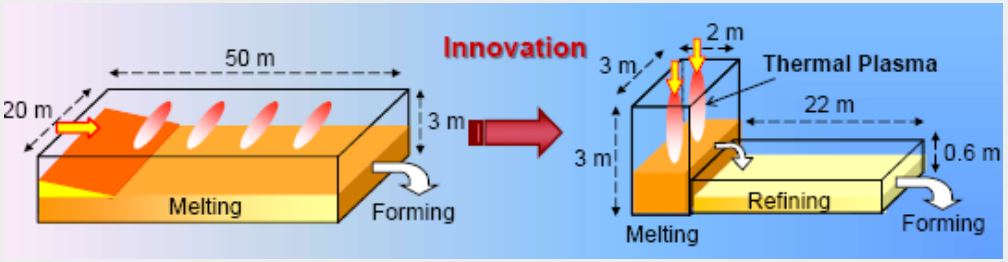


**2-3h**

## *4 – Recherche d'une nouvelle solution*

**Présentation disponible**

- pour réduire le temps de production
- essai de 3 nouvelles sources de plasmas :


## *5 – Multi-phase Arc*

- réduction de la consommation d'énergie de 60%
- 2 à 3 heures de fonctionnement pour la production

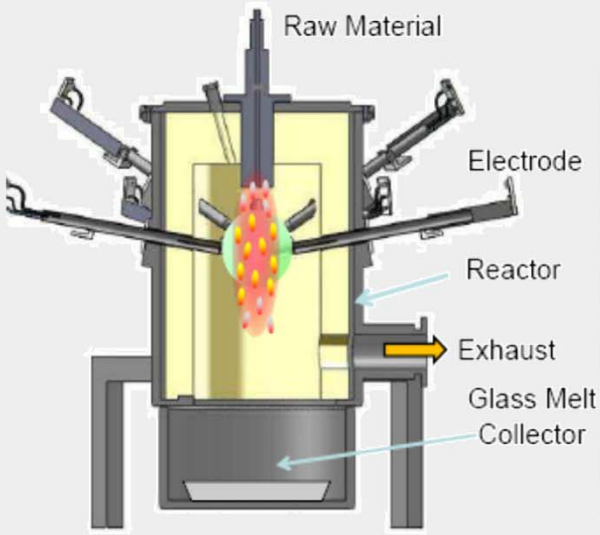


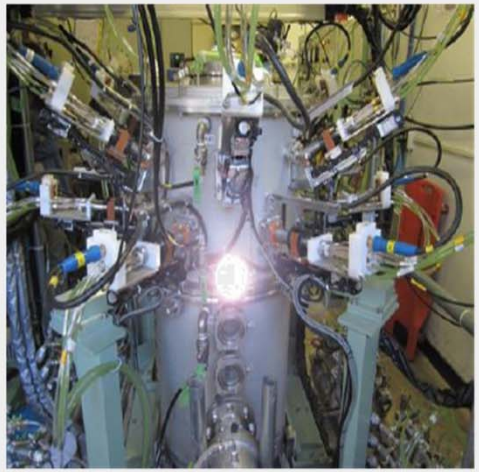

## *6– Études réalisées*

**Présentation disponible**

- Position des 12 électrodes symétriquement + déphasage temporel
- Étude de la reproduction : toutes les 20ms
- Tmax = 7300K et Vmax=20m/s (low)
- Comparaison du degré de vitrification selon les 3 sources de plasma

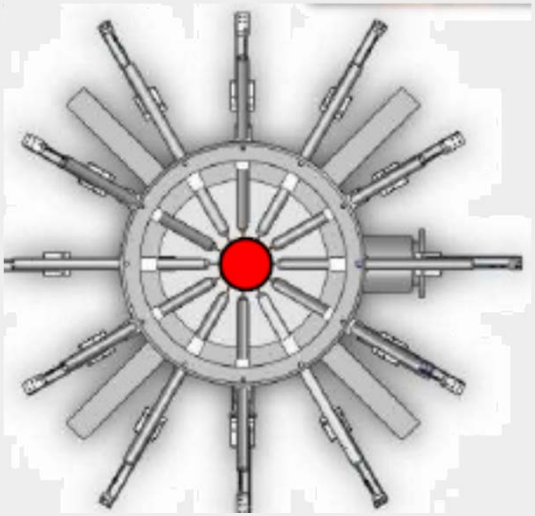

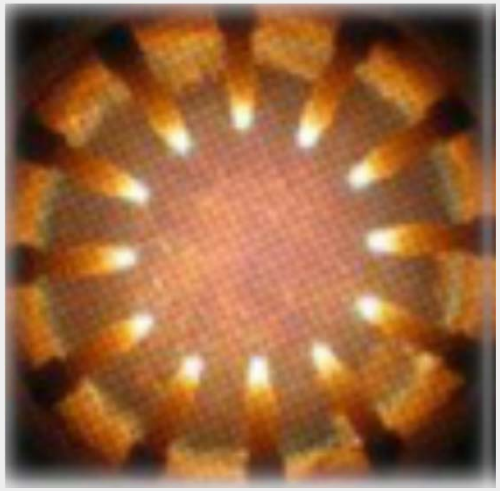

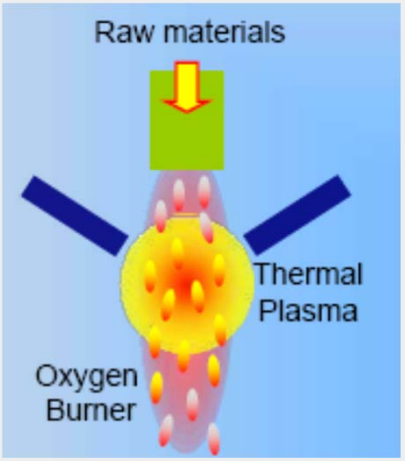


Le changement de la configuration des électrodes modifie la région chaude de l'arc

## *7 – Étude de 2 types de matériaux brut de verre : Soda & alkali*

**Soda-lime glass** *Lower melting temperature*

$SiO_2$-$Na_2O$-CaO-$SO_3$

Target

$72SiO_2$-$16Na_2O$-$10CaO$-$2Al_2O_3$-$0.5SO_3$

**Alkali–free glass** *Higher melting temperature*

$SiO_2$-$B_2O_3$-$Al_2O_3$-BaO-$Sb_2O_3$

Target

$49SiO_2$-$15B_2O_3$-$10Al_2O_3$-$25BaO$-$1Sb_2O_3$

**Présentation disponible**

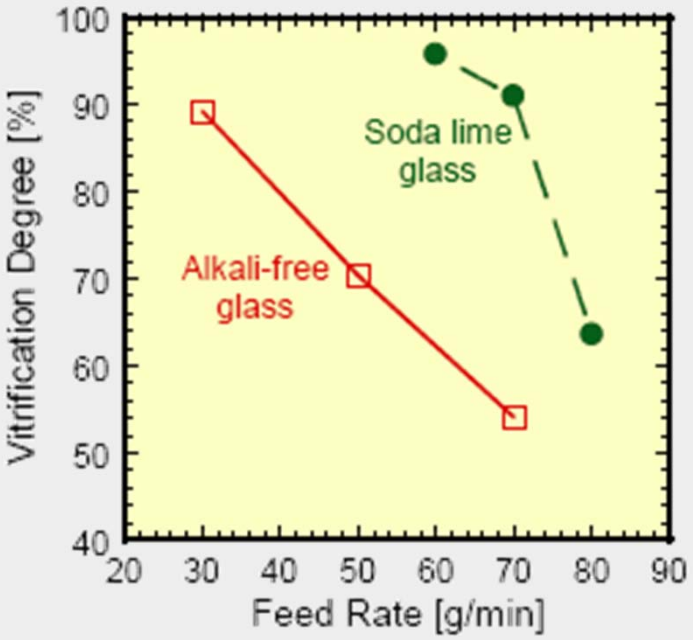


-100% de vitrification pour le verre soda-line
et 90% pour les verres alkali-free

- Le verre alkali a un plus faible degré de vitrification à cause de sa haute température de fusion et de sa haute viscosité

| Analysis | |
|---|---|
| TG | Evaluation of vitrification |
| XRD | Evaluation of vitrification |
| SEM | Particle morphology |
| EPMA | Element distribution |
| ICP–AES | Composition analysis |

**Degree of vitrification (Alkali-free glass)**

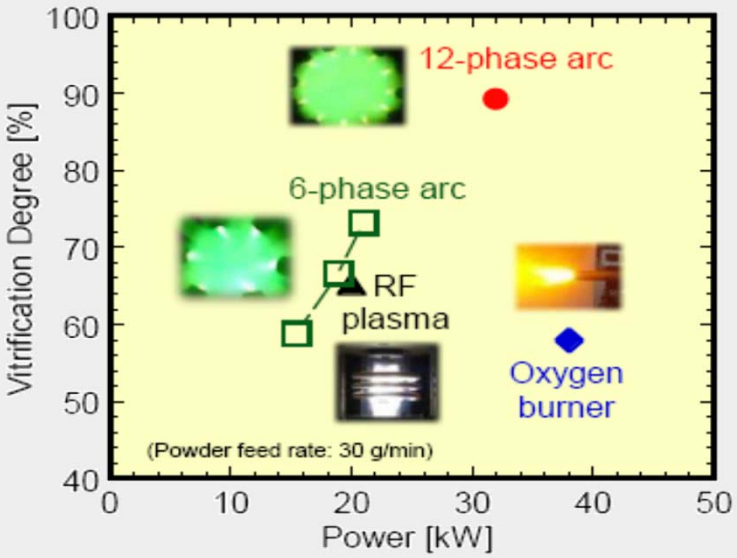


**Alkali–free glass**
Average diameter: 80 μm
Feed rate: 30, 50, 70 g/min
Power: 46 kW

**Soda lime glass**
Average diameter: 99 μm
Feed rate: 30 g/min
Power: 36, 46 kW

Carrier gas (Air): 20 L/min
Shield gas (Ar): 36 L/min
Feed time: 5 min

**$B_2O_3$ volatilization**

12-phase AC arc: 30%
Oxygen burner: 41%

- In-flight melting for glass production provides individual control of temperature and residence time.
- In-flight melting by multi-phase arc can be applied to industrial glass production.

***Objectif : 100 tonnes/jour***

**Présentation disponible**

# Investigation on electrode erosion mechanism of multi-phase AC arc by high-speed camera observation

M. Tanaka, T.Ikeba, Y.Liu, S.Choi and T.Watanabe (Fukuoka, Japon)

**Objectifs:** Comprendre le mécanisme d'érosion des électrodes dans un arc AC multi-phase. Mesure de la température des électrodes pour en déduire une relation entre cette température et l'érosion des électrodes (et la production de vapeurs métalliques).

**Mots Clés:** plasmas thermiques, arc AC multi-phase, érosion électrodes, caméra rapide

**Constat:** nouvelle technologie permet de passer à une vitrification de 2-3h. Large volume (mm de diamètre), faible vitesse (5-20m/s). Pour la durée de vie des électrodes et pour la pureté des produits, il est nécessaire d'étudier l'érosion des électrodes.

**Comment:** combinaison d'une pyrométrie 2 couleurs avec une caméra rapide pour mesurer la température des électrodes sur une durée de quelques millisecondes. Etude du comportement dynamique des vapeurs métalliques.

**Expérience:**

12 phase AC, 12 électrodes W-thoriée 2%,Φ=6mm
12 électrodes (6 en haut inclinées 30 , 6 en bas de 5 )
Gaz argon 99.99 pureté, débit=2-5L/min

T et Vapeurs dans l'arc : 738nm (Ar) et 401nm (W)
FASTCAM SA-5 Photron + band-pass filtres
Pyrométrie 2 couleurs pour T électrodes (785, 880nm)
Spectrometre iHR550 Horiba Jobin Yvon
+ band pass filter (MSI-2, Photron)

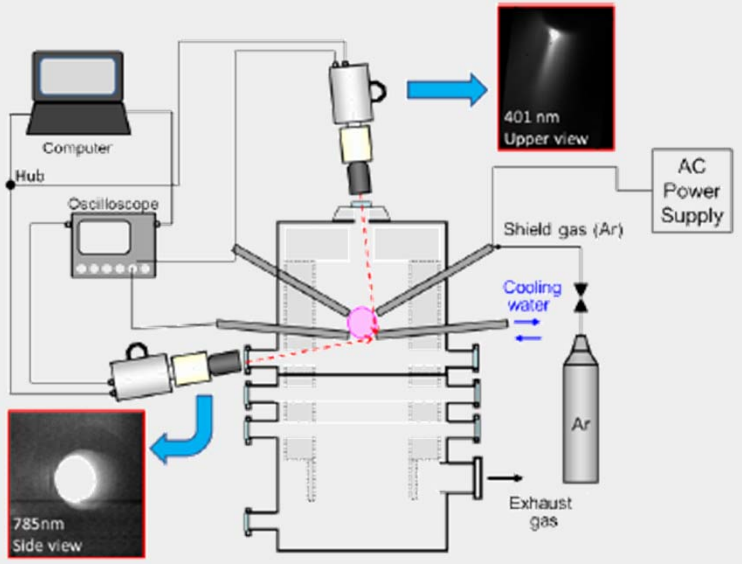

**Présentation disponible**

# Investigation on electrode erosion mechanism of multi-phase AC arc by high-speed camera observation

M. Tanaka, T.Ikeba, Y.Liu, S.Choi and T.Watanabe (Fukuoka, Japon)

**Résultats:** l'électrode en tungstène commence à s'éroder au bout de 5ms (en mode anodique)., éjection des gouttelettes de la surface observée à 17ms.

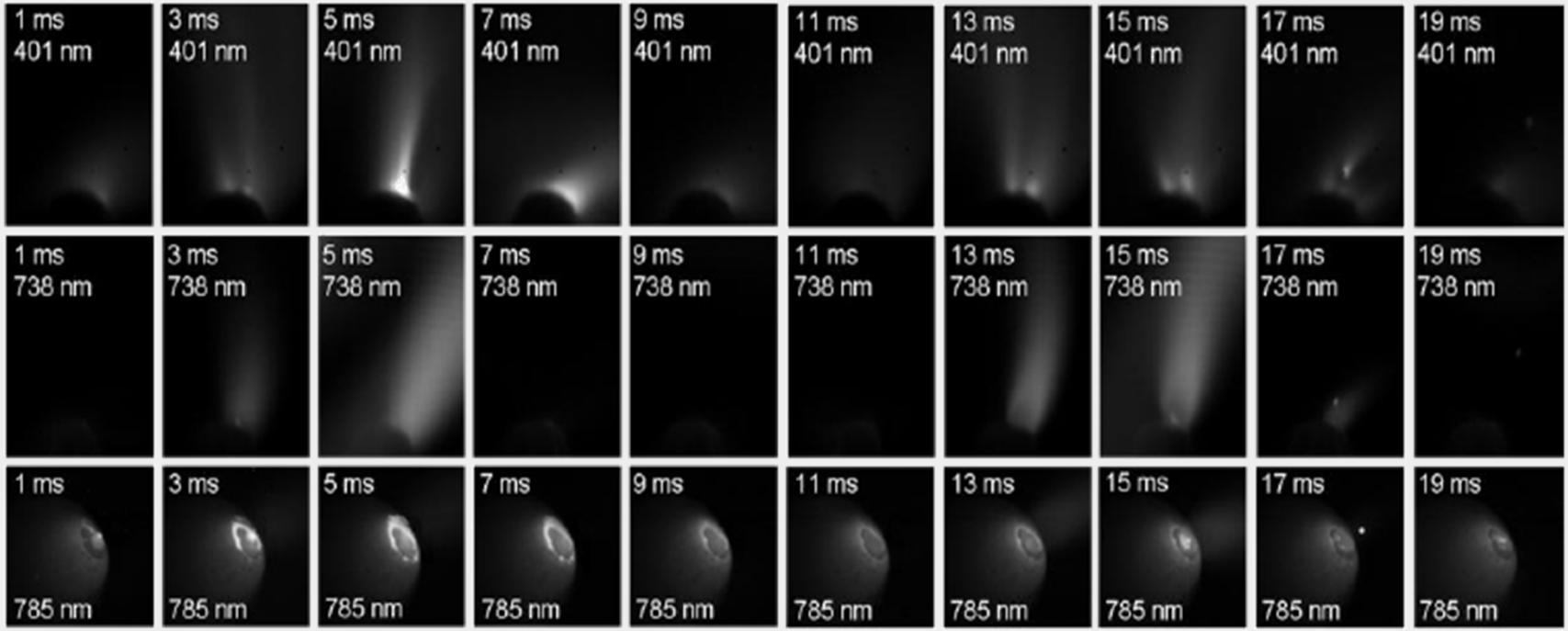


Fig. 4 Representative snapshots of high-speed camera images; upper column: tungsten emission at 401 nm, middle: argon emission at 738 nm, bottom: thermal radiation from the electrode surface at 785 nm.

**Présentation disponible**

# Investigation on electrode erosion mechanism of multi-phase AC arc by high-speed camera observation

M. Tanaka, T.Ikeba, Y.Liu, S.Choi and T.Watanabe (Fukuoka, Japon)

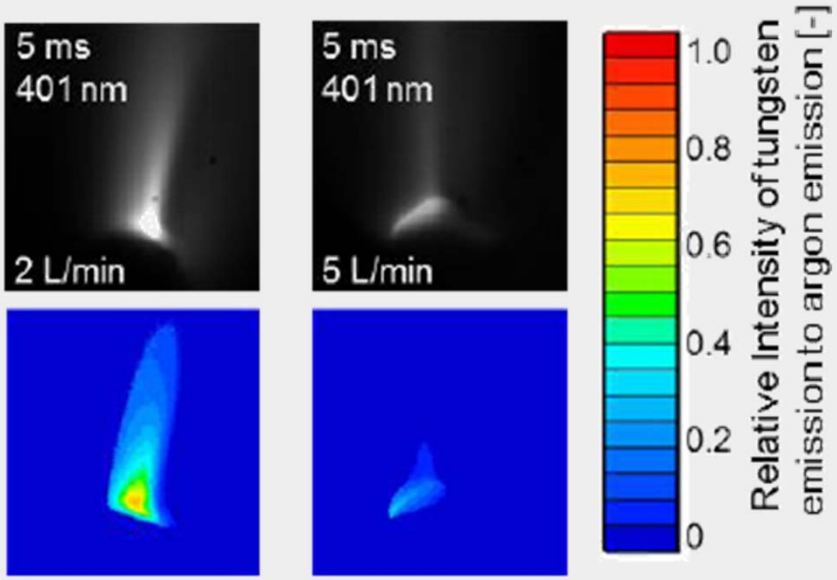


Fig. 5 High-speed images and distributions of the relative intensity of tungsten emission to argon emission at 5 ms in the anodic period for different argon gas.

**Intensité plus forte à 2L/min par rapport à 5L/min**

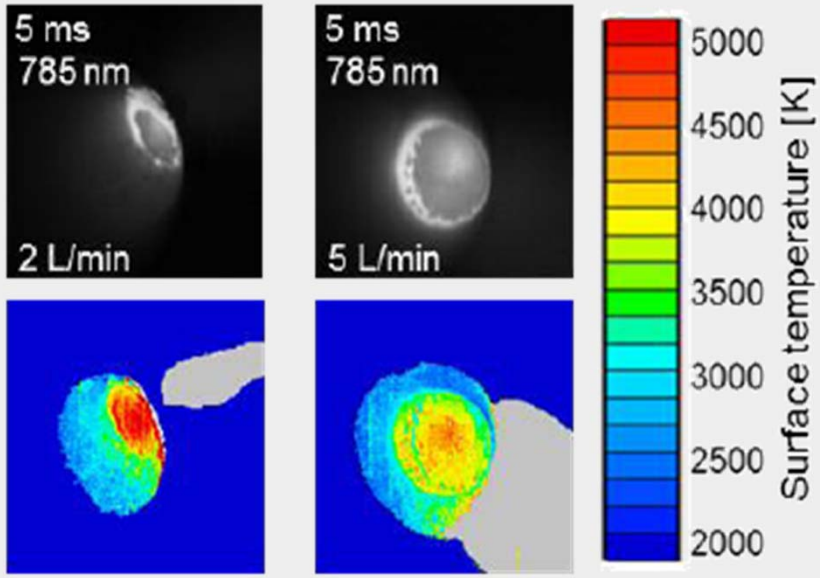


Fig. 6 Temperature distribution of the electrode surface at 5 ms in the anodic period for different shield gas flow rates.

**Température de surface supérieure à 2L/min**

**Présentation disponible**

# Investigation on electrode erosion mechanism of multi-phase AC arc by high-speed camera observation

M. Tanaka, T.Ikeba, Y.Liu, S.Choi and T.Watanabe (Fukuoka, Japon)

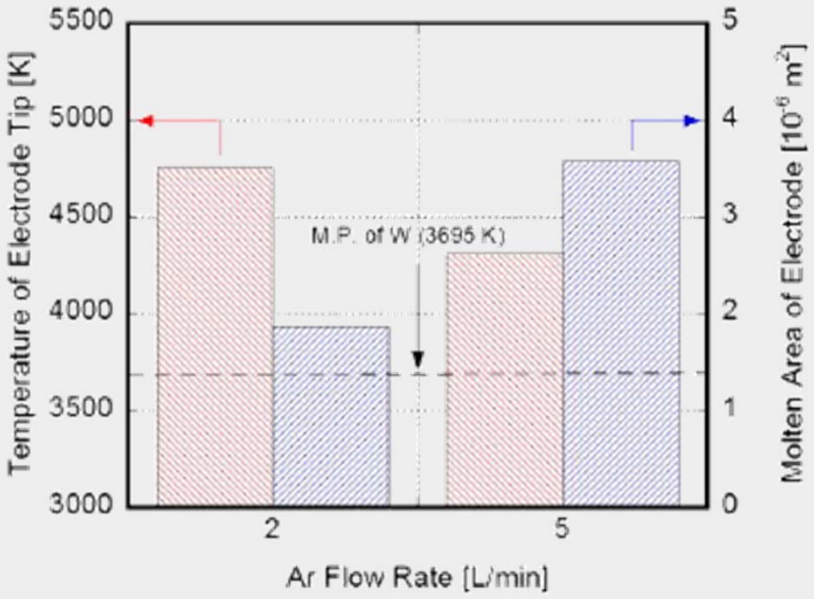


Fig. 7 Maximum temperature of electrode tip and the molten area of electrode at different shield gas flow rates.

**A 2L/min:**
**Température du gaz plus forte**
**Zone de fusion plus faible**
**Forte érosion, arc plus constricté**
**Spot de l'arc stabilisé**
**Bonne cohérence avec les images caméra**

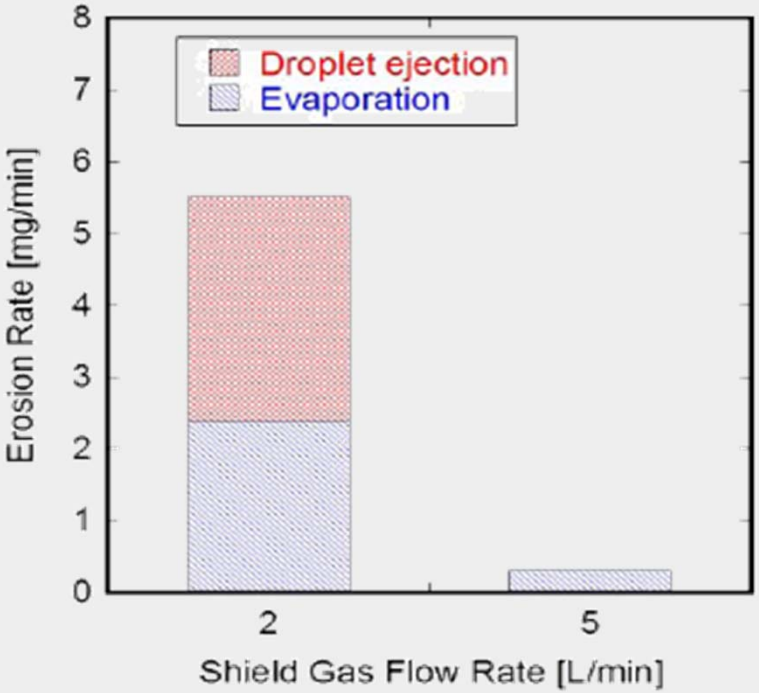


Fig. 8 Relationship between the erosion rate and the shield gas flow rate.

**A 2L/min:**
**Erosion de l'électrode par évaporation et éjection**
**Entrainement de l'oxygène ambiant**

**A 5L/min:**
**Comptage du nombre de gouttelettes**
**Erosion de l'électrode par évaporation**

# Investigation of spatial characteristics of Multi-Phase AC arc combined with in-situ particle measurement

Y.Liu, M.Tanaka, S.Choi and T.Watanabe (Fukuoka, Japon)

**Objectifs:** production vitrifiât par arc multi-phases. Regarder l'effet du profil de température sur les particules en vol et mieux comprendre comment se comportent l'arc et les particules selon la configuration des électrodes ou la vitesse du plasma.

**Mots Clés:** arc multi-phase, particules en vol, camera rapide, pyrométrie 2-couleurs

**Constat:** arc non uniforme spatialement ce qui entraine différentes températures et différentes positions de l'arc, selon la configuration des électrodes: Clockwise (CW) et Flip-Flop (FF). Le débit du gaz et la configuration des électrodes influencent les propriétés du plasma. Avantages d'un plasma multi-phases : grande efficacité, large volume, faible vitesses, installation facile, faible cout.

**Comment:** Observation par vidéo caméra rapide et modèle.

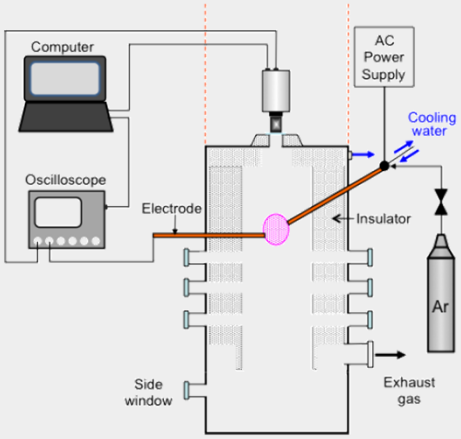


**Expérience :**
12 phase AC
12 électrodes tungtène-thoriée 2%,
6 électrodes en haut inclinées 30
6 électrodes en bas horizontales
Φ=6mm
2 configurations : CW et FF
Gaz argon 99,99 pureté,
débit=5L/min

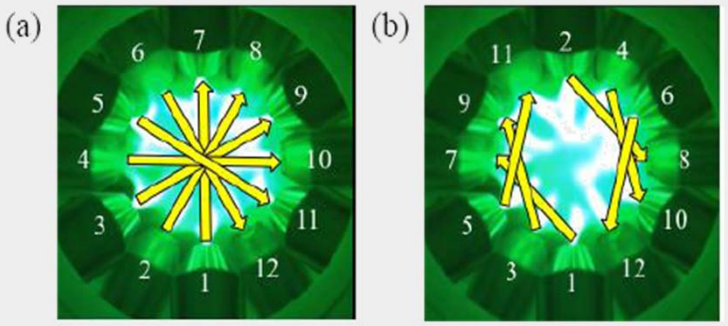


Fig. 2 Electrode configurations of 12-phase AC arc: (a) Clockwise pattern and (b) Flip-flop pattern.

# Investigation of spatial characteristics of Multi-Phase AC arc combined with in-situ particle measurement

Y.Liu, M.Tanaka, S.Choi and T.Watanabe (Fukuoka, Japon)

**Mesures sur l'arc :**

Distance supérieure: cercle de 80mm

Horizontal: 100mm

Camera en haut de la chambre d'arc, 10000f/s, vitesse d'obturation 0.37 micros

Enregistrement toutes les 0,1ms, 10ms, 10 cycles

**Sur le comportement de l'arc:**

**Influence du contour des électrodes**

**Influence du diamètre des électrodes**

**Influence de la configuration des électrodes**

Température uniforme (CW)

Température concentrée proche électrodes (FF)

Mouvement périodique du spot (CW & FF)

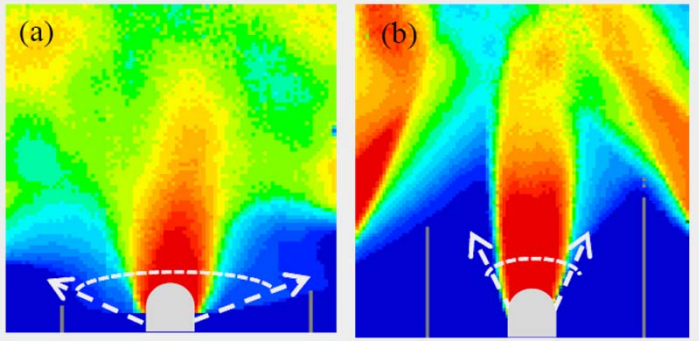


Fig. 4 Contour map of the existence time of 12-phase AC arc with different electrode configurations: (a) CW pattern and (b) FF pattern.

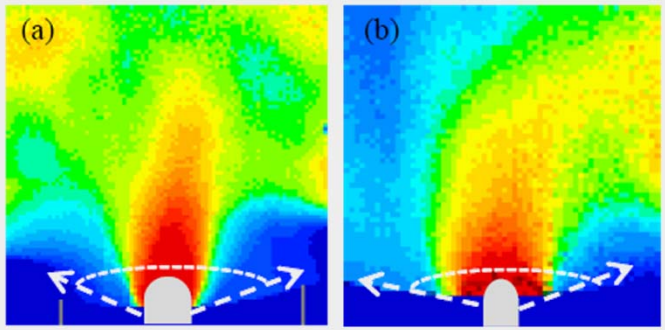


Fig. 5 Contour map of the existence time of 12-phase AC arc with different tungsten diameter: (a) 6 mm and (b) 3.2 mm.

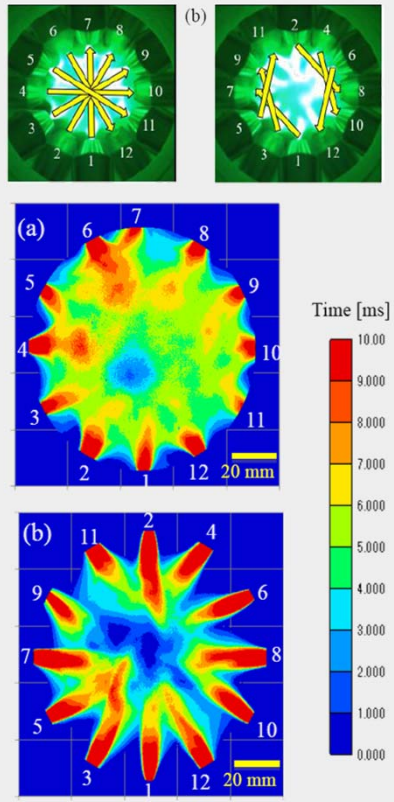


Fig. 3 Arc existence time of the 12-phase AC arc during an AC cycle: (a) CW pattern and (b) FF pattern.

# Investigation of spatial characteristics of Multi-Phase AC arc combined with in-situ particle measurement

Y.Liu, M.Tanaka, S.Choi and T.Watanabe (Fukuoka, Japon)

**Mesures sur particules :**

Alkali free glass 135micrometre de grain
Pyrométrie Haute Vitesse DPV-2000
Capteur 80mm en dessous de l'électrode et bouge radialement
Quand la particule chaude passe devant le capteur (volume du ) une image est enregistrée
Rayonnement thermique émis par la particule est filtré à 785nm et 995nm
Spectromètre Micro iHR550 chez Horiba Jobin Yvon

**Sur les particules :**

**Influence de la configuration des électrodes, de la position radiale, du débit**

CW : ↑ vitesse avec le débit, ↓ légère de la vitesse avec la distance, T linéaire pour les faibles débits (10,20)
FF : ↑ vitesse avec le débit, ↓ plus forte de la vitesse avec la distance, T linéaire pour les faibles débits (10,20)
Vitesse (FF) > Vitesse (CW) sur l'axe

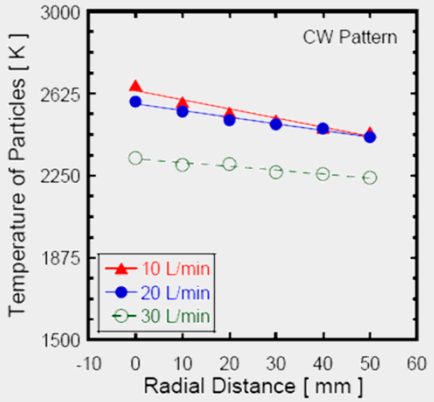


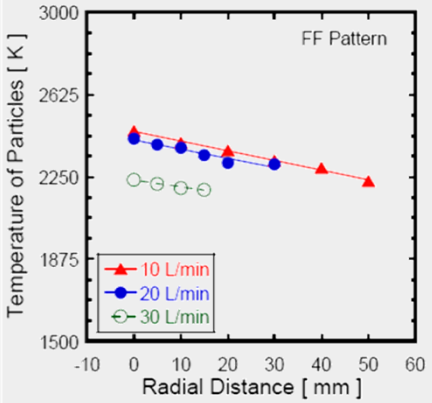


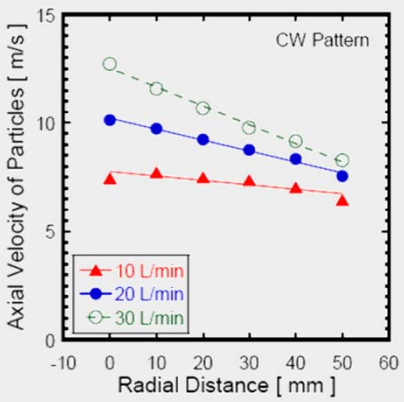


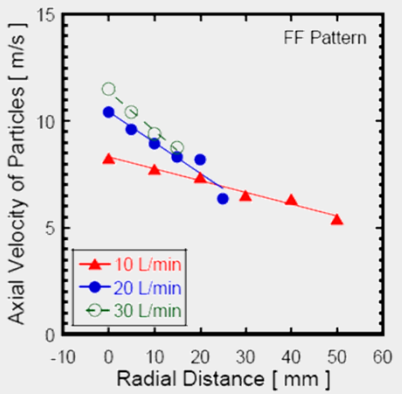

**Présentation disponible**

## (1) Experimental analysis of arcs behaviour in a 3-Phase AC arc plasma torch : comparison with MHD modelling results

## (2) 3D unsteady state MHD modeling of a 3-phase AC hot electrodes plasma torch

C.Rehmet, F.Fabry, V.Rohani, F.Cauneau, L.Fulcheri (Mines ParisTech, PERSEE, Sophia)

**Objectifs:** gazéification, transformation déchets-énergie. Comparaison configuration coplanaire et parallèle des électrodes

**Mots Clés:** mouvement arc électrique, torche à plasma triphasée, MHD

**Constat:** Généralement des torches DC. Torche AC triphasé semblent plus stables

**Comment:** Comportement d'un arc triphasé selon différents paramètres: fréquence, intensité, débit, température et configuration des électrodes. Etude de l'amorçage, l'extinction et le mouvement entre les 3 électrodes. **Modèle et Expérience**.

**Expérience:**

Génération d'arcs tournant
1 période = 6arcs
$I_{exp}$=200A, D=3.82N.$m^3$.$h^{-1}$

Caméra Olympus FS de 100000fps
Tps expo 20µs, 180*132 pixels, située à 2m

Potentiel électrique imposé sur chaque électrode
Sinus 680Hz à partir d'un 263kW 3-Phase converter, déphasage de 2π/3

Électrodes en graphite (cathode, anode, 2x par période)
ϕ=17mm, cône de révolution de 15°, config. triangle

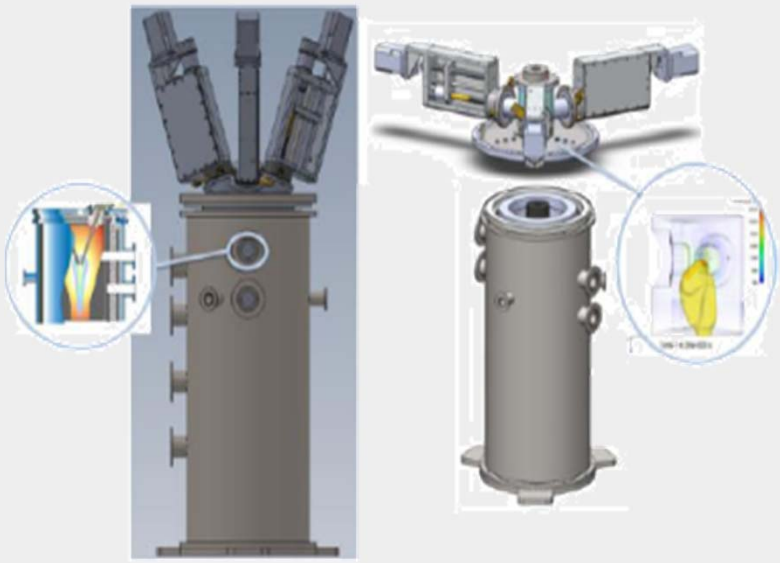

**Présentation disponible**

## (1) Experimental analysis of arcs behaviour in a 3-Phase AC arc plasma torch : comparison with MHD modelling results

## (2) 3D unsteady state MHD modeling of a 3-phase AC hot electrodes plasma torch

C.Rehmet, F.Fabry, V.Rohani, F.Cauneau, L.Fulcheri (Mines ParisTech, PERSEE, Sophia)

**Modèle :**

Code Saturne V2.0, 3D transitoire MHD triphasé, plasma $N_2$

**Géométrie** (Salomé 6), hexaèdre, 800.000 nœuds, électrodes incluses

**Equations classiques** + effet Joule, loi d'Ohm, neutralité électrique + interaction magnétiques (Lorentz…)

**Cond. limites**: hydrodynamiques, thermiques et électromagnétiques

Comparaison électrodes coplanaires / parallèles

8 processus (Intel 2.66GHz)

2µs entre chaque step, 1iter=1min20s, 1 période=1.5ms=750iter=16h

Pic de courant durant 0.75ms de 5A à 400A.

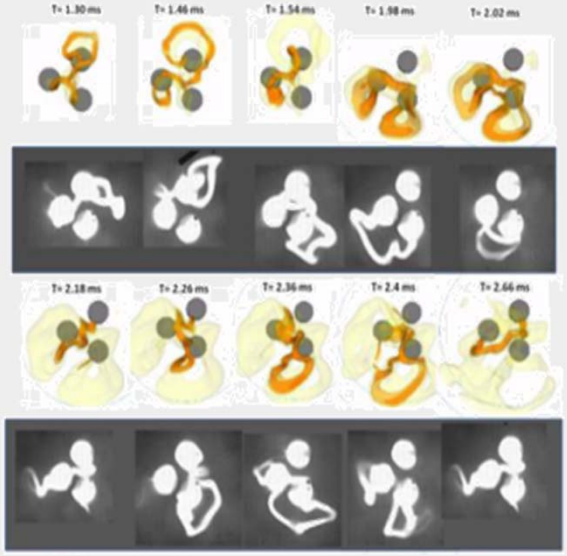

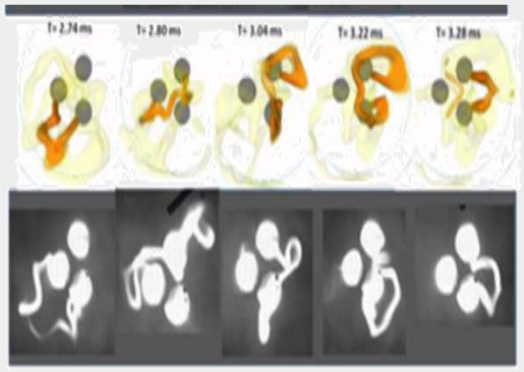

**Fig.3** Comparison of the arc shapes, displayed by a 10 000 K isosurface temperature and hot channels displayed by a 5 000 K isosurface temperature, with the arc video sequence by a bottom view of the inter electrode gap.

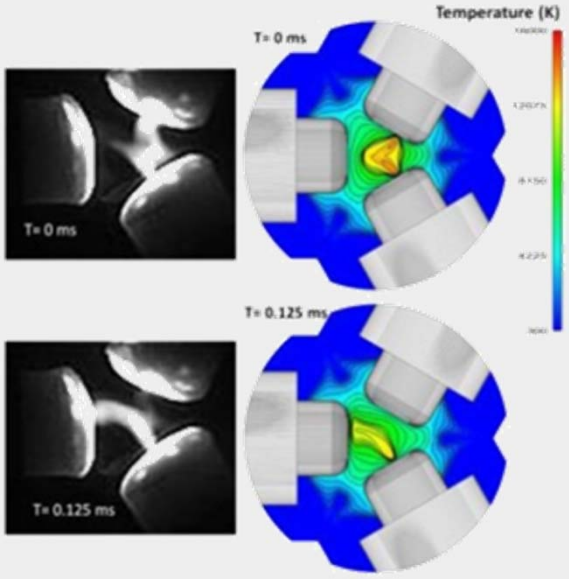

**Présentation disponible**

**(1) Experimental analysis of arcs behaviour in a 3-Phase AC arc plasma torch : comparison with MHD modelling results**

**(2) 3D unsteady state MHD modeling of a 3-phase AC hot electrodes plasma torch**

C.Rehmet, F.Fabry, V.Rohani, F.Cauneau, L.Fulcheri (Mines ParisTech, PERSEE, Sophia)

**Configuration Coplanaire**

Arc contrôlé par l'hydrodynamique
Puissance plus faible
V stable à 35V
Si I augmente, arc est stabilise au milieu des électrodes

**Configuration Parallele**

Arc contrôlé par forces répulsives
Importance des effets magnétiques (Lorentz et Maecker)
Mouvement centrifuge de l'arc
Puissance plus grande

**Ce qui change le comportement**

**Courant d'arc :**

* Si le courant augmente, l'arc se déplace aux extrémités des électrodes, l'arc s'allonge, création d'un canal thermique, la vitesse de l'arc augmente.
* Si le courant diminue, l'arc stagne au milieu des électrodes

**Fréquence :**

* Si la fréquence augmente, le mouvement du canal thermique diminue, l'arc est plus stable
* Si la fréquence diminue, il ne reste plus qu'un seul arc apr7s 10ms

**Importance du canal thermique**

La tension V entre l'arc et les électrodes joue un rôle important
Le mouvement autour de l'électrode inactive joue un rôle important
Le passage d'une paire d'électrode à l'autre s'effectue avec une fréquence =2*fréquence input
Le canal thermique induit augmentation du $\Delta V$ dans la zone proche de l'électrode inactive

**Présentation disponible**

# 3D CFD MHD modeling of a very high pressure plasma reactor working at low current with helium

A.Lebouvier, S.A. Iwarere, D.Ramjugernath, L.Fulcheri (Kwazulu-Natal, Afrique du Sud)

**Objectifs:** production de fluorocarbones. Stabilité des procédés faible courant, haute pression.

**Mots Clés:** MHD modèles, faible courant, haute pression, plasmas

**Constat:** peu de connaissance dans le domaine de la haute pression et des faibles courants mais surtout à forts courants et pression atmosphérique (électrodes, érosion des matériaux, alimentation, puissance, gaz). Procédés intéressants pour la chimie. Premier test effectué pour la synthèse de fluorocarbones et fuel. **Problème:** à faible courant et forte pression, présence d'instabilités numériques.

**Comment:** modélisation d'une torche Fishcher-Tropsch

**Modèle :**
Torche de type type Fischer-Tropsch
**Logiciel:** Code Saturne V2.1 + module électrique de l'arc
**Maillage:** 188550 cellules hexa, structuré, rafiné proche électrodes.

**Hypothèses:**
MHD, arc non transféré, milieux non réactif, non thermique
Temporel, LTE, fluide, incompressible, gravité prise en compte
Navier-Stokes et EMG équations
2MPa-10MPa, I<1A, gaz Hélium

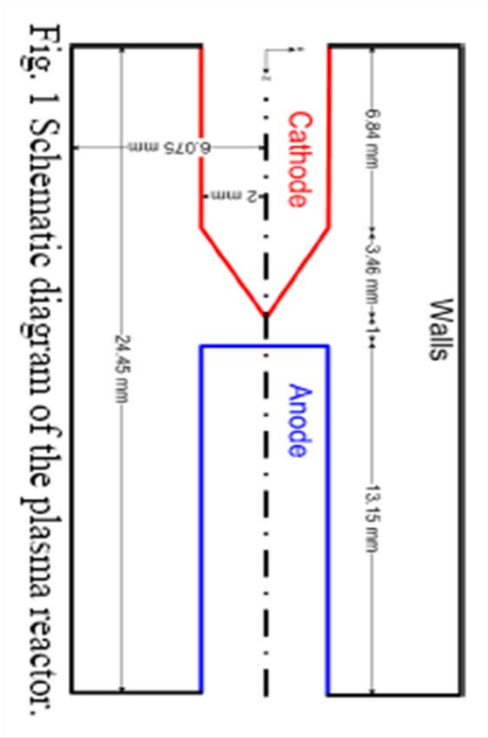

Fig. 1 Schematic diagram of the plasma reactor.

**Présentation disponible**

# 3D CFD MHD modeling of a very high pressure plasma reactor working at low current with helium

A.Lebouvier, S.A. Iwarere, D.Ramjugernath, L.Fulcheri (Kwazulu-Natal, Afrique du Sud)

*** Résultats: I=0.35, P=8MPa**

L'arc reste attaché à la pointe de la cathode, et bouge le long de l'anode dans le temps 2ms-32ms puis stagne.
T=16000K à la pointe de la cathode, T=12700K à l'anode
Rayon de l'arc ~0.168mm (estimé par d'autres études expérimentales à 0.16mm)
A haute pression, faible déplacement de l'arc
Vitesse moyenne de 0.4m/s, section de l'arc ~$3{,}2.10^{-4}mm^2$, débit volumique moyen de $0.128cm^3/s$
La convection est le phénomène le plus influent
Recirculation du gaz dans le réacteur.

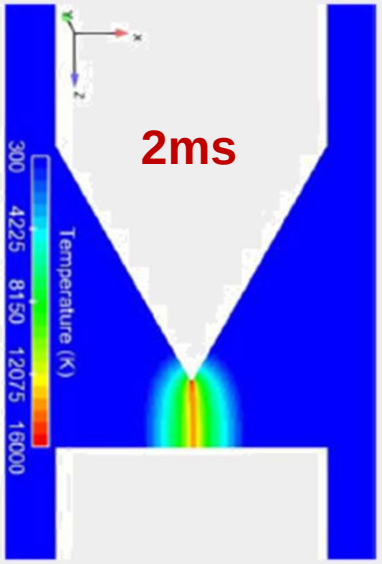


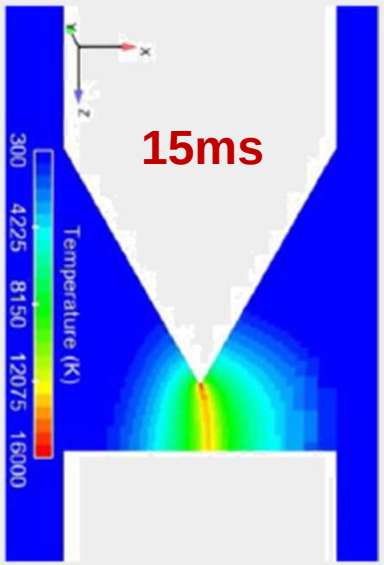


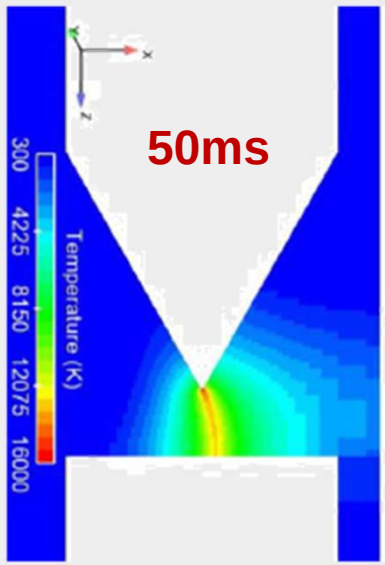


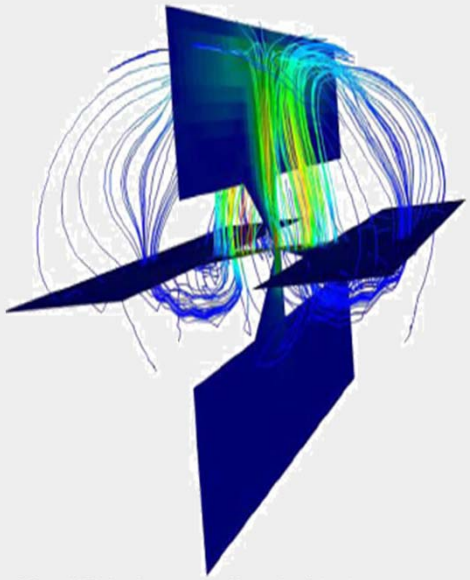

Fig. 4 Velocity streamlines inside the reactor.

**Présentation disponible**

# 3D CFD MHD modeling of a very high pressure plasma reactor working at low current with helium

A.Lebouvier, S.A. Iwarere, D.Ramjugernath, L.Fulcheri (Kwazulu-Natal, Afrique du Sud)

*** Résultats: I=0.35, P varie**

Augmentation des forces convectives, déplacement de l'arc vers le haut du réacteur
Augmentation des gradients de densité responsables de la convection naturelle.
Rôle très important des gradients de densité à haute pression.
Peu d'effet sur le rayon de l'arc qui varie entre 0.153mm et 0.168mm.

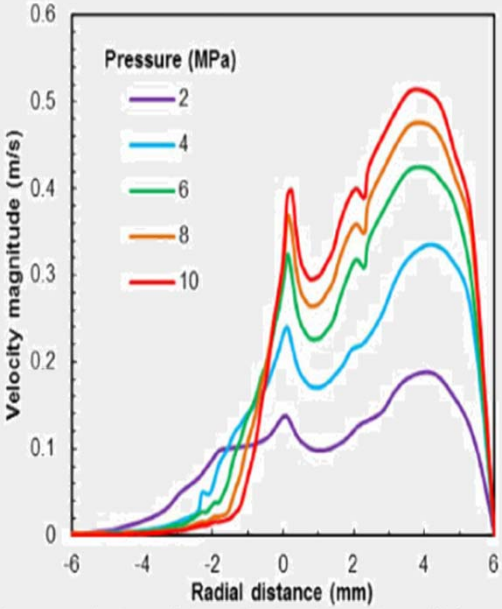


Fig. 6 Evolution of the velocity along the radial cross section as a function of pressure. I = 0.35 A. t = 50 ms.

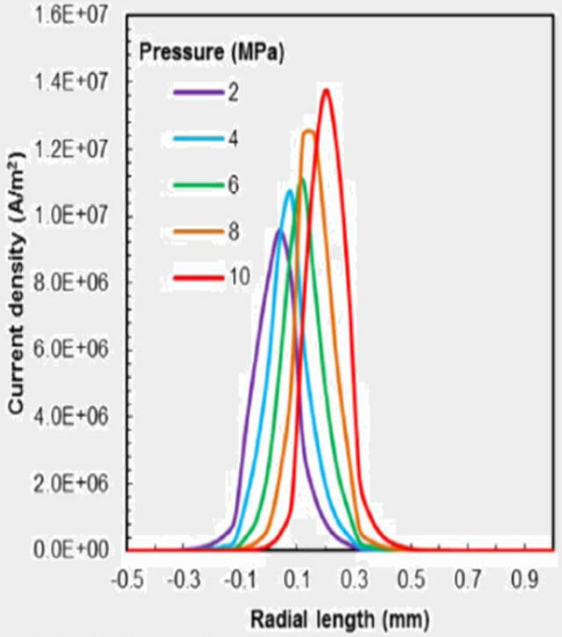


Fig. 8 Evolution of the current density vs. pressure. I = 0.35 A.

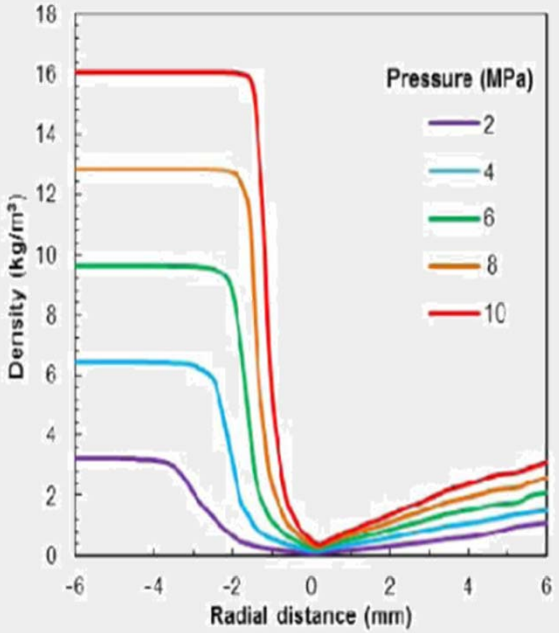


Fig. 7 Evolution of the density along the radial cross section vs. pressure. I = 0.35 A.

**Présentation disponible**

# 3D CFD MHD modeling of a very high pressure plasma reactor working at low current with helium

A.Lebouvier, S.A. Iwarere, D.Ramjugernath, L.Fulcheri (Kwazulu-Natal, Afrique du Sud)

*** Résultats: I varie, P=8MPa**

Très faible influence du courant sur la vitesse de l'arc, la température, le rayon de l'arc ou la pression.

*** Résultat sur la tension:**

Différence observée sur la tension entre modèle et expérience probablement due au modèle de gaine non considéré.
Caractéristique U-I est typique d'une décharge non thermique

**Dans le futur :** ajouter au modèle les modèles de gaines.

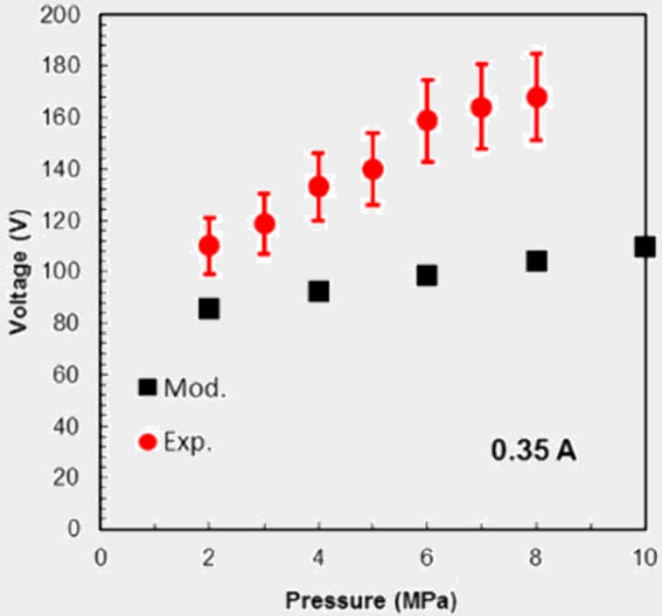


Fig. 5 Simulated and experimental voltage in function of pressure. I = 0.35 A. t = 50 ms.

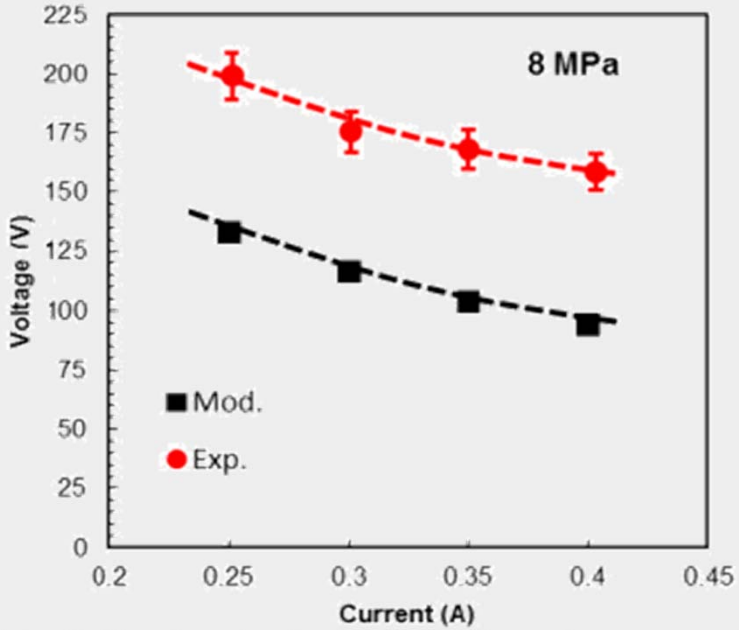


Fig. 9 Simulated voltage in function of current and comparison with experimental data.

# Procédés Thermiques

- **F.Gao:** Changes of the electron dynamics in hydrogen inductively coupled plasma
- **J.Cao**: Coupling of high frequency oscillations in a dc plasma torch

- **T.Tanaka:** **Quantitative elemental analysis by laser-induced breakdown spectroscopy**

- **N.Phi Long:** **Reduction of heat flux on the Hafnium Cathode surface by changing the cathode holder shape in plasma arc cutting torch**
- **T.Ito:** **Understanding and suppression of magnetic arc blow in plasma arc cutting**
- **M.Boselli:** **Prediction of fume formation in a pulsed GMAWprocess by means of 2D time-dependant arc model coupled with nanoparticle tracking**
- **V.Colombo**: High-speed imaging investigation of transient phenomena impacting plasma arc cutting process optimization

- **Y.Goto: Distribution of driving forces in weld pool affected by temperature near anode in pulsed arc welding with iron vapor**
- **P.Sanibondi : Investigation of a constant current plasma arc welding process by means of two-temperature modelling and OES**

- **L.Wang**: **3D modeling and simulation of arc deflection behavior in vacuum interrupters with consideration of external circuits**

# Quantitative elemental analysis by laser-induced breakdown spectroscopy

T.Tanaka, S. Harada, T. Ikegami, F. Mitsugi (Kumamoto, Japon)

**Objectifs:** Amélioration de la technique LIBS. Analyse de la composition de différents métaux oxydés et saletés.

**Mots Clés:** LIBS, analyse, XRF, Spectres

**Constat:** la technique LIBS est populaire car simple, in situ, peu couteuse mais reste moins précise que AAS, AES. Il faut donc améliorer la résolution spectrale avec des appareils adaptés. Spectromètre à très faible résolution.

**Comment:** Comparaison entre spectres calculés et spectres expérimentaux (Températures, composition, élargissements)

**Expériences:**
1000K < T > 16000K
Q-switched Nd:YAG laser
Spectra-Physics GCR-130, 1064nm
Pulse de 8ns, ttes les 10Hz, énergie de 50-200mJ
Gaz ambiant Air, He, Ar
Rotation de la cible

***Emission de la surface***
lentille quartz f=150mm, fibre optique en quartz
USB spectromètre Ocean optics USB4000
Trigger par générateur SR GD535
Résolution spectrale par Fourier Self-Deconvolution method
Labview pour l'acquisition des spectres

***Eléments :***
PZT (Zirconate Titanate), Ti, Zr, Pb, O, Na, Mg, Al, Ca, Fe, V

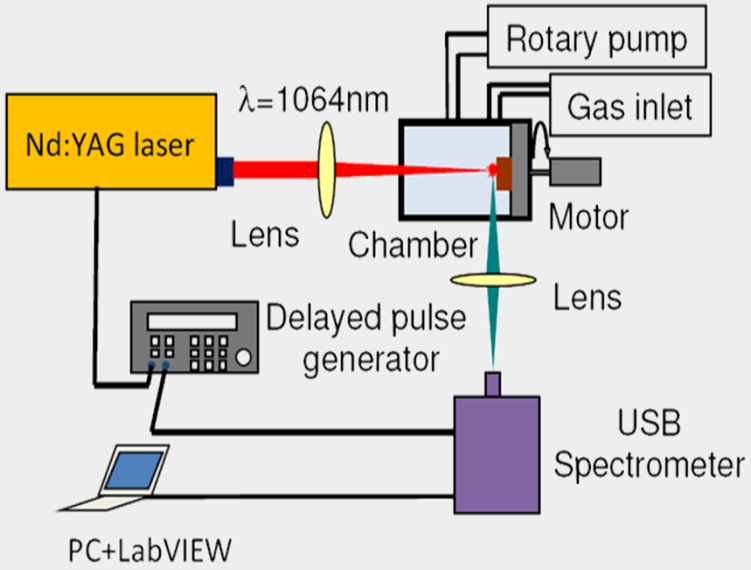

# Quantitative elemental analysis by laser-induced breakdown spectroscopy

T.Tanaka, S. Harada, T. Ikegami, F. Mitsugi (Kumamoto, Japon)

**Mesure du PTZ dans l'air, pression réduite de 70kPa (pour supprimer l'émission de $N_2$)**

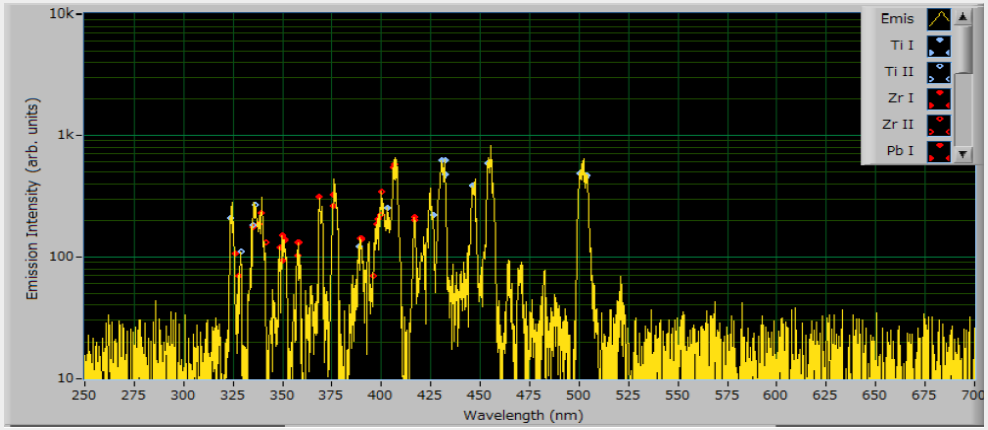


**Spectre PTZ mesuré : Pb : Zr : Ti = 41 : 39 : 20 à 7000K**

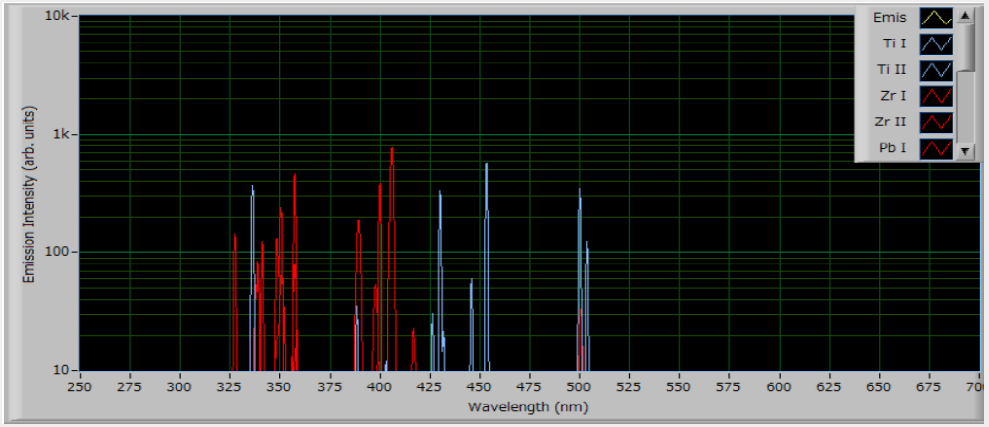


**Spectre PTZ calculé**

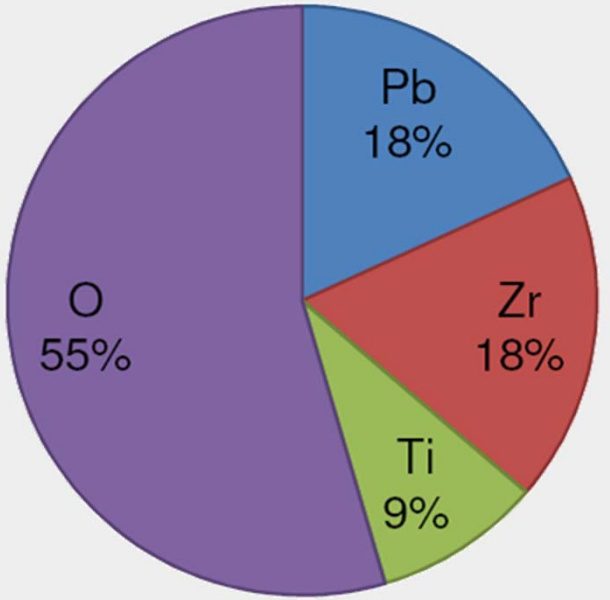


**Composition obtenue par XRF (Rigaku ZSX PrimuxII)**

**Si on exclut l'oxygène, on arrive à :**
**Pb : Zr : Ti : 40 : 40 : 20**

# Quantitative elemental analysis by laser-induced breakdown spectroscopy

T.Tanaka, S. Harada, T. Ikegami, F. Mitsugi (Kumamoto, Japon)

**Mesure pour des saletés, 1atm de gaz He**

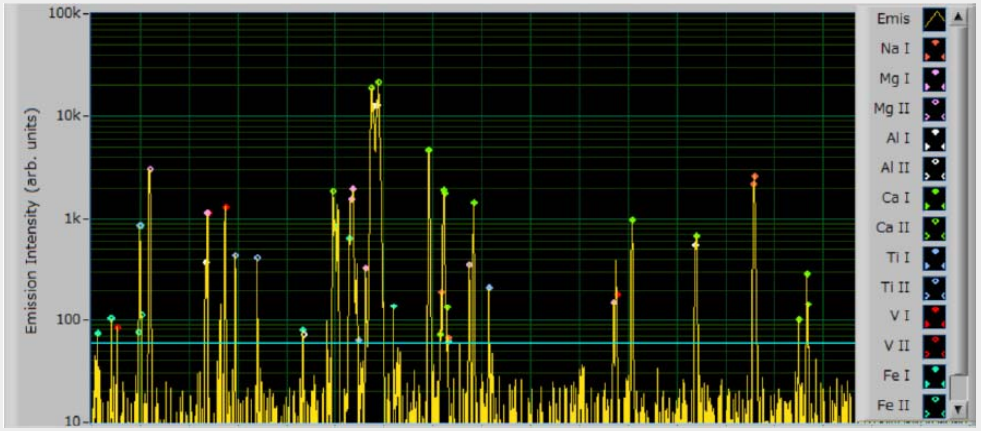


**Spectre PTZ mesuré : Pb : Zr : Ti = 41 : 39 : 20 à 7000K**

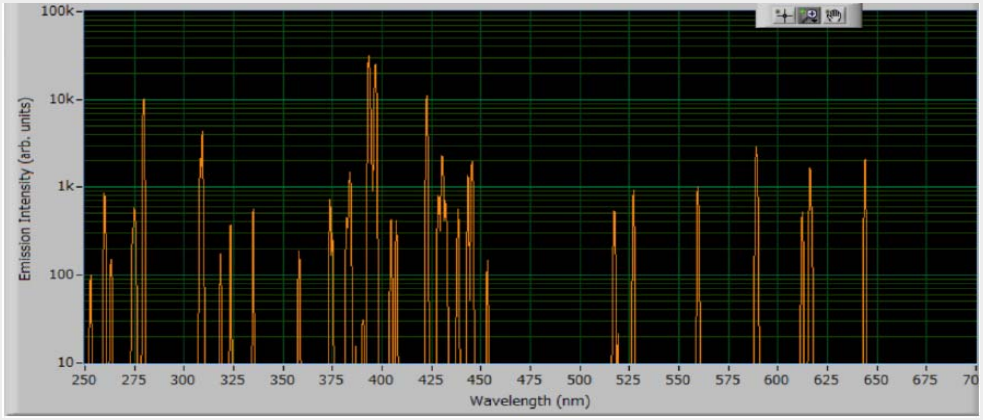


**Spectre PTZ calculé**

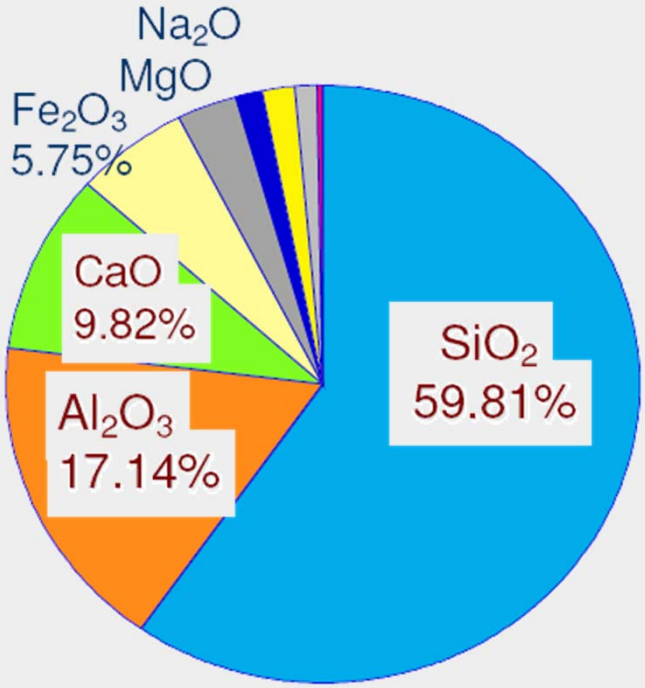


**Composition obtenue par XRF (Rigaku ZSX PrimuxII)**

# Reduction of heat flux on the Hafnium Cathode surface by changing the cathode holder shape in plasma arc cutting torch

N. Phi Long, Y.Tanaka, Y. Uesugi, Y.Yamaguchi (Kanazawa, Japon)

**Objectifs:** Etude de la forme de la cathode (non de l'insert) sur l'évaporation de l'Hafnium par le développement d'un modèle 2D d'un plasma d'oxygène.

**Mots Clés:** plasma de découpe, évaporation de l'Hafnium, forme de la cathode

**Constat:** durant le fonctionnement, du matériel est éjecté de la surface de la cathode (de l'insert). La forme de l'insert change donc rapidement. La géométrie de l'électrode a un effet important sur l'évaporation de celle-ci et sur le comportement de l'arc.

**Modèle:**

Torche de découpe DC, SIMPLE Method
2D laminaire, stationnaire, axisymétrique, LTE
Optiquement mince, considération swirling gaz flow
Electrodes en cuivre avec Hafnium de ϕ =1.27mm
Sortie tuyère ϕ=1.33mm
Gaz $O_2$, $P_{in}$=0.9MPa, I=100A, D=20slm.

***Equations classiques d'un modèle***

+ loi d'Ohm + loi Ampère + cons. masse vaporisée d'Hf

***Electrodes***

Transition solide, liquide, vapeur prise en compte
Emission thermoïonique: eq. Richardon-Dushmann
+ Effet Schottky
Flux de masse par évaporation: eq. Hertz-Knudsen
Pression de vapeur saturante: eq. Clausius Clapeyron

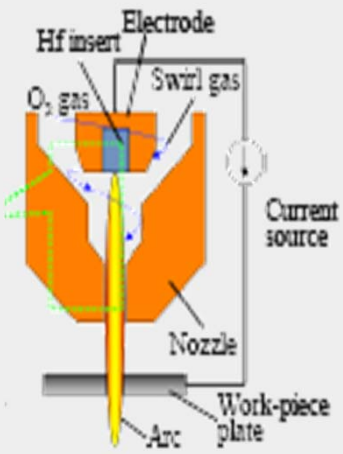


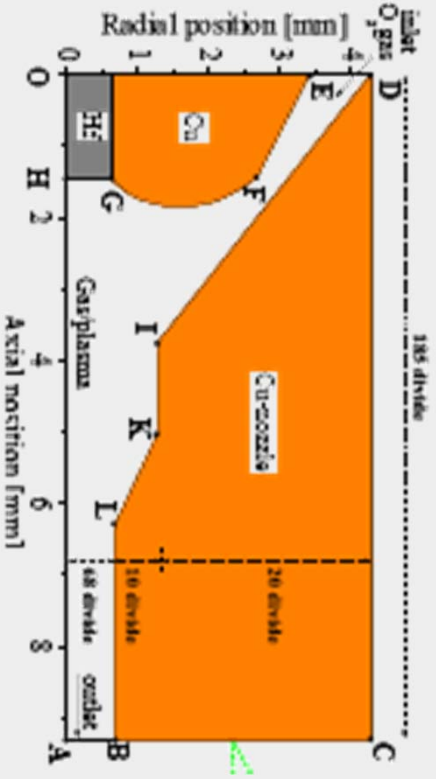

# Reduction of heat flux on the Hafnium Cathode surface by changing the cathode holder shape in plasma arc cutting torch

N. Phi Long, Y.Tanaka, Y. Uesugi, Y.Yamaguchi (Kanazawa, Japon)

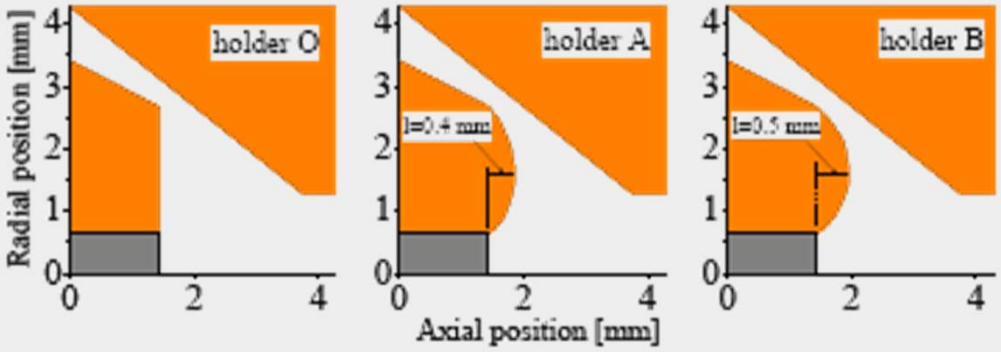


*** Proche de cathode Hf, vorticity plus faible pour O. Pour B, apparition d'une rotation sens horaire.**

*** Masse perdue ↓ avec la taille de cathode à cause du vortex proche surface ce qui ↓ la probabilité d'évaporer l'Hf.**

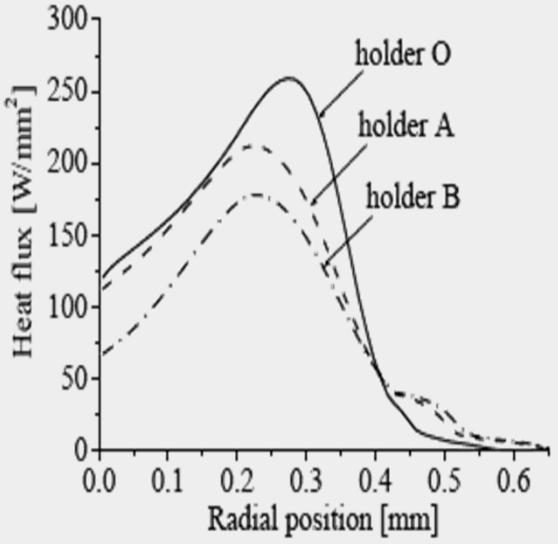


Fig.4 Heat flux on the Hf cathode surface

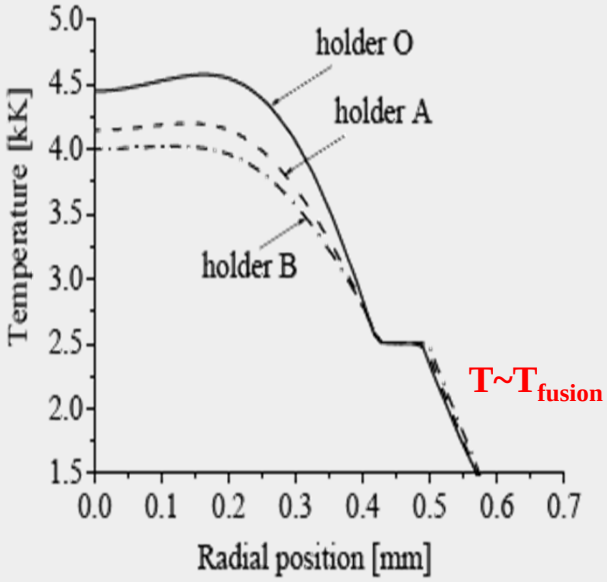


Fig.5 Radial temperature of Hf cathode surface

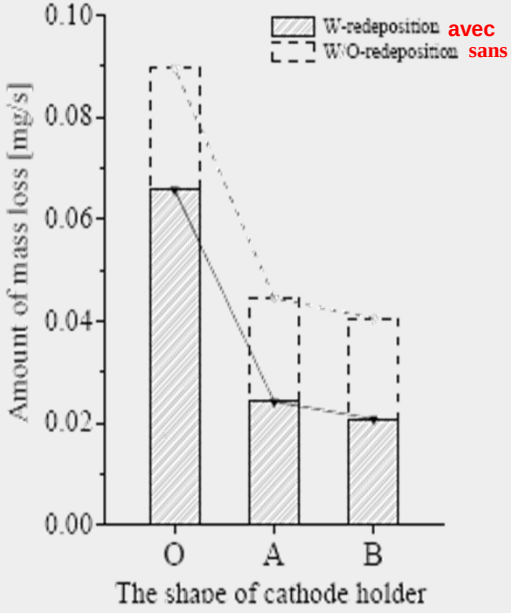


Fig.8 Amount of mass loss of Hf evaporation

# Understanding and suppression of magnetic arc blow in plasma ar cutting

T.Ito, Y.Katada, Y.Uesugi, Y.Tanaka, T.Ishijima, Y.Yamaguchi (Kanazawa, Japon)

**Objectifs:** Relation entre les conditions opératoires et l'apparition d'un double arc.

**Mots Clés:** arc magnétique, double arc, plasma de découpe, «bouclier» magnétique

**Constat:** lors de la découpe d'une plaque, l'arc peut être dévié à cause de la magnétisation de la plaque par les forces de Lorentz. Quand il touche les parois, création d'un arc double ce qui endommage la tuyère: ce phénomène est appelé «magnetic arc blow». Cela coute extrêmement cher de démagnétiser des plaques de plusieurs m² de surface.
**Problème:** l'apparition de nouveaux métaux ou d'alliages entraine l'apparition d'arc double. Il faut donc comprendre ce phénomène et comment le supprimer.

**Comment:** la solution semble technique: ajout d'un bouclier magnétique.

**Expérience:**
Torche DC avec $I_{max}$=150A
Anode cuivrée refroidie
Cathode (Cu-holder, Hf-insert), $\phi$ =1.6mm
Sortie tuyère $\phi$=1.33mm
Mesures à 2.5mm de la plaque
Gaz $O_2$, $N_2$, $P_{in}$=0.9MPa, I=100A, D=20slm.
Haute tension, haute fréquence
Champ B par générateur DC Tohodenki TRM89 (max 140mT)
Plaque : 100mm x 200 x 16mm
Double arc: Caméra NAC memrecam GX-8 (600.000fps)
Présence : Caméra Keyence VW-6000

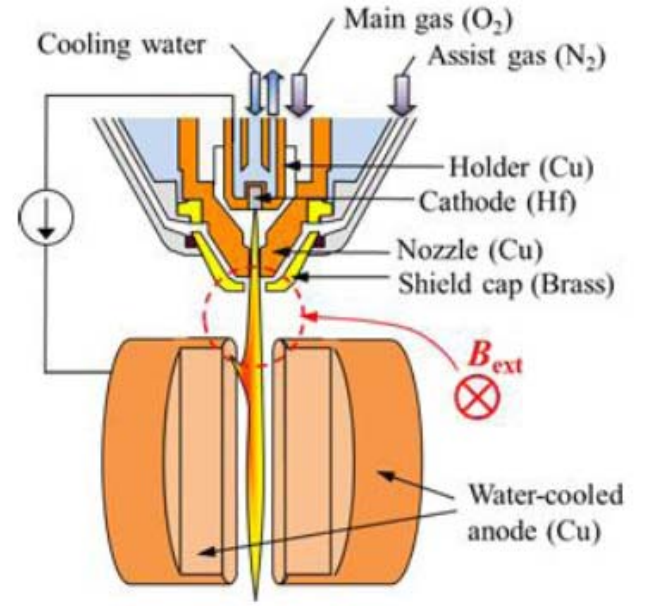

Fig.1. Plasma arc cutting torch and water-cooled anodes.

# Understanding and suppression of magnetic arc blow in plasma ar cutting

T.Ito, Y.Katada, Y.Uesugi, Y.Tanaka, T.Ishijima, Y.Yamaguchi (Kanazawa, Japon)

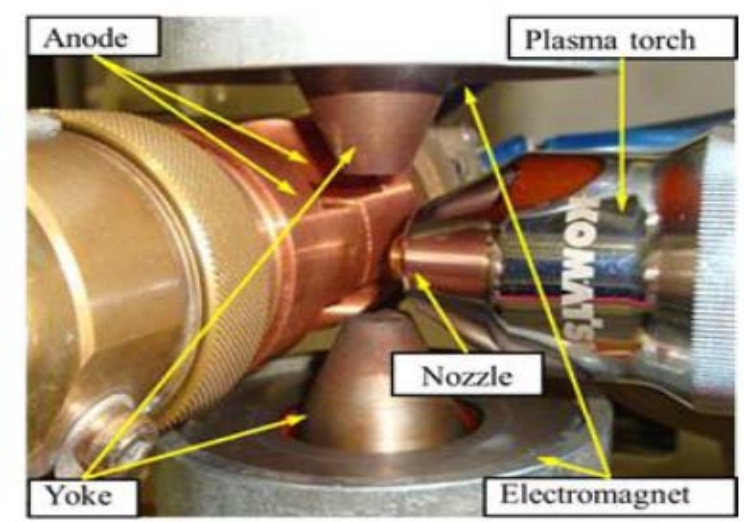


Fig.2. Arrangement of a pair of electromagnets.

**Résultats: beaucoup de résultats proposés**

- Comportement de l'arc dans le champ $B_{ext}$
- Fluctuation de la tension dans le champ $B_{ext}$
- Champ magnétique dans la torche
- Seuil d'apparition ($B_{th}$) du double arc
- Vidéos du double arc
- État de la surface / qualité de la découpe
- Densité B=f(débit, présence ou non cap magnétique)

Si I↑, $B_{th}$↓ (due à la déviation de l'arc par forces de Lorentz)
Si D↓, $B_{th}$↓ (isolation électrique devient moins effective)
Si faible diamètre tuyère, arc en contact avec les parois


**Solutions:**

**Opérer à faible courant, fort débit et large tuyère**
**Ajout d'un bouclier magnétique**

**Présentation disponible**

# Prediction of fume formation in a pulsed gas metal arc welding process by means of 2D time-dependant arc model coupled with nanoparticle tracking

M. Boselli, V. Colombo, E. Ghedini, M. Gherardi, P. Sanibondi (Bologne, Italie)

**Objectifs:** prédiction des formations des fumées (procédés de soudage)

**Mots Clés:** plasmas thermiques, pulsés, soudage, synthèse de nanoparticules, modèles

**Constat:** problème de protection des humains avec l'inhalation des fumées dans les procédés de soudage. Réduction des fumées et compréhension de leur formation et propagation.

**Comment:** développement d'un modèle couplant méthode des volumes VoF (modèle axisymétrique 2D temporel incluant le détachement des gouttelettes et la production de vapeurs métalliques) + méthode des moments MoM (modèle de formation des fumées et de transport des fumées)

**Modèle:**

Cebora Sound MIG 5040/TD double pulse source
1mm de diamètre pour le fil d'acier, 5m/min
Pic de courant de 350A jusqu'à 30A
Période de 9ms
Argon 10l/min
Distance pièce-tip : 15mm (longueur de l'arc 4mm et longueur totale 11mm)

***Equations classiques d'un modèle***

+ conservation des vapeurs métalliques (production issue de l'évaporation des nanoparticules et pertes de ½ par reformation des nanoparticules)
+ effet Thomson
chaleur spécifique de fusion, production de vapeurs métalliques
+ turbulence négligée
formation nanoparticules et dynamique aérosol.

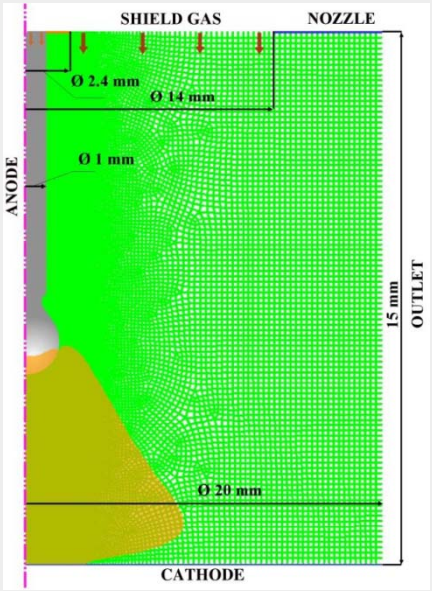

**Présentation disponible**

# Prediction of fume formation in a pulsed gas metal arc welding process by means of 2D time-dependant arc model coupled with nanoparticle tracking

M. Boselli, V. Colombo, E. Ghedini, M. Gherardi, P. Sanibondi (Bologne, Italie)

**Résultats:** **T, $V_{gas}$, concentration de vapeurs, de nanoparticules en fonction du temps.**

**Apres une centaine de pulses : pic à 350A.**

- $T_{max}$=**7000K**, arc diffus, fil partiellement fondu, forme sphérique des gouttes, vapeurs métalliques proche de la zone d'évaporation de la tip et proche surface sans induire de refroidissement notable
- $V_{plasma}$=**15m/s**
- Vapeurs formées au niveau de la fil-pointe, puis transportées vers les bords par convection et diffusion et converties en nanoparticules. Distribution avec T moyenne de 2000K, et **0.5µg/mm³s** proche tip, et **0.05 µg/mm³s** proche pièce.
- Fumées formées dans les bords, proche de la pièce (là où les vapeurs métalliques sont transportées par convection)
- Comportement périodique du détachement des gouttes et du transfert des vapeurs.
- Les nanoparticules sont formées dans les régions proches de la pièce, transportées par convection radiale et converties. Celles produites proches de la tip sont aspirées par les régions chaudes où elles deviennent vapeurs.

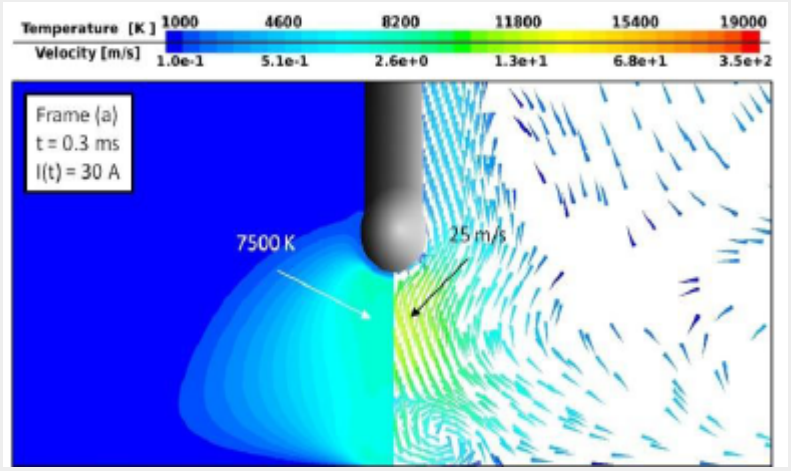


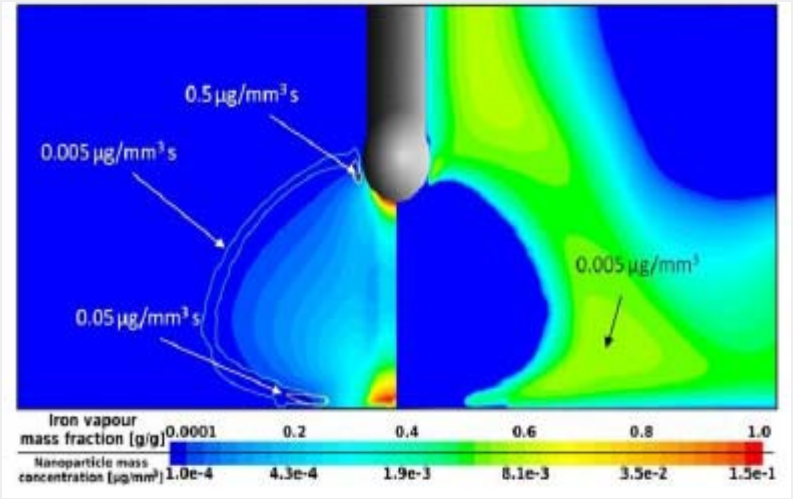

**Présentation disponible**

# Prediction of fume formation in a pulsed gas metal arc welding process by means of 2D time-dependant arc model coupled with nanoparticle tracking

M. Boselli, V. Colombo, E. Ghedini, M. Gherardi, P. Sanibondi (Bologne, Italie)

**Résultats:** **T, $V_{gas}$, concentration de vapeurs, de nanoparticules en fonction du temps.**

**2ms après le pulse : chute du courant à 30A.**

- T environ **12500K**, arc moins étendu, surtout convection
- $V_{plasma}$=**40m/s**
- Concentration de vapeurs surtout sur l'axe de la torche
- max de **0.3 µg/mm³s** nanoparticules proche pièce, **$2.10^{-2}$** ailleurs autour
- Production de 1 à 11 mg/s (moyenne de 5,5mg/s)

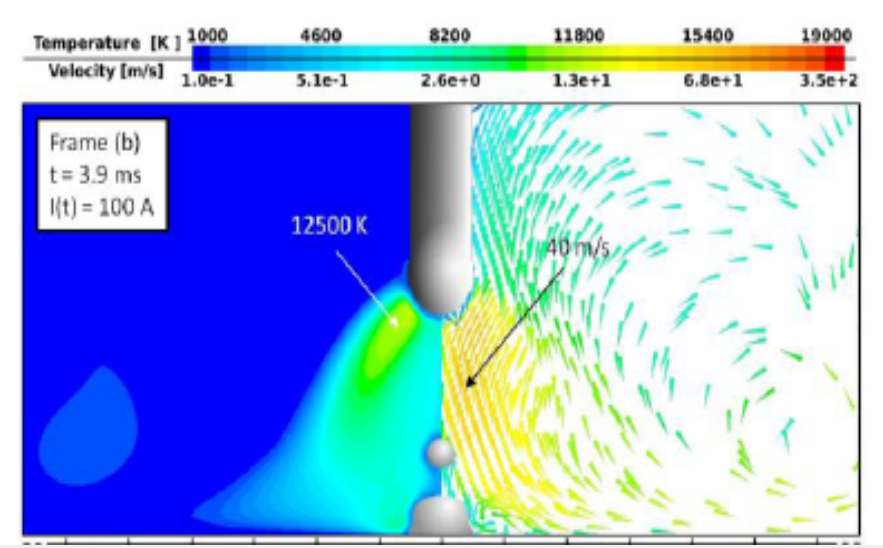


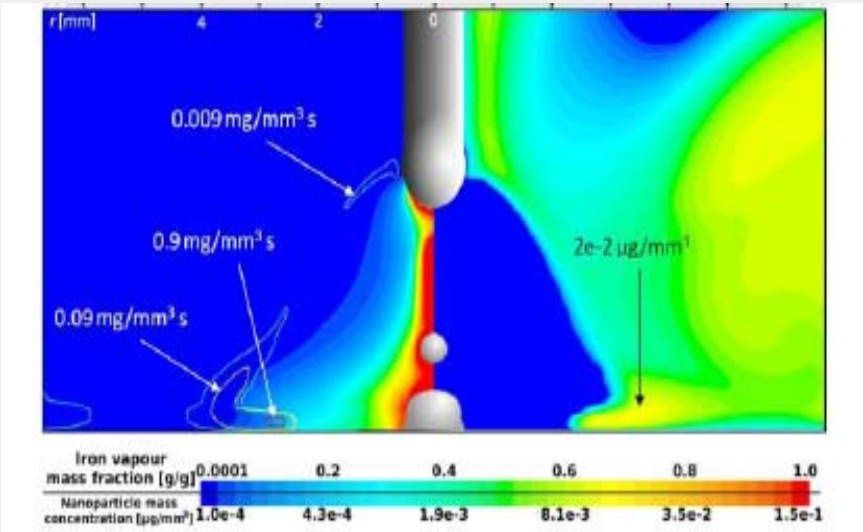

# 3D modeling and simulation of arc deflection behavior in vacuum interrupters with consideration of external circuits

L.Wang, X.Huang, Z.Qian, S.Jia, Z.Shi (Xian, Chine)

**Objectifs:** Efficacité de l'interruption dans des appareils de coupure dans le vide. Etude de la déflection sous un champ B total dans différente direction.

**Mots Clés:** arc dans le vide, 3D modèle, déflection, TMF et AMF (Transverse, Axial Magnétique Field)

**Constat:** les arcs dans le vide sont contrôlés par le champ magnétique axial (AMF). Une fois connecté au réseau, ils sont perturbés par le $B_{ext}$ ce qui entraine sa déflection + érosion des électrodes. Cette déflection réduit de 20% l'efficacité du procédé et provoque des échecs. Modèle 2D insuffisant.

**Comment:** Modèle 3D

**Modèle:**
3D, Fluent Ansys, $B_{total}$
$\phi_{électrodes}$=10mm, $d_{inter\text{-}électrodes}$=10mm
I=25kA, cuivre, TMF champ B uniforme

***Equations classiques d'un modèle***
+ Rayonnement NEC

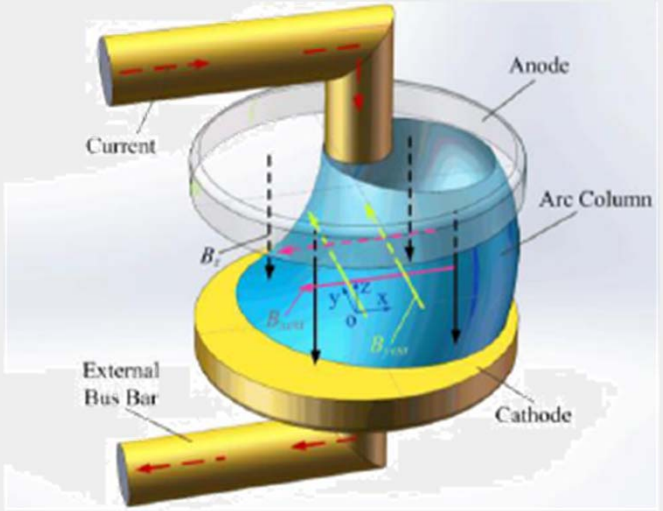


Fig.1 3D physical model of deflection behavior of vacuum arc subjected to global magnetic fields by AMF and magnetic field

# 3D modeling and simulation of arc deflection behavior in vacuum interrupters with consideration of external circuits

L.Wang, X.Huang, Z.Qian, S.Jia, Z.Shi (Xian, Chine)

## Vitesse de l'arc (à z=5mm pour les cercles)

$B_{xext}=B_{yext}=0$ | $B_{xext}$=-20mT, $B_{yext}$=0mT | $B_{xext}$=0mT, $B_{yext}$=-20mT | $B_{xext}$=-20mT, $B_{yext}$=20mT

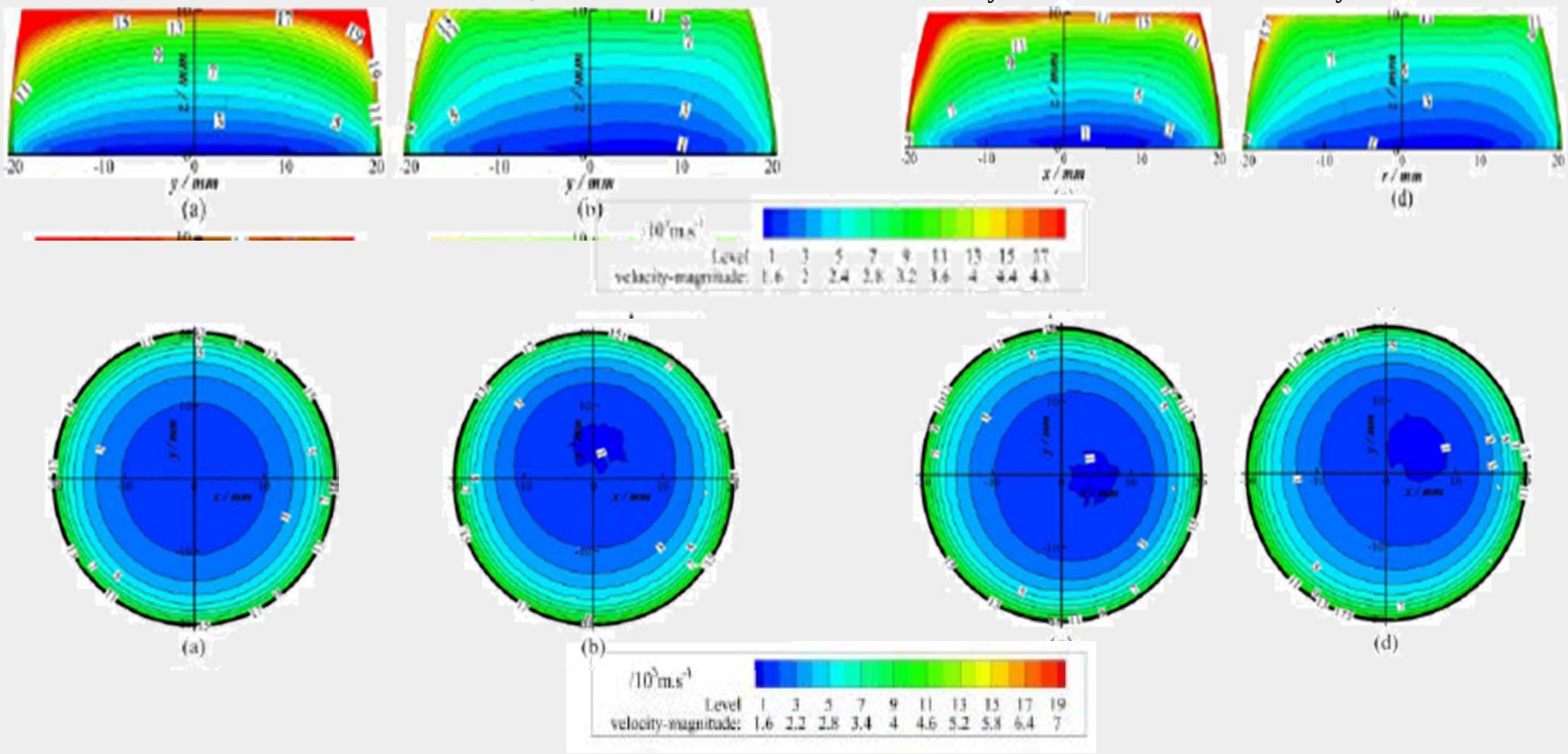


**Résultats :**

La position de déflection ↑ avec ↑ TMF, Distribution des vitesses ≅ distribution du nombre de MACH

# 3D modeling and simulation of arc deflection behavior in vacuum interrupters with consideration of external circuits

L.Wang, X.Huang, Z.Qian, S.Jia, Z.Shi (Xian, Chine)

## Pression de l'arc (à z=5mm pour les cercles)

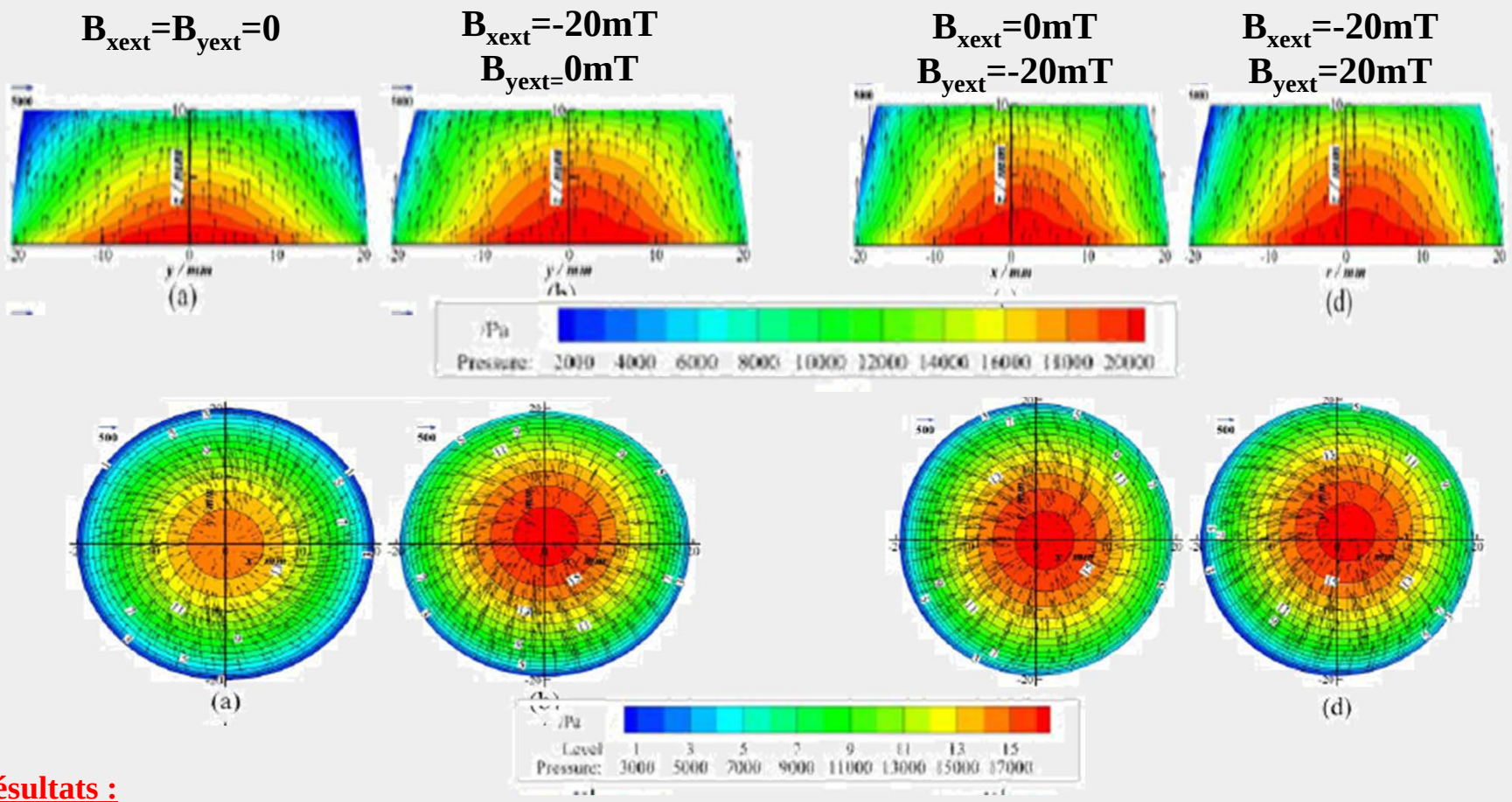


**Résultats :**

Arc déflecté par le courant généré par le TMF, force Ampère.

TMF (selon x, $B_{ext}<0$) arc déflecté vers y>0, TMF (selon y, $B_{yext}>0$) arc deflecté vers x>0, si $|B_{xext}>0|=|B_{yext}<0|$, tourne autour du centre

# 3D modeling and simulation of arc deflection behavior in vacuum interrupters with consideration of external circuits

L.Wang, X.Huang, Z.Qian, S.Jia, Z.Shi (Xian, Chine)

## Température des ions et électrons (à z=5mm pour les cercles)

$B_{xext}=B_{yext}=0$ | $B_{xext}$=-20mT, $B_{yext}$=0mT | $B_{xext}$=0mT, $B_{yext}$=-20mT | $B_{xext}$=-20mT, $B_{yext}$=20mT

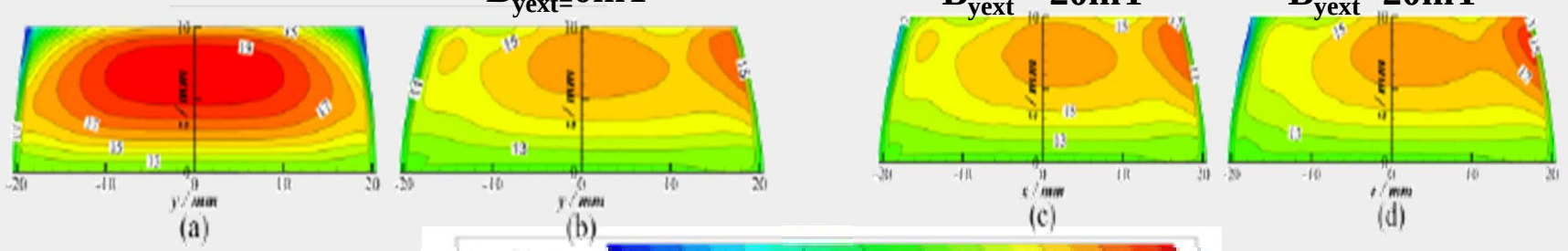


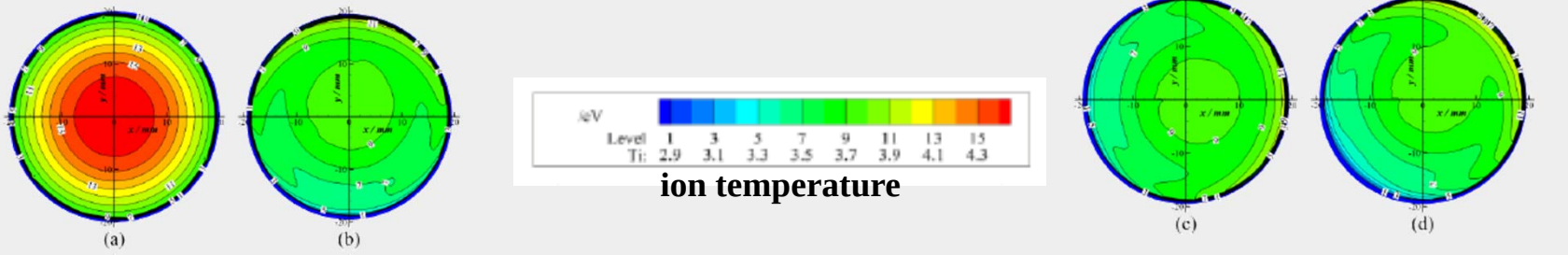


ion temperature

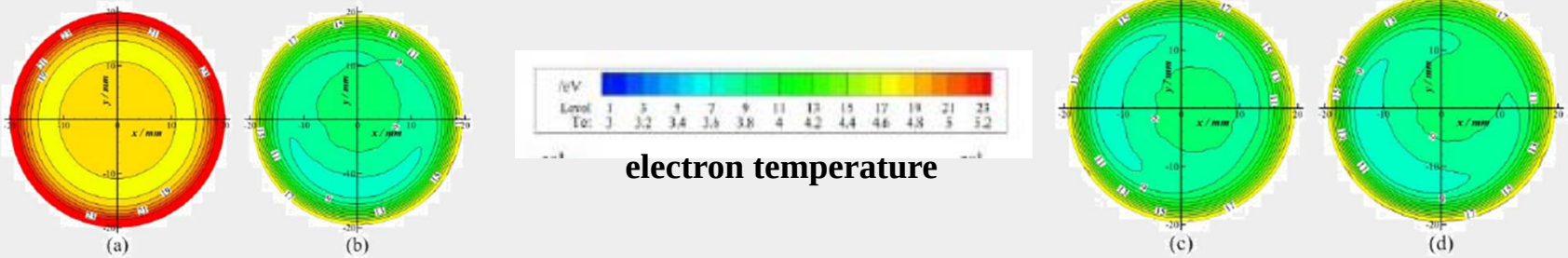


electron temperature

# Quantitative elemental analysis by laser-induced breakdown spectroscopy

T.Tanaka, S. Harada, T. Ikegami, F. Mitsugi (Kumamoto, Japon)

## Introduction

Laser-induced breakdown spectroscopy (LIBS) has been popular as elemental analysis due to advantages, however it has disadvantages to be solved.

Advantage
- Pre-preparation of sample is unnecessary
- *In-situ* rapid analysis with low cost

Disadvantage
- Inferior to the conventional element analysis methods such as AAS, XRF in accuracy and sensitivity

## Research purposes

- To develop a compact LIBS system for on site analysis
- To improve accuracy of composition analysis by LIBS

## Experimental method

- We have analyzed the elemental composition of metal alloy and metal oxide using LIBS with a small spectrometer.
- To improve low-resolution spectral data, various computational processing are applied to data.
- To estimate quantitative elemental composition, theoretical spectral intensity was calculated and fitted to observed spectrum.
- To evaluate LIBS results, XRF was used as reference.

Theoretical spectral emission intensity

$$I(\lambda)=\frac{8\pi hc}{\lambda^5}e^{\frac{(E_2-E_1)}{kT}}\left(1-\exp\left[-\frac{\sqrt{\ln 2}}{4\pi\sqrt{\pi}}\frac{\lambda^2}{\Delta\nu_D}\frac{g_k A_{ki} N}{U(T)}e^{-\frac{E_i}{kT}}K(a,x)\ell\right]\right)$$

| | |
|---|---|
| $\lambda$ : transition wavelength | $h$ : Plank's constant |
| $E_k, E_i$ : energy of the states(k,i) | $k$ : Boltzmann constant |
| $g_k$ : degeneracy of the states(k,i) | $A_{ki}$ : transition probability |
| $U(T)$ : partition function | $N$ : number density |
| $T$ : plasma temperature | $K(a,x)$ : Voigt function |

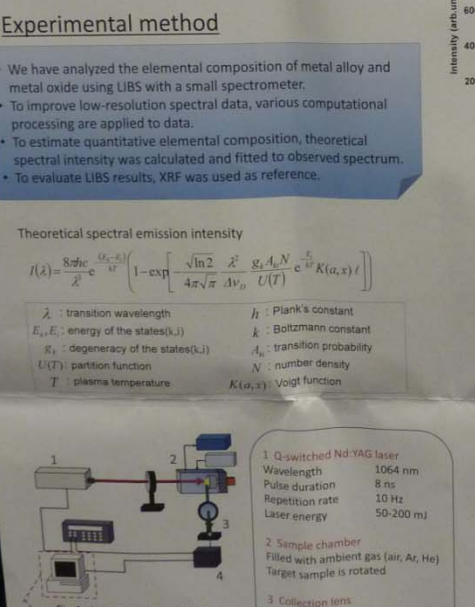


Fig.1 LIBS experimental setup

Control program (using LabVIEW)
- Acquire and analyze LIBS spectra
- Detect peaks in LIBS spectra and identify atomic and ionic lines

Spectrum processing
- Removing the outlier, averaging
- Convolution(calculated spectrum)

1 Q-switched Nd:YAG laser

| | |
|---|---|
| Wavelength | 1064 nm |
| Pulse duration | 8 ns |
| Repetition rate | 10 Hz |
| Laser energy | 50-200 mJ |

2 Sample chamber
Filled with ambient gas (air, Ar, He)
Target sample is rotated

3 Collection lens
Emission light from the target surface was collected by lens ($f$=150mm) and transferred using a quartz optical fiber into the USB spectrometer

4 USB spectrometer(USB4000)
Trigger delay time, gate width is adjusted by the delayed pulse generator

Kumamoto University

## Results and Discussion

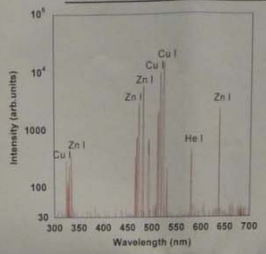


Spectral peaks are identified as emission from elements of Cu, Zn. The composition ratio of brass is Cu : Zn = 65.4 : 34.6 it seems definitely accurate.
The metal atoms composition ratio is Cu : Zn = 68.8 : 31.2, which is close to that estimated by XRF.

Fig.2 LIBS spectrum of brass.

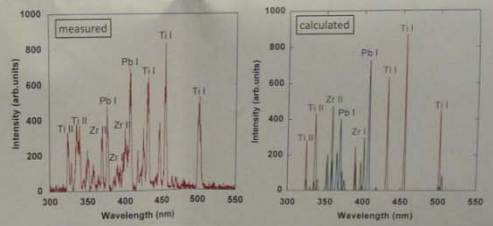


Fig.3 LIBS spectrum of PZT(left) and calculated spectrum (right).

The composition ratio of the PZT is Pb : Zr : Ti : O = 18 : 18: 9 : 55 and it seems definitely accurate. Since oxygen atoms are contained in both the PZT sample and the ambient air, oxygen atoms are excluded in the calculation. Excluding oxygen component, the metal atoms composition ratio is Pb : Zr : Ti = 38 : 39: 23, which is close to that measured by XRF.


Fig.4 Composition of PZT measured by LIBS(left) ,XRF(right)

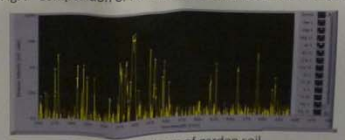

Fig.5 LIBS spectrum of garden soil.

Many spectral peaks are well identified as emission from elements of Na, Mg, Al, Ca, Ti, Fe, V. However there are some unknown peaks because the spectral resolution of the spectrometer is low and some spectral lines overlap within the instrumental width.

## Conclusions

- In the case of simple composition sample such as brass and PZT, the composition ratios obtained by LIBS showed a relatively good agreement with those by XRF.
- In the soil sample, most of elements can be detected from its LIBS spectrum, however, agreement with XRF result was poor.

# Understanding and Suppression of Magnetic Arc Blow in Plasma Arc Cutting Torch

uesugi@ec.t.kanazawa-u.ac.jp

Takeru ITO[1], Yusuke KATADA[1], Yoshihiko UESUGI[1, 2], Yasunori TANAKA[1, 2], Tatsuo ISHIJIMA[2], and Yoshihiro YAMAGUCHI[3]

[1]Faculty of Electrical & Computer Engineering, Kanazawa University, [2]Research Center for Sustainable Energy & Technology, Kanazawa University, [3]Komatsu Industries Corp.

## troduction

**lasma arc cutting system**
widely used in metal cutting

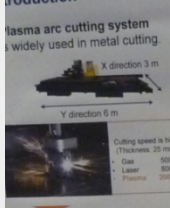







Cutting speed is high (Thickness 25 mm)
- Gas 500 mm/min
- Laser 800 mm/min
- Plasma 2000 mm/min

**Application**

Construction machinery, transport machinery, building bridge, plant, factory, ship, railway, etc.

**Problem : Magnetic arc blow** When a magnetized steel plank is cut, the electromagnetic force induced by magnetic flux leakage in the cutting edge deflects the arc plasma jet.

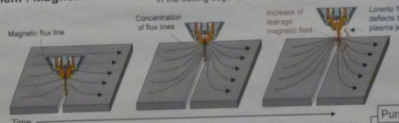


Causes of the steel magnetization
- Transportation by lifting magnet.
- Rolling and heat treatment.

Steel plank that causes the magnetic arc blow
- Large plank with a few meters square.
- High-tensile steel containing Ni or Co.

- It takes time and money to demagnetize a large steel plank.
- Suppression of magnetic arc blow by means of developing process design of the plasma torch is required.

Current status of magnetic arc blow
- Little physical details have emerged on the magnetic arc blow in plasma arc cutting.
- The increased occurrence of the phenomenon is expected by the development and use of high-tensile steel that is easy to magnetization.

- Understanding of the magnetic arc blow and establishment of suppression technique are strongly required.

Problems caused by the magnetic arc blow
- Abnormal damages of the nozzle and the shield cap.
- Poor cutting quality.

Double arc
- Bifurcation of the arc column.
- It damages the nozzle parts.

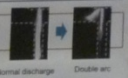


**Purpose of this study**

Physical understanding and suppression of magnetic arc blow.

**Experimental methods**

We applied external magnetic field to the plasma jet and performed following experiments.

Experiment 1: Magnetic field application by electromagnets.
- Artificial reproduction of magnetic arc blow by external magnetic field.
- Examination for the relationship among operating conditions, such as arc current, gas flow rate and so on, and occurrence of the double arc.

Experiment 2: Cutting test for the magnetized steel plank.
- Magnetic shielding on the torch was used to suppress the double arc.

## Applying external magnetic field to the plasma jet

### Plasma torch and electromagnets

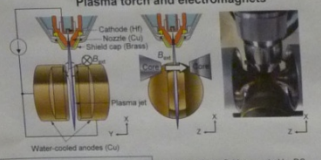


| Experimental conditions | |
|---|---|
| Arc current | 135 A |
| Main gas | $O_2$, 7 – 20 L/min |
| Assist gas | $N_2$, 30 L/min |
| Hf cathode diameter | 1.6 mm |
| Nozzle diameter | 1.3 mm |
| Shield cap diameter | 3.0 mm |

- The magnetic field generated by DC electromagnets was applied to the plasma jet to generate the magnetic arc blow.
- Magnetic field is oriented perpendicular to the plasma jet.

### Double arc generation by external magnetic field

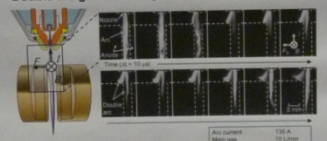


| | |
|---|---|
| Arc current | 135 A |
| Main gas | 10 L/min |
| Assist gas | 20 L/min |
| Magnetic flux density | 20 mT |
| Frame rate | 100,000 fps |
| Shutter speed | 0.5 μs |

Double Arc occurred when the external magnetic field was increased to 20 mT.
- External magnetic field was applied after arc ignition.
- The deflected plasma jet came into contact with the nozzle orifice.
- Multiple abnormal discharges are formed through the nozzle.
- Torch parts (Nozzle, shield cap, cathode) were damaged.

### Arc voltage fluctuation caused by double arc

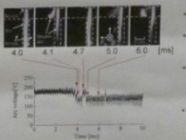


- Double arc time: Arc voltage dropped.
- After double arc extinction: Arc voltage recovered.
- Resistance between the electrodes decreased by forming other current paths.
- Arc voltage drops can be used as an indicator whether the double arc occurs.

Arc current is controlled to a constant value by the power source.

### Threshold magnetic flux density for the double arc occurrence $B_{th}$

Arc current: 40 A - 135 A
Main gas flow rate: 5 - 25 L/min

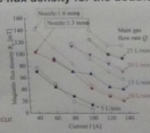


$B_{th}$ has a strong dependence on the arc current and main gas flow rate.

Increase in arc current
- Increase in Lorentz force $j \times B$
- $B_{th}$ declines.
  Double arc become easy to occur.

Increase in gas flow rate
- Deflected plasma jet is pushed back by cold gas.
- $B_{th}$ is high.
  The double arc hardly occurs.

From the experimental data, $B_{th}$ [mT] is empirically given by the following equation.

$$B_{th} = 778 \times Q^{1.1} \times I^{-1.2}$$

where $Q$ [L/min] is main gas flow rate, $I$ [A] is arc current. $B_{th}$ is approximately proportional to $Q$ and inversely proportional to $I$.

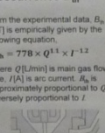


Large diameter of the nozzle orifice
- Distance between plasma jet and the nozzle orifice is long.
- $B_{th}$ is high.
  The double arc hardly occurs.

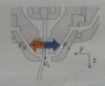

While Lorentz force deflects the arc plasma, the axial flow velocity acts as a restoring force that push back the arc plasma.

$$F_B \propto u_z \frac{\partial u_z}{\partial z}$$

### Arc plasma behavior in the nozzle

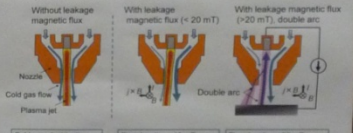


| Cold gas electrically insulates the plasma jet from the nozzle. | Flux density: ~ 10 mT<br>• Arc plasma is deflected.<br>• Arc plasma does not contact with the nozzle.<br>• Double arc is not generated. | Flux density: > 20 mT<br>• Arc plasma comes into contact with the nozzle.<br>• Formation of abnormal discharges.<br>• Double arc occured. |
|---|---|---|

## Demonstration of steel cutting with and without magnetization

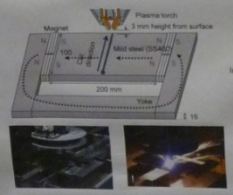





In the images of the second and subsequent, arc plasma was disturbed and the double arc was generated. The plank was separated after plasma cutting and the cut surface was observed.

| | |
|---|---|
| Arc current | 150 A |
| Main gas | 13 L/min |
| Assist gas | 25 L/min |
| Torch height | 2.5 mm |
| Nozzle orifice diameter | 1.6 mm |
| Magnetic flux density at the torch height | 30 mT |
| Frame rate | 250 fps |
| Shutter speed | 0.1 ms |

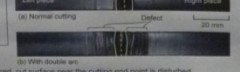


If double arc has occurred, cut surface near the cutting end point is disturbed.


| | |
|---|---|
| Arc current | 150 A |
| Main gas | 0.45 ~0.65 MPa, $O_2$ |
| Assist gas | 25 L/min, Air |
| Nozzle diameter | 1.6 mm |
| Torch height | 2.5 mm |
| Frame rate | 250 fps |
| Shutter speed | 1/100000 s |

With decreasing gas flow rate, $B_{th}$ decreases.
This trend is similar to the previous experiment with external magnetic field by electromagnets.

## Proposed solution for double arc suppression

### Magnetic shielding on the torch

We tried a method of less susceptible to magnetic field with magnetic shielding on the plasma torch.

At the torch height: ~ 100 mT
Inside the cutting groove: ~ 600 mT

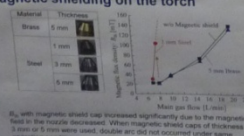


$B_{th}$ with magnetic shield cap increased significantly due to the magnetic field in the nozzle decreased. When magnetic shield caps of thickness 3 mm or 5 mm were used, double arc did not occurred under same operating conditions.

Magnetic shielding on the torch can suppress the occurrence of the double arc. Ferromagnetic material having thickness is effective.

The cross section without magnetic shielding (a) has poor cutting quality near the end point. When the cutting point approaches the end of the plank, the magnetic field in the plank is concentrated in the uncut part, and leakage magnetic field near the torch increases.


Cut surface with magnetic shielding is smooth due to the absence of double arc.

## Conclusions

To predict and prevent the occurrence of magnetic arc blow, we examined the relationship between operating conditions and the occurrence of the abnormal discharges called "Double arc".

- Threshold magnetic flux density for the double arc occurrence $B_{th}$ has a strong dependence on the arc current and main gas flow rate.
- With increasing arc current, $B_{th}$ decreases because arc plasma is more deflected by the Lorentz force.
- $B_{th}$ also decreases with decreasing main gas flow rate because the electrical insulation between the plasma jet and the nozzle become less effective.
- If the nozzle diameter is small, the deflected arc plasma is likely to contact with the nozzle wall.
- Magnetic shielding on the torch is effective to suppress the double arc without changing operating conditions.

# 3D modeling and simulation of arc deflection behavior in vacuum interrupters with consideration of external circuits

**Lijun Wang, Xiaolong Huang, Zhonghao Qian, Shenli Jia, Zongqian Shi**

State Key Laboratory of Electrical Insulation and Power Equipment, Xi'an Jiaotong University, Xi'an, 710049, China

## INTRODUTION

Vacuum arcs widely appear in many fields, such as coating and depositions, vacuum interrupters (VIs), vacuum ion sources and pulsed power technology, and so on. Axial magnetic fields (AMFs) always are used to make VAs keep in the diffuse status, which also makes AMFs become the most popular technology in commercial VIs. However, actual VIs are connected in the power system through external circuits, which will generate transverse magnetic field (TMF), which is vertical to VAs. So, actual VAs always are not only subjected to AMFs, but also external TMFs. This kind of TMFs will lead to deflected VAs and electrode erosion. Many interruption failure of VIs is related to the deflected erosion of electrode.

## 3D MODEL OF VA DEFLECTION BEHAVIORS UNDER GLOBAL MAGNET FIELDS

The 3D physical model of deflection behavior of vacuum arc subjected to global magnetic fields by AMF (shown in Fig.2) and magnetic field generated by external bus bar or nearboring phase (TMF is assumed to be uniform) is shown in Fig.1, mathematical model is based on two-fluid theory and Maxwell equations and is shown in right box.

### Physical Model:

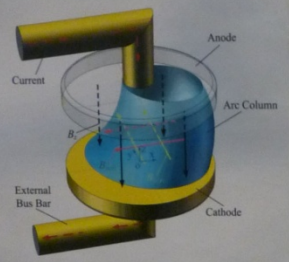


Fig.1 3D physical model of deflection behavior of vacuum arc subjected to global magnetic fields by AMF and magnetic field generated by external bus bar or nearboring phases

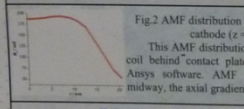

Fig.2 AMF distribution between anode and cathode (z = 5mm)

This AMF distribution is generated by the coil behind contact plate, and calculated by Ansys software. AMF distribution is from midway, the axial gradient is not considered.

**Related experimental results**

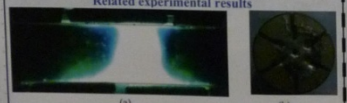

(a) (b)

Fig.3 Experimental results about electrode deflected erosion (a) Image of deflected arc column; (b) Deflected anode erosion (Electrode diameter: 58mm; gap distance: 16mm; Arc current: 20kA (rms); peak-value current moment)

### Mathematical Model:

Mass eqution:

$$\frac{\partial n_i u_{ix}}{\partial x}+\frac{\partial n_i u_{iy}}{\partial y}+\frac{\partial n_i u_{iz}}{\partial z}=0 \tag{1}$$

Ion momentum equation along $x$, $y$ and $z$ direction respectively:

$$m_i n_i\left(u_x\frac{\partial u_{ix}}{\partial x}+u_y\frac{\partial u_{ix}}{\partial y}+u_z\frac{\partial u_{ix}}{\partial z}\right)=\left[j_y(B_z+B_{zext})-j_z(B_y+B_{yext})\right]-\left(\frac{\partial n_i kT_i}{\partial x}+\frac{\partial n_e kT_e}{\partial x}\right)+\nabla\cdot(\vec{\tau}_i)_x \tag{2}$$

$$m_i n_i\left(u_x\frac{\partial u_{iy}}{\partial x}+u_y\frac{\partial u_{iy}}{\partial y}+u_z\frac{\partial u_{iy}}{\partial z}\right)=\left[j_z(B_x+B_{xext})-j_x B_z\right]-\left(\frac{\partial n_i kT_i}{\partial y}+\frac{\partial n_e kT_e}{\partial y}\right)+\nabla\cdot(\vec{\tau}_i)_y \tag{3}$$

$$m_i n_i\left(u_x\frac{\partial u_{iz}}{\partial x}+u_y\frac{\partial u_{iz}}{\partial y}+u_z\frac{\partial u_{iz}}{\partial z}\right)=\left[j_x(B_y+B_{yext})-j_y(B_x+B_{xext})\right]-\left(\frac{\partial n_i kT_i}{\partial z}+\frac{\partial n_e kT_e}{\partial z}\right)+\nabla\cdot(\vec{\tau}_i)_z \tag{4}$$

Ion energy equation:

$$\nabla\cdot(\vec{u}(m_i n_i E_i+p_i))=\nabla\cdot(\lambda_i\nabla T_i)+\nabla\cdot(\vec{\tau}_i\cdot\vec{u})+Zen_i\vec{u}\cdot\vec{E}+\frac{3km_i n_e\nu_{ei}}{m_i}(T_e-T_i)+\vec{u}\cdot\left(-\frac{n_i e}{\sigma}\vec{j}+g_T n_e k\nabla T_e\right) \tag{5}$$

Electron energy equation:

$$\nabla\cdot(\vec{v}(n_e m_e E_e+p_e))=\nabla\cdot\left(\frac{3}{2}\vec{j}\cdot\frac{kT_e}{e}+\lambda_e\nabla T_e\right)-\frac{3km_i n_e\nu_{ei}}{m_i}(T_e-T_i)+\frac{j_x^2+j_y^2+j_z^2}{\sigma}-P_{radiation} \tag{6}$$

Current density:

$$\vec{j}=en_e(\vec{u}-\vec{v}) \tag{7}$$

Magnetic field transport equation along $x$ and $y$ direction respectively:

$$-\nabla\cdot\left(\frac{1}{\mu_0\sigma}\nabla B_x\right)=\frac{\partial}{\partial y}\left[v_z(B_x+B_{xext})-v_x(B_z+B_{zext})\right]-\frac{\partial}{\partial z}\left[v_x(B_y+B_{yext})-v_y B_x\right]-\frac{1}{en_e^2}\left(\frac{\partial n_e}{\partial y}\frac{\partial p_e}{\partial z}-\frac{\partial n_e}{\partial z}\frac{\partial p_e}{\partial y}\right) \tag{8}$$
$$-\frac{1}{\mu_0\sigma^2}\left[\left(\frac{\partial B_z}{\partial z}-\frac{\partial B_z}{\partial x}\right)\cdot\frac{\partial\sigma}{\partial z}-\left(\frac{\partial B_x}{\partial x}-\frac{\partial B_x}{\partial y}\right)\cdot\frac{\partial\sigma}{\partial y}\right]+\frac{1}{\mu_0\sigma^2}\left(\frac{\partial\sigma}{\partial x}\frac{\partial B_x}{\partial x}+\frac{\partial\sigma}{\partial y}\frac{\partial B_x}{\partial y}+\frac{\partial\sigma}{\partial z}\frac{\partial B_x}{\partial z}\right)$$

$$\nabla\cdot\left(\frac{1}{\mu_0\sigma}\nabla B_y\right)=\frac{\partial}{\partial z}\left[v_y B_z-v_z(B_y+B_{yext})\right]-\frac{\partial}{\partial x}\left[v_z(B_y+B_{yext})-v_y(B_x+B_{xext})\right]-\frac{1}{en_e^2}\left(\frac{\partial n_e}{\partial z}\frac{\partial p_e}{\partial x}-\frac{\partial n_e}{\partial x}\frac{\partial p_e}{\partial z}\right) \tag{9}$$
$$-\frac{1}{\mu_0\sigma^2}\left[\left(\frac{\partial B_z}{\partial x}-\frac{\partial B_x}{\partial y}\right)\cdot\frac{\partial\sigma}{\partial x}-\left(\frac{\partial B_y}{\partial y}-\frac{\partial B_y}{\partial z}\right)\cdot\frac{\partial\sigma}{\partial z}\right]+\frac{1}{\mu_0\sigma^2}\left(\frac{\partial\sigma}{\partial x}\frac{\partial B_z}{\partial x}+\frac{\partial\sigma}{\partial y}\frac{\partial B_y}{\partial y}+\frac{\partial\sigma}{\partial z}\frac{\partial B_z}{\partial z}\right)$$

Current density:

$$j_x=\frac{1}{\mu_0}\left(\frac{\partial B_z}{\partial z}-\frac{\partial B_z}{\partial y}\right),\ j_y=\frac{1}{\mu_0}\left(\frac{\partial B_x}{\partial x}-\frac{\partial B_x}{\partial z}\right),\ j_z=\frac{1}{\mu_0}\left(\frac{\partial B_y}{\partial y}-\frac{\partial B_y}{\partial x}\right) \tag{10}$$

## RESULTS

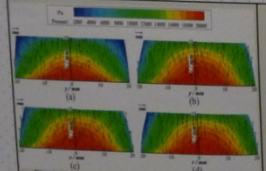

Fig.4 Contours of plasma pressure of vacuum arc subjected to global magnetic fields along some cross-sections plane (a) $B_{xext}=B_{yext}=0$; (b) $B_{xext}$ = -20mT, $B_{yext}$ = 0mT; (c) $B_{xext}$ = 0mT, $B_{yext}$ = 20mT; (d) $B_{xext}$ = -20mT, $B_{yext}$ = 20mT

From Fig.4 and Fig.5, it can be seen that the vacuum arc plasma is deflected by the Ampere force generated by the action of TMF arc current. The ion velocity deflection also can be seen.

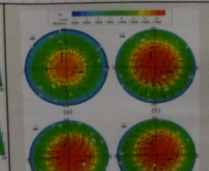

Fig.5 Plasma pressure contours of vacuum arc subjected to global magnetic fields on $z$ = 5mm plane (a) $B_{xext}=B_{yext}=0$; (b) $B_{xext}$ = -20mT, $B_{yext}$ = 0mT; (c) $B_{xext}$ = 0mT, $B_{yext}$ = 20mT; (d) $B_{xext}$ = -20mT, $B_{yext}$ = 20mT ($r$ is the direction of 45° from $x$ to $y$ coordinate axis)

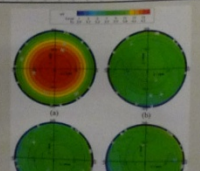

Fig.6 Contours of ion temperature of vacuum arc subjected to glogal magnetic fields on $z$ = 5mm plane (a) $B_{xext}=B_{yext}=0$; (b) $B_{xext}$ = -20mT, $B_{yext}$ = 0mT; (c) $B_{xext}$ = 0mT, $B_{yext}$ = 20mT; (d) $B_{xext}$ = -20mT, $B_{yext}$ =20mT ($r$ is the direction of 45° from $x$ to $y$ coordinate axis)

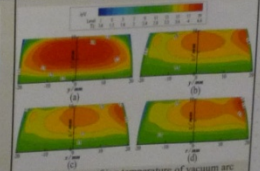

Fig.7 Contours of ion temperature of vacuum arc subjected to global magnetic fields along some cross-sections plane (a) $B_{xext}=B_{yext}=0$; (b) $B_{xext}$ = -20mT, $B_{yext}$ = 0mT; (c) $B_{xext}$ = 0mT, $B_{yext}$ = 20mT; (d) $B_{xext}$ = -20mT, $B_{yext}$ = 20mT

In Fig.6 and Fig.7, ion temperature distribution deflected by Ampere force. In Fig.6, (a) and Fig.7, (a), TMF is not considered, also, in this case, arc radiation is not considered in the model, that is why the ion temperature in (a) is higher than (b), (c) and (d).

## CONCLUSIONS

In this paper, the deflection effect of VAs subjected to global magnetic field, including AMFs and TMF along different directions is modeled and simulated. Simulation results show that external TMF will lead to deflection of VA, and plasma parameters also are deflected. The deflected direction of plasma parameters in vacuum arc obeys left hand rule. When external TMF is along minus $x$ direction, arc plasma deflects toward $y$ direction. And when external TMF is along $y$ direction, arc plasma deflects toward $x$ direction. When the above composite TMFs is added on arc column, the vacuum arc is deflected toward center line between $x$ and $y$ positive directions.

# EXPERIMENTAL INVESTIGATION ON THE EFFECTS OF THE GAS MIXTURES IN PLASMA ARC CUTTING OF AUSTENITIC STAINLESS STEEL

M. Boselli[2], L. Ceschini[1,2], V. Colombo[1,2], E. Ghedini[1,2], M. Gherardi[1], F. Rotundo[2], P. Sanibondi[1], S. Dallavalle[3], R. Fazzioli[3], M. Vancini[3]

[1] Department of Industrial Engineering (D.I.N.)
[2] Industrial Research Centre for Advanced Mechanics and Materials (C.I.R.I.-M.A.M.)
Alma Mater Studiorum-Università di Bologna, via Saragozza 8, 40123 Bologna, Italy
[3] Cebora S.p.A., via Andrea Costa 24, 40057 Cadriano di Granarolo, Italy
e-mail: vittorio.colombo@unibo.it

ALMA MATER STUDIORUM
UNIVERSITÀ DI BOLOGNA

CEBORA welding&cutting

BUILDING OUR FUTURE TOGETHER

## ABSTRACT

***Plasma Arc Cutting (PAC)*** *is a process for cutting metallic sheets with thickness in the range of 1 -150 mm in which a thermal plasma arc is ignited between a thermionic cathode that is enclosed in the plasma torch and the workpiece which works as the anode. In the last decades significant increase in the quality of the cut, on the maximum cutting speed and in the reduction of the wear rate for torch consumables have been achieved.*
*An important role in the optimization of the PAC process is played by the choice of the* ***working gas mixtures*** *that can be tuned depending on the cutting material, thickness and operating current as to obtain the maximum performance.*
*In this work the effects of different mixtures* ***(Ar/H2/N2 as plasma gas and N2 as shield gas)*** *on the performance of AISI 304L* ***austenitic stainless steel cutting*** *has been investigated experimentally focusing on cut quality and cutting speed. Experiments have been performed using a plasma arc cutting torch working at* ***400 A****. Results show that adding N2 to the H35 mixture (35% H2 and 65% Ar) in the plasma gas it is possible to reach higher cutting speed than using pure H35, however the presence of N2 or entrained ambient Air in the plasma arc column can modify the surface chemical composition and microstructural properties of the kerf surface negatively influencing machinability and weldability.*
***Microstructural analysis*** *of the kerf surface has been performed by means of scanning electron microscopy (SEM) with energy dispersive microprobe (EDS) for* ***localized elemental analysis****, as to understand how the PAC operating parameters and the use of different mixtures can affect the surface condition of the workpiece material, that affects its machinability and weldability.*

## EXPERIMENTAL SETUP

A **PROTOTYPAL CEBORA PLASMA TORCH** EQUIPPED WITH A GAS MIXING UNIT ABLE TO PROVIDE ARBITRARY MIXTURES HAS BEEN USED.

ALL TESTS HAVE BEEN PERFORMED AT **400 A CURRENT** USING **PURE $N_2$ AS SHIELDING GAS**.

THE STAINLESS STEEL (SS) USED IN THIS WORK IS THE WIDELY USED **AISI 304L**.

TYPICAL STAINLESS STEEL CUTTING SPEED FOR 400A PLASMA TORCH

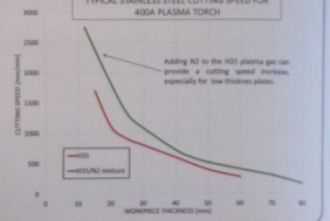


## OPERATING CONDITIONS

| Sample | Plasma gas | Shield gas | Cutting speed [mm/min] | Plate thickness [mm] |
|---|---|---|---|---|
| A | H35 | N2 | 2000 | 15 |
| B | H35 30% + N2 70% | N2 | 2000 | 15 |
| C | H35 70% + N2 30% | N2 | 2000 | 15 |
| D | H35 | N2 | 1125 | 25 |
| E | H35 | N2 | 900 | 30 |
| F | H35 30% + N2 70% | N2 | 520 | 50 |

### KERF SURFACE APPEARANCE FOR EACH SAMPLE

Macrographs by multifocal optical microscopy


Surface quality evaluation is usually performed by the PAC system end users by means of **qualitative observation** of the kerf surface color related the physical properties of surface oxide layers but only few preliminary studies have been accomplished in literature concerning the effect of plasma cutting on stainless steels microstructure.

It is known that the thin **film interference effect** can influence the appearance of a semi-transparent oxide coating when the coating thickness is on the order of the wavelength of light incident on a specimen (400-700 nm for visible light). In particular, constructive interference is likely to occur when the oxide thickness is equal to $\lambda/4n$ where $n$ is the index of refraction for the oxide.

Apparently, **the use of plasma cutting gas rich in nitrogen gave rise to darker surfaces** (A and F). Sample F showed in particular a completely dark appearance, possibly related to the presence of a thicker oxide layer also due to the lower cutting speed and consequent prolonged heating of the kerf surface. Oxidation is due to the entrained ambient air.

## SURFACE COMPOSITION BY LARGE AREA EDS ANALYSIS

| AISI 304L nominal composition (wt. %) | | | | | | | | |
|---|---|---|---|---|---|---|---|---|
| C | Si | Mn | P | S | Cr | Ni | Co | N |
| 0.018 | 0.32 | 1.61 | 0.029 | 0.001 | 18.3 | 8.1 | 0.13 | 0.07 |

| | Sample | | | |
|---|---|---|---|---|
| Element (wt. %) | A | B | C | F |
| C | - | 8.4 | 7 | 8.2 |
| N | - | 6.1 | - | - |
| O | 13.4 | 5.4 | 13 | 21.3 |
| Si | 1.0 | 0.6 | 0.4 | 0.2 |
| Cr | 16.3 | 16.2 | 15.6 | 13.3 |
| Mn | 2.2 | 1.8 | 1.9 | 6.9 |
| Fe | 59.6 | 54.7 | 55.7 | 37.7 |
| Ni | 7.5 | 1.5 | 6.7 | 6.4 |
| Other | - | 0.8 | 0.2 | 0.2 |

Surface composition was generally found to **be rich in oxygen**, with weight ranging between 5.4% for sample B and 31.3% for sample F.

The **higher level of oxidation** of sample F is caused by the lower cutting speed that increases the plasma residence time and the material overheating. It is important to limit the presence of oxide on the kerf surface to guarantee its weldability, as the presence of oxide inclusions would compromise the joint quality and strength.

A **high content of atomic N** (6.1 wt. %) was found on the surface of sample B, as a consequence of using a 70% $N_2$ rich plasma gas that seems also to **prevent surface oxidation**.

## CROSS SECTIONS OPTICAL AND SEM ANALYSIS

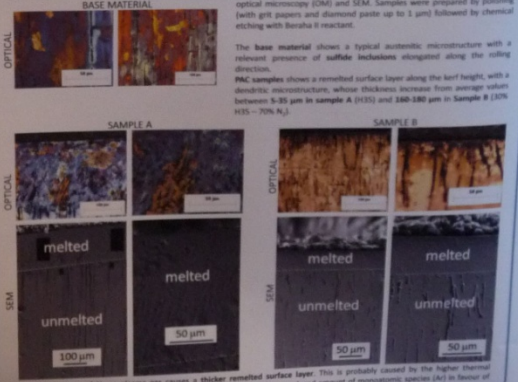


Microstructural characterization were carried on the cross sections by optical microscopy (OM) and SEM. Samples were prepared by polishing (with grit papers and diamond paste up to 1 µm) followed by chemical etching with Beraha II reactant.

The **base material** shows a typical austenitic microstructure with a relevant presence of **sulfide inclusions** elongated along the rolling direction.
**PAC samples** shows a remelted surface layer along the kerf height, with a dendritic microstructure, whose thickness increase from average values between **5-35 µm in sample A** (H35) and **160-180 µm** in **Sample B** (30% H35 – 70% $N_2$).

A **higher content of $N_2$** as plasma gas causes a **thicker remelted surface layer**. This is probably caused by the higher thermal conductivity and heat capacity of the sample B cutting mixture that has a reduced amount of monoatomic species (Ar) in favour of diatomic species ($N_2$ and $H_2$) with respect to sample A.

## SEM MICROGRAPHS

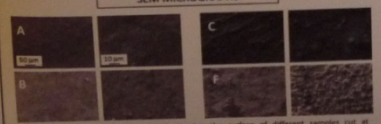


Scanning electron micrographs (SEM) showing the surface of different samples cut at different operating parameters. The surface was generally found to be **relatively smooth** except for the case of sample F.

## CROSS SECTIONS EDS ANALYSIS

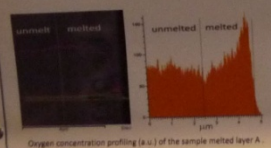


Oxygen concentration profiling (a.u.) of the sample melted layer A.

The oxygen content has **a peak near the kerf surface**, rapidly decreasing moving inside the workpiece. Although non-oxidizing gas mixtures were used in both A and B cases, this very thin (about 1 µm) oxide layer could form either during cutting, due to the entrance of atmospheric air in the arc column, or during the cooling phase of the kerf surface

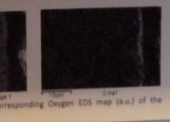

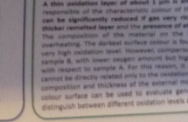

SEM micrograph and corresponding Oxygen EDS map (a.u.) of the melted layer in sample B.

## CONCLUSIONS

The effects of different Ar/H2/N2 plasma gas mixtures on the microstructural modifications of the AISI 304L stainless steel in high current (400A) plasma cutting has been investigated experimentally.
**The kerf remelted layer is proportional to the heating capacity of the plasma cutting gas mixture**. A higher percentage of diatomic species ($N_2$ and $H_2$) increases the deepness of the layer for samples A and B from 5 to 180 µm.
**A thin oxidation layer of about 1 µm is always formed on the kerf surface** and it is responsible of the characteristic colour of the surface. **The amount of atomic oxygen can be significantly reduced if gas very rich in N2** is used with the drawbacks of a **thicker remelted layer** and the **presence of atomic nitrogen** on the surface.
The composition of the material on the kerf surface is strongly affected by the overheating. The darkest surface colour is found for sample F that is characterized by a very high oxidation level. However, comparisons between samples A and B shows that sample B, with lower oxygen amount but higher nitrogen content, has a darker colour with respect to sample A. For this reason, it can be concluded that the surface colour cannot be directly related only to the oxidation level, but more generally to the chemical composition and thickness of the external modified layer. A qualitative analysis of the colour surface can be used to evaluate general overheating but is not sufficient to distinguish between different oxidation levels and remelted layer thickness.

# Distribution of Driving Force in Weld Pool Affected by Temperature near Anode in Pulsed Arc Welding with Iron Vapor

Yasunori Goto, Toru Iwao, Motoshige Yumoto (Tokyo City University)

## Introduction

**Arc welding technology**

Widely used as **metaled junction** technology

**DC-TIG-Welding** (Direct Current Tungsten Inert-Gas)

High-quality joining technology

➢ Used for various construction with **reliability well**

Nuclear power and Petrochemical industry…etc

**★Disadvantage**

✓ Current is limited (For Electrode protection)

- **Deflection of Arc**
- **Low heat flux to Anode**

➢ **Shallow depth** and **Uneven** weld penetration

✓ **Weld defect occurs**


**Improvement**

➢ **PC-TIG-Welding** (Pulse Current Tungsten Inert-Gas)

**★Advantage**

Pulsed current waveform

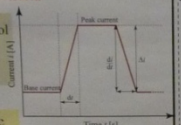


✓ Transient arc by the **parameter** control

- **High directional of Arc**
- **High heat flux to Anode**

Reason

High current density in pulsed arc

- **Because current area is small**
- **Pinch effect increase**

Necessary deeply weld depth in order to improvement

- High heat flux
- **Electromagnetic force is large**
  (It is a kind of ***driving force***)

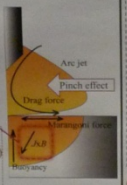


- Marangoni effect (radial direction)
- Electromagnetic force (axial direction)
- Drag force
- Buoyancy

**These driving forces affected by temperature near anode**

- Marangoni effect depend on graduation of temperature
- Current density depend on conductivity
  (**Conductivity** is as a function of temperature)

**Temperature of arc is reply transiently**

Including iron vapor
:conductivity increase

## Objective

**Distribution of Driving Force in Weld Pool Affected by Temperature near Anode in Pulsed Arc Welding with Iron Vapor is elcidated.**

## Research model

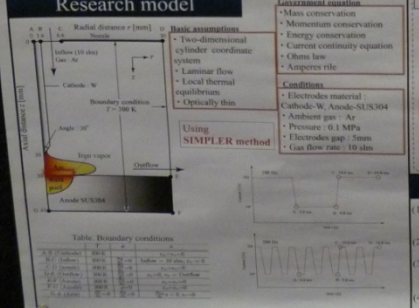


**Basic assumptions**

- Two-dimensional cylinder coordinate system
- Laminar flow
- Local thermal equilibrium
- Optically thin

Using **SIMPLER method**

**Government equation**

- Mass conservation
- Momentum conservation
- Energy conservation
- Current continuity equation
- Ohms law
- Amperes rile

**Conditions**

- Electrodes material : Cathode-W, Anode-SUS304
- Ambient gas : Ar
- Pressure : 0.1 MPa
- Electrodes gap : 5mm
- Gas flow rate : 10 slm

Table. Boundary conditions

## Results and Discussion

The points at A and B are the base current.
The points at C and D are the peak current.

### Temperature near anode

In the case of **100 Hz**

The temperature at radial center at point A and B are almost same to be 6000 K

In the case of **500 Hz**

the temperature at radial center is to be 7000 K at A and 6000 K at B.

**In the case of pulsed arc…**

**The temperature of arc cannot catch up the dI/dt to peak current**

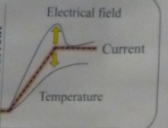


Because arc velocity is different

| 100Hz | 500Hz |
|---|---|
| 90.3ms | 93.6ms |

high temperature medium neat the cathode transports neat the anode.

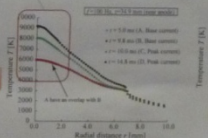


Fig.Temperature near anode ($f$=100 Hz)

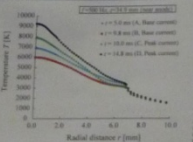


Fig.Temperature near anode ($f$=500 Hz)

### Current density

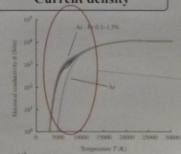


Temperature decrease

Electrical conductivity σ decrease (because σ is as s fuction of temperature)

Constricted of current path *S*

*J=σE:*

Maintain of current continuation

Current is concentrated in the center axis of the high electric field

Current density of the central part increase

**However**

Conductivity in the case of Ar-Fe is high than the one in the case of pure Ar !

The current density is same distribution which does not depend on the frequency and before or after current transition

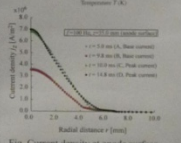


Fig. Current density at anode surface ($f$= 100 Hz)

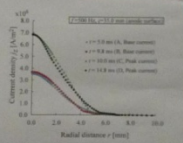


Fig. Current density at anode surface ($f$= 500 Hz)

### Distribution of driving force

**Radial direction of driving force**

- Marangoni effect : depend on temperature
- Electromagnetic force: depend on current density

**Axial direction of driving force**

- Electromagnetic force: depend on current density

The marangoni effect is 10 times as high as the electromagnetic force.

- In the case of 100 Hz,
  Radial positions which across the driving force to the radial direction are $r$=1.9 mm at point A and $r$=1.4 mm at point B-D
- in the case of 500 Hz
  they are less than those at $r$= 1.5 mm

almost same

The electromagnetic force distribution is almost same in the case of 100Hz and 500 Hz.

The maximum value is different with different frequency

**Pulsed arc ( Ar-Fe)**

Driving force at anode surface affected by temperature is almost same

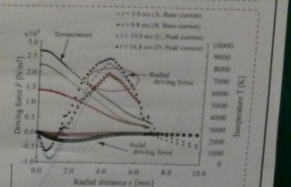


Fig. Driving force and temperature at anode surface ($f$=100 Hz)

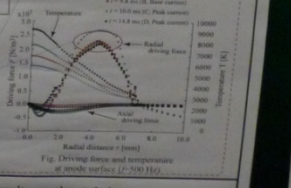


Fig. Driving force and temperature at anode surface ($f$=500 Hz)

## Summary

The main results are shown below.

(1) The temperature distribution of arc changes with changing the current waveform. Especially, it occurs in the case of the different frequency and transition to base current, because of plasma flow velocity difference.

(2) The current density distribution does not change so much with contamination of iron vapor, because the electrical conductivity increases with contamination of iron vapor, and it is easy to maintain the current continuity.

(3) The marangoni effect is 10 times as high as the electromagnetic force. However, the peak position of each distribution is different. The position of electromagnetic force > marangoni effect exits near the center part, the weld pool is expected to be better.

(4) The radial positions which across the driving force to the radial direction are almost same with any frequency, and the electromagnetic force distribution is almost same.

# HIGH-SPEED IMAGING INVESTIGATION OF TRANSIENT PHENOMENA IMPACTING PLASMA ARC CUTTING PROCESS OPTIMIZATION

Marco Boselli[1], Vittorio Colombo[1,2], Emanuele Ghedini[1,2], Matteo Gherardi[1], Fabio Rotundo[2] and Paolo Sanibondi[1]

[1] Department of Industrial Engineering (D.I.N.)
[2] Industrial Research Centre for Advanced Mechanics and Materials (C.I.R.I.-M.A.M.)
Alma Mater Studiorum-Università di Bologna
Via Saragozza 8, 40123 Bologna, Italy

ABSTRACT

In this work, we report high-speed imaging investigations of selected transient phenomena in plasma arc cutting (PAC) that induce wear of torch consumables, for different torch configurations. In particular, high-speed imaging sequences for the pilot arc start-up and shut-down phase have been analyzed for a 250 A automatic dual-gas torch equipped with electrodes with **different shape of the initial insert recess**, while the influence of **different insert materials**, including Ag-Hf and Cu-Zr binary alloys, was investigated at 120 A.

Also, we investigated the start-up and shut-down transients by high-speed imaging during torch operation in transferred arc mode on a graphite anode, by removing the shield cup and by using a modified nozzle characterized by the presence of **a viewing port at one side of the nozzle**. Moreover, results are presented concerning the effects of swirl flow during the pilot arc start-up phase and during the cutting phase in a 100 A mono-gas manual torch: the former must be investigated for the optimization of the torch operating conditions in terms of reduction of the wear rate of the nozzle internal surface, whereas the study of the latter can provide a deeper insight for the improvement of cut quality and the reduction of cathode erosion during the cutting phase.

SELECTED REFERENCES

[1] Boselli M, Colombo V, Ghedini E, Gherardi M, Rotundo F and Sanibondi P. "High-speed imaging investigation of transient phenomena impacting plasma arc cutting process optimization", Journal of Physics D: Applied Physics 46 (22), 224010, 2013
[2] Nemchinsky V A and Severance W S. "What we know and what we do not know about plasma arc cutting "Journal of Physics D: Applied Physics 39 R423-R438, 2006
[3] Colombo V, Concetti A, Ghedini E, Rotundo F and Dallavalle S. "Experimental analysis of the behaviour of high current electrodes in plasma arc cutting during first cycles", Plasma Sources Science and Technology 19 015008, 2010
[4] Rotundo F, Martini C, Gherardi C, Cucchini L, Concetti A, Ghedini E, Colombo V and Dallavalle S. "Plasma arc cutting: Microstructural modifications of hafnium cathodes during first cycles", Materials Chemistry and Physics 134 858-66, 2012

ACKNOWLEDGEMENTS

Funding from D.I.E.M./Cebora S.p.A. research contracts on project MIUR-DM.28562 (Art.1(88)Mo) is acknowledged. We acknowledge the contribution of S. Dallavalle, E. Frassoldi and M. Vancini of Cebora S.p.A. on the definition of the experimental set-up and operating conditions. We acknowledge Dr. Alessia Concetti who contributed to obtain part of the results reported in this work.

## EXPERIMENTAL SETUP


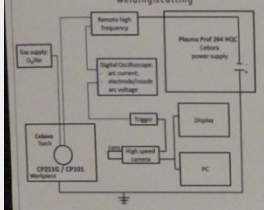


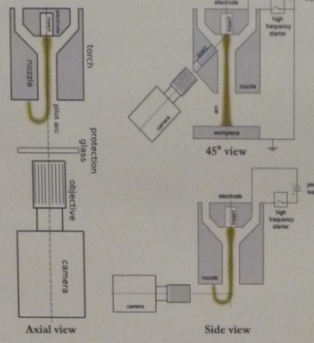


Nozzle orifice diameter: 1.9 mm; Electrode insert diameter: 2 mm; Pilot arc current: 25 A
High speed camera frame rate: up to 100,000 fps; Shutter time: up to 1/333,000 s

## SWIRL VELOCITY EFFECT ON ARC STABILITY (SIDE VIEW)

Single gas Cebora CP101 torch; Mild steel 20 mm thick plate
Air cutting 160 A; Diffuser with 8 holes 1,2 mm diameter
Problem to be solved: bad cutting performances

Diffuser 8x1.2 mm
High swirl velocity

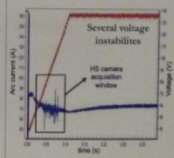


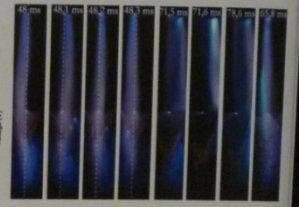


Unsteady arc, with low axial symmetry of the jet

Copper vapour emission
Double arcing phenomena

Diffuser 42x1.4 mm
Low swirl velocity

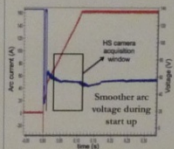


Solution: reduction of swirl by new diffuser
Diffuser with 42 holes 1,4 mm diameter
Effect: improvement in cutting quality


Good axial symmetry of the jet with constant arc width in time

## SHUT DOWN DURING PILOT ARC (AXIAL VIEW, CEBORA CP251G DUAL GAS TORCH)

New standard electrode with concave recess (depth 0,3 mm)

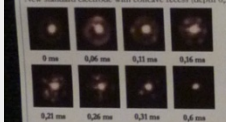


Standard Hf electrodes **with recess** on insert present massive droplet emission

Standard pure Hf insert

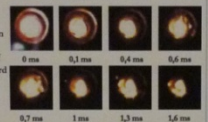


**Massive emission** of droplet from molten surface of insert with **standard electrodes**

New electrode with flat insert

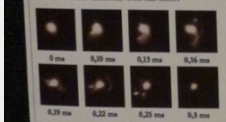


**Flat shape** of insert does not reduce droplet emission

Cu-Zr binary alloy

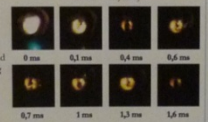


Cu-Zr insert material reduces droplet emission and **increases cooling of insert molten pool**

Used standard Hf electrode

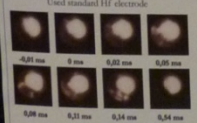


Droplet emission occurs even on **used electrode**

Ag-Hf binary alloy


**Ag-Hf avoids droplet emission** and further increases cooling of insert molten pool

## DIFFUSER EFFECT ON PILOT ARC BLOW-OUT (SIDE VIEW, CEBORA CP251G TORCH)

Diffuser with 6 holes, diameter 0.8 mm
Low swirl velocity, and high flow rate

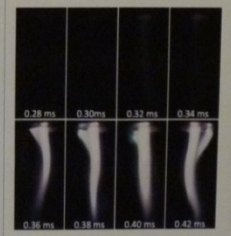


Fast pilot arc blow-out time

Diffuser with 3 holes, diameter 0.4 mm
High swirl velocity, and low flow rate


Slow pilot arc blow-out time

## BEHAVIOUR OF THE ARC INSIDE THE PLASMA CHAMBER DURING TORCH OPERATION IN TRANSFERRED MODE (45° VIEW, CEBORA CP251G TORCH)

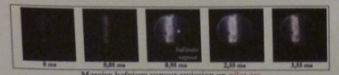


Massive hafnium vapour emission on pilot arc

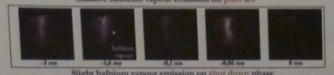


Slight hafnium vapour emission on shut down phase


Pulsing behaviour of the arc during start-up at a frequency of 7.7 kHz

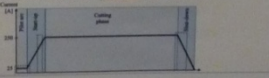


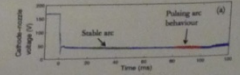


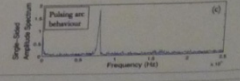


## INITIAL RECESS DEPTH DURING PILOT ARC START-UP TRANSIENT (AXIAL VIEW, CEBORA CP251G TORCH)

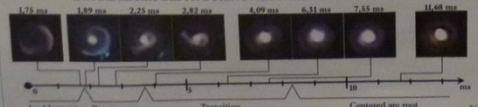


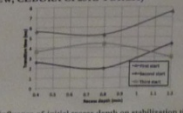


No influence of initial recess depth on stabilization time

CONCLUSIONS

- The **depth of the initial recess** of the emissive element in Hf electrodes does **not have influence** on the time required for the **stabilization of the arc** attachment on the center of the emitting surface during pilot arc start-up transient. These results suggest that the **transition time** is mainly **influenced by thermal properties** of the emitting material.
- **Binary alloy electrodes** have a pilot arc shut-down transient characterized by a **faster solidification** of the molten insert without massive emission of droplets from the liquid insert surface.
- High speed imaging of torch operation in transferred arc torch revealed **pulsing arc behaviour** inside the plasma chamber that is correlated with cathode-nozzle voltage oscillations at a frequency of 7.7 kHz.

# Plasmas assistés combustion & aérodynamiques

- **Hrabovki:** **Steam plasma assisted gasificationof organic waste by reaction with water, CO2 and O2**
- **H.X Wang** : Modeling study on the nonequilibrium expansion process of plasma arc through a nozzle
- **H.X Wang** : Modeling study on plasma flow and heat transfer of low power helium arcjet

# Steam plasma assisted gasification of organic wate by reaction with water, $CO_2$ and $O_2$

W. Hrabovski, M.Hlina, M.Konrad, V.Kopecky, O.Chumak, A.Maslani, T.Kavka, O.Zivny, G.Pellet
(IPP, Prague, Rep. Tchèque)

**Objectifs:** : traitement de déchets organiques, production de gaz de synthèse bilan énergétique du procédé de gazéification. Conversion du C en CO avec ajout $H_2O$, $CO_2$ et $O_2$

**Mots Clés:** plasma, gazéification, gaz de synthèse, plasma de vapeur

**Comment:** réacteur de 200L

**Expérience:**
Torche hybride DC stabilisée (vortex eau et gaz argon)
Création d'un plasma de vapeurs
En sortie, chute de la température à 300K
Vaporisation d'eau, filtrage et nettoyage en sortie
Le gaz produit est ensuite brulé
$I_{arc}$=400A, $P_{arc}$=115kW, rendement torche 60%
Gaz 0.45g/s, enthalpie moyenne 153MJ/Kg
Température de sortie 1900K

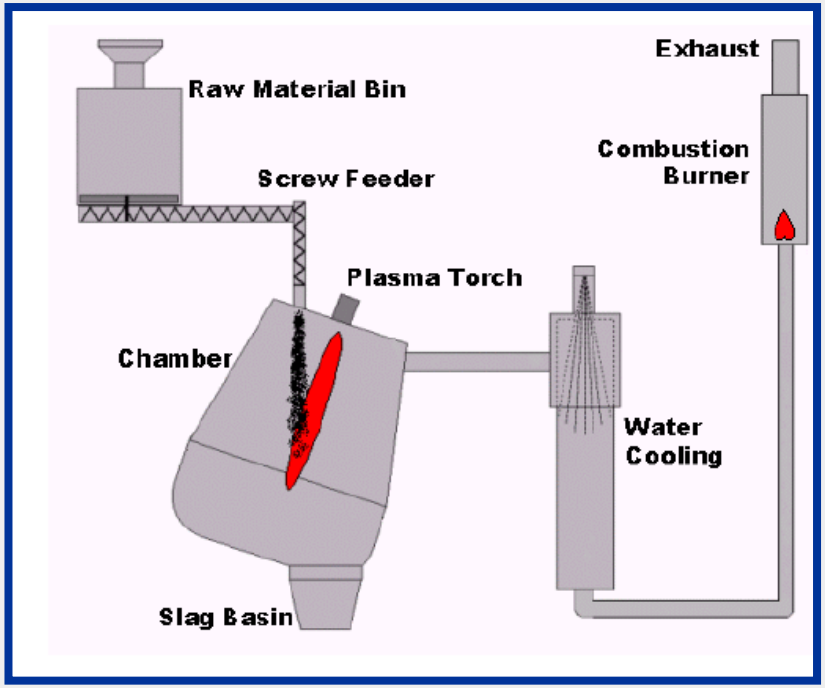


**Mesures:**
Températures, pertes dans le réacteur, composition gaz produit, analyse CO et $H_2$ en sortie par spectromètre

# Steam plasma assisted gasification of organic wate by reaction with water, $CO_2$ and $O_2$

W. Hrabovski, M.Hlina, M.Konrad, V.Kopecky, O.Chumak, A.Maslani, T.Kavka, O.Zivny, G.Pellet
(IPP, Prague, Rep. Tchèque)

**Resultats:** 30kg/h, 60kg/h pour la quantité de déchet traités, T° de 1200 à 1500K
Le changement du taux de déchet à traiter ne change pas la composition du plasma
Le changement de la taille des déchets ne change pas la composition du plasma
Bon accord avec les mesures expérimentales

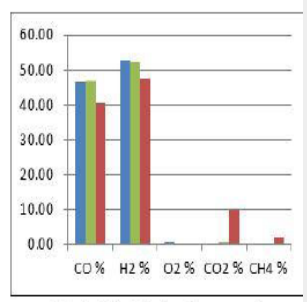


**Wood saw 30kg/h, $H_2O$, 70.4ml/min**

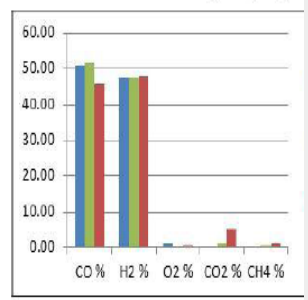


**Wood saw 30kg/h, $O_2$, 44.2slm**

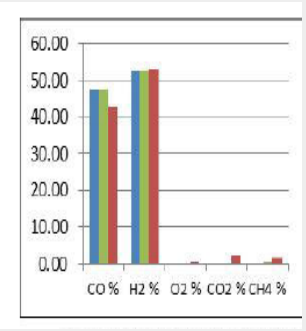


**Wood saw 60kg/h, $H_2O$, 140.8ml/min**

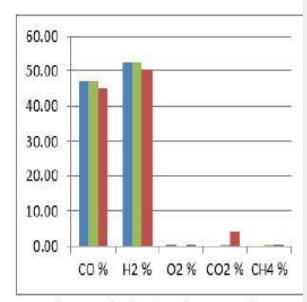


**Wood pellets 30kg/h, $H_2O$, 79.6ml/min**

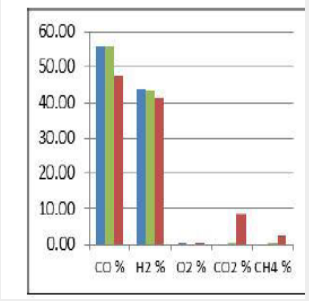


**Wood saw 30kg/h, $CO_2$, 85.4slm**

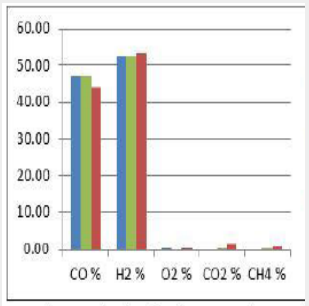


**Wood pellets 60kg/h, $H_2O$, 177ml/min**

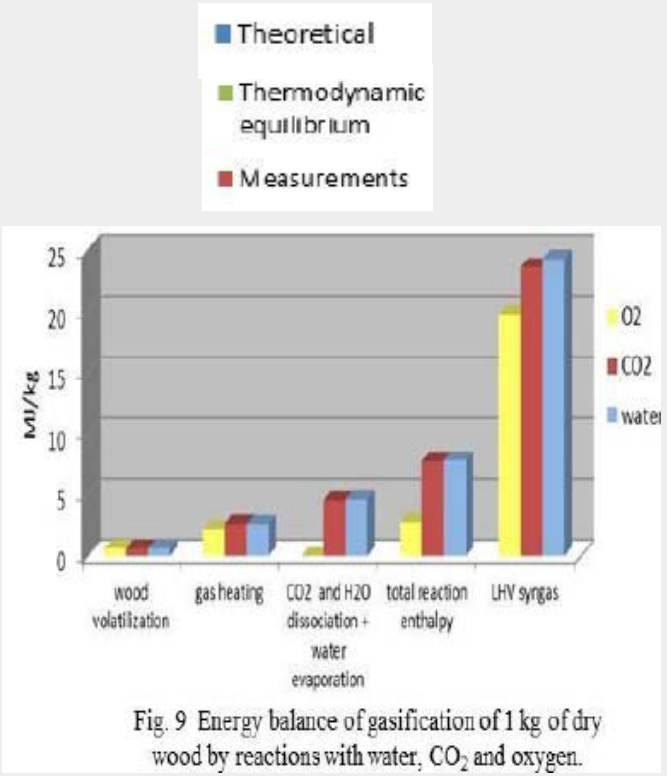


Fig. 9 Energy balance of gasification of 1 kg of dry wood by reactions with water, $CO_2$ and oxygen.

# Synthèse de nanoparticules

-**J.L Meunier**: **Homogeneous nucleation of graphene nanoflakes (GNFs) in a thermal plasma: Tuning the 2D nanoscale geometry**

- **M.Boselli: Modelling for the optimization of the reaction chamber in silicon nanoparticle synthesis by a RF-ITP**

- **E.Tam: 3D modelling of DC atmospheric arc discharges for carbon nanostructure production**

- **G. Soucis:** Synthesis of single-walled nanotube by induction thermal plasma technology using different catalysts

- **L.Fulcheri**: Synthesis of fullerenes from carbon powder in an entrained flow 3-phase AC plasma reactor operating at atmospheric pressure

**Présentation disponible**

# Homogeneous nucleation of graphene nanoflakes (GNFs) in thermal plasma: tuning the 2D nanoscale geometry

J.L Meunier, N.Y Mendoza-Gonzalez, R.Pristavita, D.Binny, D.Berk ( Montréal, Canada)

**Objectifs:** production de graphene nanoflakes pour PEM-FC (Polymer electrolyte membrane fuel cells). Étude de la géométrie du réacteur, débit des précurseurs de carbone injectés…

**Constat:** non seulement leur modèle permet de comprendre le contrôle et la synthèse de pure GNFs mais aussi de comprendre l'évolution de la structure 2D des nanoparticules.

**Comment:** Modèle de suivi et de contrôle de l'évolution des nanoparticules (longueurs, épaisseurs). Torche ICP qui permet un bon suivi et contrôle de la nucléation des nanoparticules, qui induit une bonne stabilité des propriétés des GNFs, haute cristallinité, fort dopage N.

**Modèle :**
ICP Torche 35kW, conique, 50cm de long, 14  angle d'ouverture
Fluent Ansys 14.5, 2D axisymétrique stationnaire

**Hypothèses:** Ar-$N_2$ + $CH_4$ injecté axialement, 14kPa<P<1atm, P=$C^{ste}$=10kW
Équation fluide + nucléation particule + modèle de croissance
Pas gravité, k-e turbulence, pas vapeurs condensées
Particules sphériques à la température du gaz
**PSD modèle:** Croissance, condensation, coagulation des particules ~4800k
Transport des particules par convection et diffusion
Elliptical Partial Differentieal equation (EPD) résolues

**Condi. Lim.:** 55kPa à l'entrée du réacteur, P=10kW
$10^{-3}$kg/kg fraction massique de vapeur de carbone
$T_{paroi}$=300K (refroidie par eau)
Transport et thermodynamique propriétés données par Boulos.
T~10000K dans les parties hautes de la torche

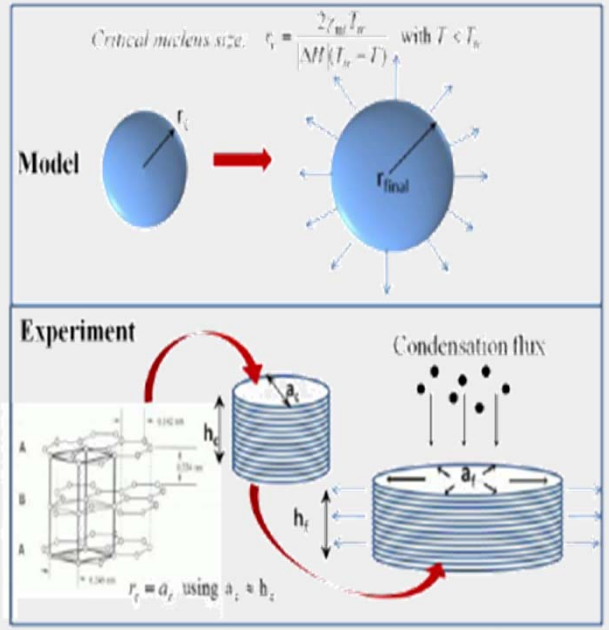

Fig. 1 Control for GNF morphology [2].

**Présentation disponible**

# Homogeneous nucleation of graphene nanoflakes (GNFs) in thermal plasma: tuning the 2D nanoscale geometry

J.L Meunier, N.Y Mendoza-Gonzalez, R.Pristavita, D.Binny, D.Berk ( Montréal, Canada)

**2 tests effectués:**

- 10kW, 7 , 55,3kPa, 10-3kg/kg (base)
- 10kW, 12 , 55,3kPa, 10-2kg/kg

La Température influence la taille finale des particules, la T diminue très vite, T de fusion du carbone proche de 3800K. La condensation est responsable de la taille finale des particules. On observe une croissance rapide le long des parois dès l'introduction du carbone. La T et les vitesses influence peu dans les régions de nucléation/croissance. Par contre elle modifie la structure 2D des GNF produits.

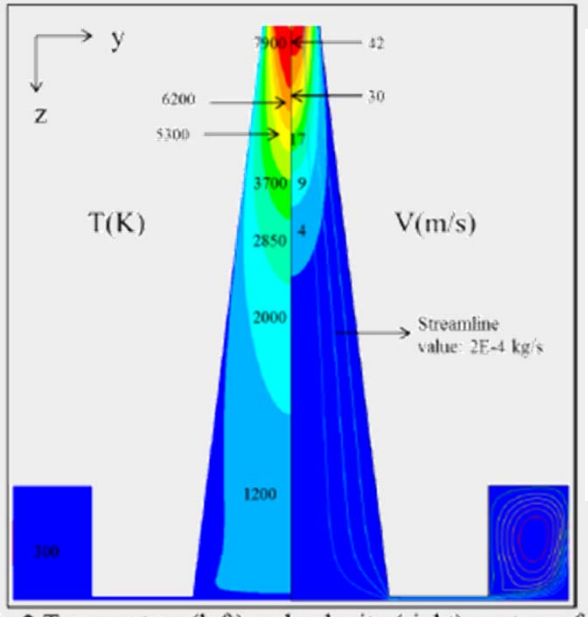


Fig.2 Temperature (left) and velocity (right) contours for the base case.

Table 2. Sumary of results

| | Base case | Angle expansion | Carbon increase |
|---|---|---|---|
| Angle exp. | 7° | 12° | 7° |
| Mass fract. [kg/kg] | $10^{-3}$ | $10^{-3}$ | $10^{-2}$ |
| **Residence times in 3000-5000 K range** | | | |
| Axis | 12 ms | 14 ms | 12 ms |
| Streamline $2E^{-4}$ | 14 ms | 19 ms | 14 ms |
| **Spherical diameter** | | | |
| Final size | 11nm | 15 nm | 19nm |
| **Lateral GNF growth** (# graphene layers for $h_f$) | | | |
| Thickness $h_f$ | 7 layers | 10 layers | 12 layers |
| Lateral size $a_f$ | 77 nm | 122 nm | 175 nm |

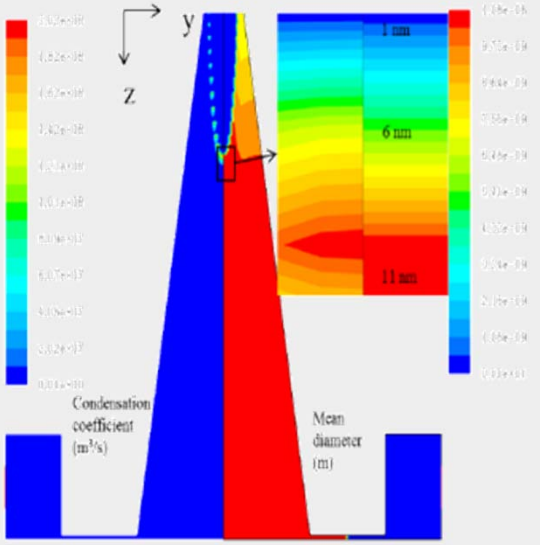


Fig. 3 Contours of condensation coefficient (left) and mean diameter (right) for the base case.

**Résultats:** des graphenes de 2-7mm d'épaisseurs (5-20 couches), 50-100nm de long, rectangulaire plan, 0.4g/30min..

# Modelling for the optimization of the reaction chamber in silicon nanoparticle synthesis by a radio-frequency induction thermal plasma

M. Boselli, V.Colombo, E.Ghedini, M.Gherardi, P.Sanibondi (Bologne, Italie)

**Investigation of silicon nanoparticles synthesis in the downstream region of a DC non-transferred arc plasma torch by three-dimensional modelling**

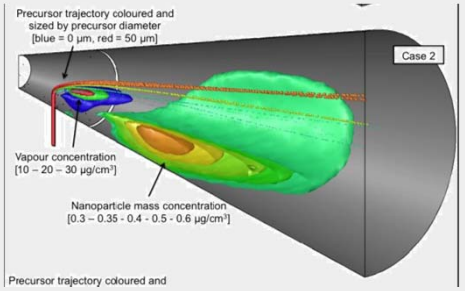


**Control of nanoparticle size in RF thermal plasma synthesis of silicon oxide starting from solid and liquid precursors**

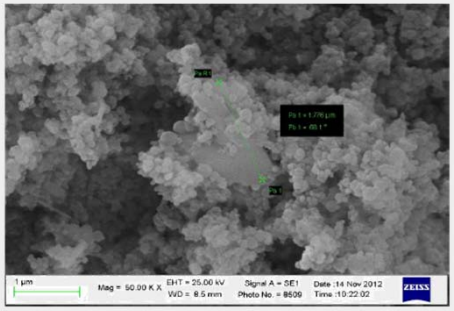

**Figure 3.** Crystalline particle in the sample of test 3A

**Evaluation of precursor evaporation in Si nano-particle synthesis by radio-frequency induction thermal plasmas**

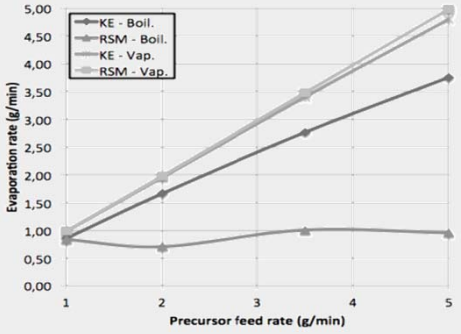


**Optimization of curtain gas injection position and flow rate in a conical reaction chamber for Si nanoparticle synthesis by inductively coupled thermal plasmas**

# Modelling for the optimization of the reaction chamber in silicon nanoparticle synthesis by a radio-frequency induction thermal plasma

M. Boselli, V.Colombo, E.Ghedini, M.Gherardi, P.Sanibondi (Bologne, Italie)

**Objectifs:** optimisation de la géométrie de la chambre d'un réacteur ICP : synthèse de nanoparticules en silicone.

**Mots Clés:** plasmas thermiques, synthèse de nanoparticules, modélisation

**Constat:** les procédés ICP semblent une solution pour la synthèse de nanoparticules de haute qualité. Haute densité, haute réactivité, haute pureté, plasma large et temps de vie long des particules. Tests avec des RF-ITP (induction thermal plasma). **Problème :** l'injection du gaz entraine une recirculation des flux qui forme des agrégats. Il faut donc contrôler le flux : test par une modélisation avec différentes géométries.

**Comment** modélisation avec tests sur 5 géométries (différents diamètres, différentes longueurs du cône)

**Modelisation:**

PL-35 Tekna plasma, 2D ANSYS Fluent, 10kW, 40kPa

**Gaz:** Injection en 3pts : pointe (6slpm, Ar), entre probe et tube quartz (12slpm, Ar), entre quartz et céramique (60slpm Ar + 6slpm $H_2$)

**Hypothèses:** Axisymétrique, LTE, coefficients diffusion combinés $ArH_2$ (Ar, $Ar^+$, $H_2$, H, $H^+$)

Equations classiques, turbulence (modèle k-epsilone), optiquement mince

Pertes radiatives : Ar pur, sans raies de résonance, sans influence des vapeurs sur les propriétés

Equations EMG jusqu'à 40mm hors torche

**Particules:** 10µm de diamètre, silicone, 6.5g/min

Trajectoire des précurseurs modélisée par approche Lagrangienne + évaporation précurseurs

Equation Advection-diffusion pour suivre les vapeurs des précurseurs

Méthodes MOM et nodal pour la nucléation et la croissance (coagulation, condensation)

General Dynamics Equation pour le transport des nanoparticules, utilisée pour les aérosols

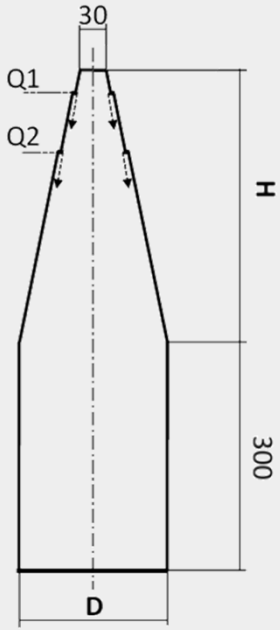

# Modelling for the optimization of the reaction chamber in silicon nanoparticle synthesis by a radio-frequency induction thermal plasma

M. Boselli, V.Colombo, E.Ghedini, M.Gherardi, P.Sanibondi (Bologne, Italie)

**Resultats:** la synthèse est affectée par la géométrie de la chambre et par l'injection des gaz additionnels.

**Localisation des régions de nucléation, de coagulation et de condensation**

## Sans injection de gaz (nucléation proche des parois du réacteur (A1,A3-A4), plus loin dans la chambre (A2, A5))

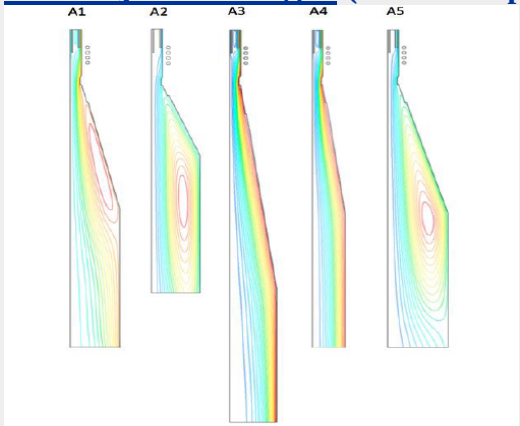


Fig. 2 Contours of stream function for cases without

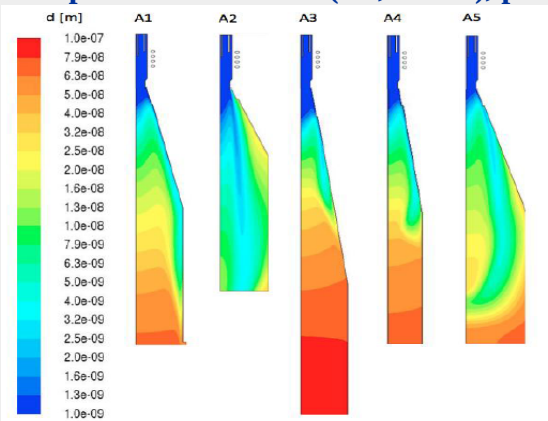


Fig. 3 Contours of nanoparticle mean diameter for cases

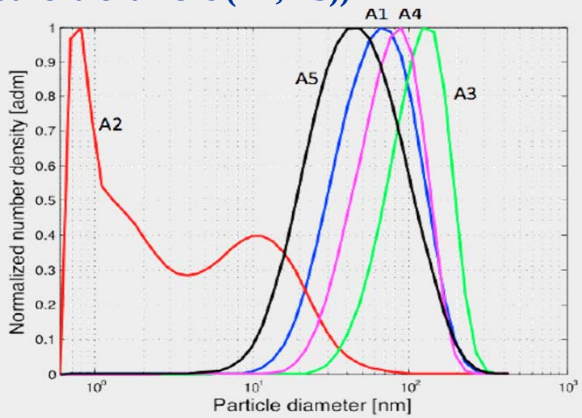


Fig. 4 Particle size distribution of nanoparticles on axial position at reaction chamber outlet. Cases A1-A5.

## Avec injection de gaz (nucléation proche des parois du réacteur (B1,B3-B5), plus loin dans la chambre (B2))

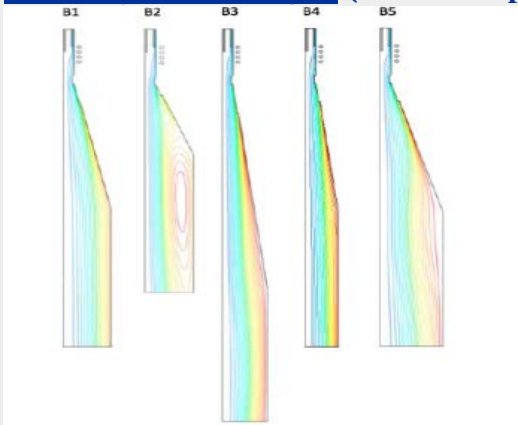


Fig. 5 Contours of stream function for cases with

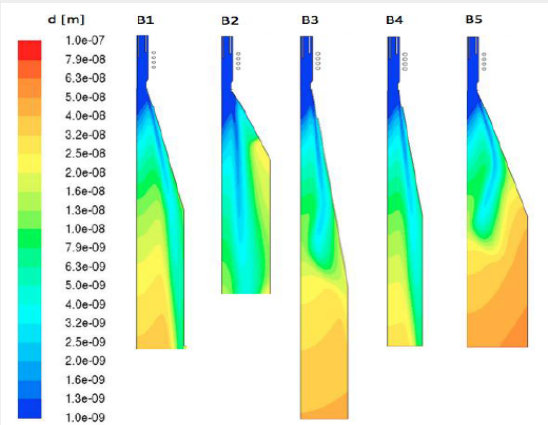


Fig. 6 Contours of nanoparticle mean diameter for cases

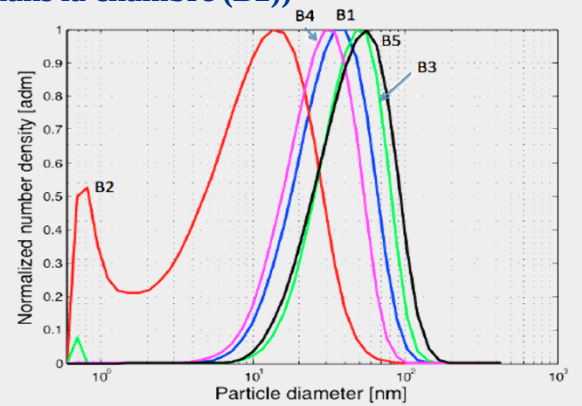


Fig. 7 Particle size distribution of nanoparticles on axial position at reaction chamber outlet. Cases B1-B5.

**Présentation disponible**

# Three dimensional modelling of DC arc discharges for carbon nanostructure production

E.Tam, A.B. Murphy (CISRO, Australie)

**Objectifs:** Production de nanotubes carbonés. Optimisation de la croissance et du rendement en étudiant le débit d'hélium, la distance inter-électrodes et le courant.

**Mots Clés:** arc, nanotubes de carbone, graphene, modèle, CFD

**Constat:** les décharges d'arc produisent de large volumes de nanostructures. Mais il reste encore à contrôler les gradients de température, optimiser le rendement, contrôler l'érosion des électrodes et la croissance des nanotubes (diamètre, cristallinité, chiralité..)

**Modèle:**
3D Patankar SIMPLER modifié
Électrodes en graphite, plongées dans un mélange He
$\phi c_{athode} = 2 * \phi_{anode}$
Fluide incompressible, LTE

**Equations classiques**
+ conservation des vapeurs de carbone
+ ablation et vaporisation du carbone
+ flux de vaporisation du carbone
+ flux déposé

**Cond. Lim.** aux électrodes données par Tanaka.
Coefficients de diffusion combinés

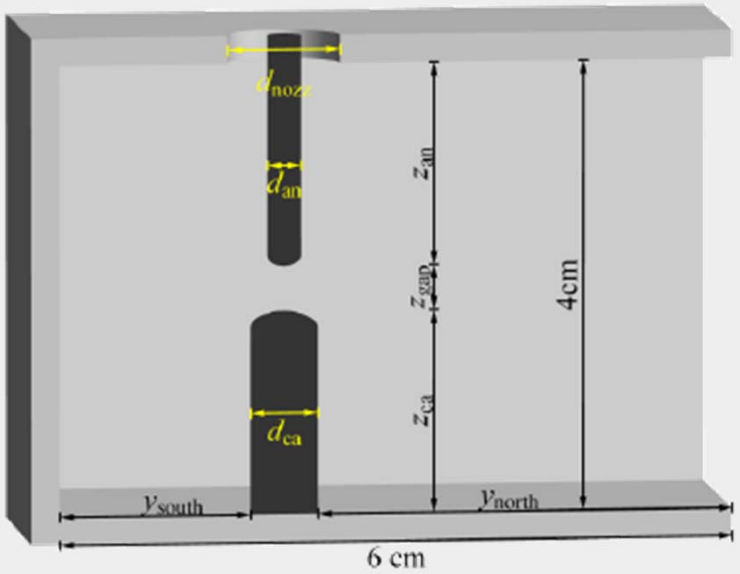


Figure 1: Schematic of the system modelled.

**Présentation disponible**

# Three dimensional modelling of DC arc discharges for carbon nanostructure production

E.Tam, A.B. Murphy (CISRO, Australie)

## Température sans ablation de carbone

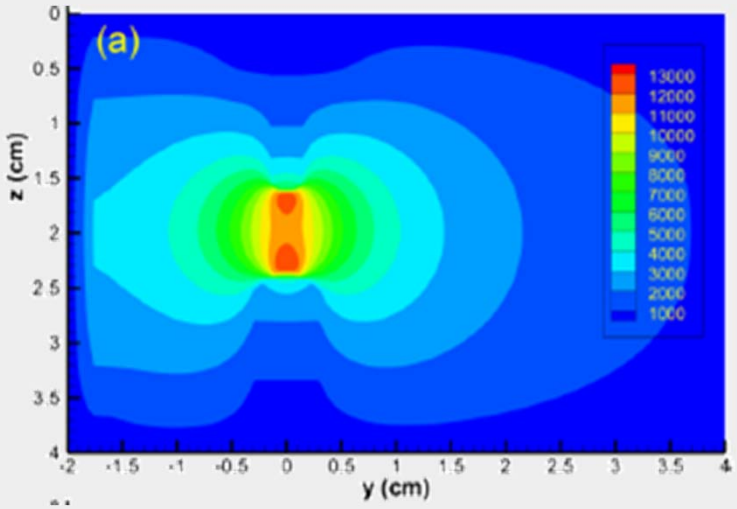


Distribution de la température selon z
Plasma contrôlé par les forces magnétiques
Remous et recirculations autour de l'arc

Température anode ~ 6000K

**Température ablation du graphite ~ 4000K**

## Température avec ablation et dépôt de carbone

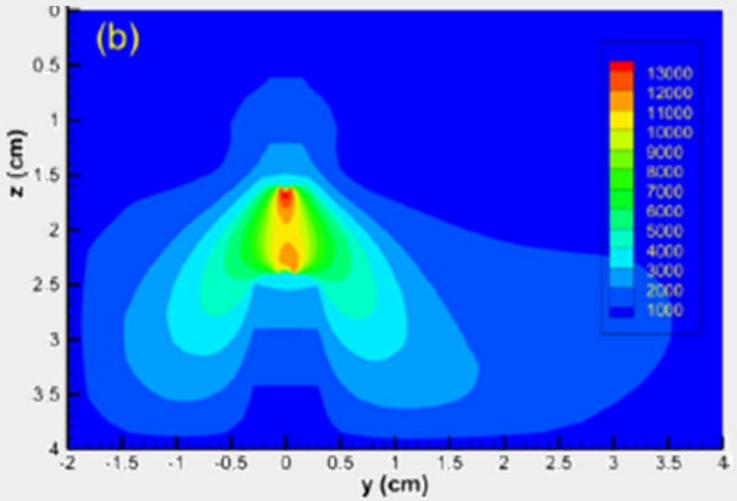


Cathode = émetteur thermoïonique
Cathode plus froide que l'anode à la surface
Plus forte ablation de l'anode
Plasma contrôlé par la croissance du carbone
Le taux d'ablation est une fonction exponentielle de la T
Température plus forte mais chute plus rapidement
L'arc semble plus constricté
Température des électrodes voisines de 4200K
Electrodes refroidies à cause de l'ablation

**Présentation disponible**

# Three dimensional modelling of DC arc discharges for carbon nanostructure production

E.Tam, A.B. Murphy (CISRO, Australie)

**Densité de masse (g/cm$^3$) du carbone 50A, 38.4L/min**

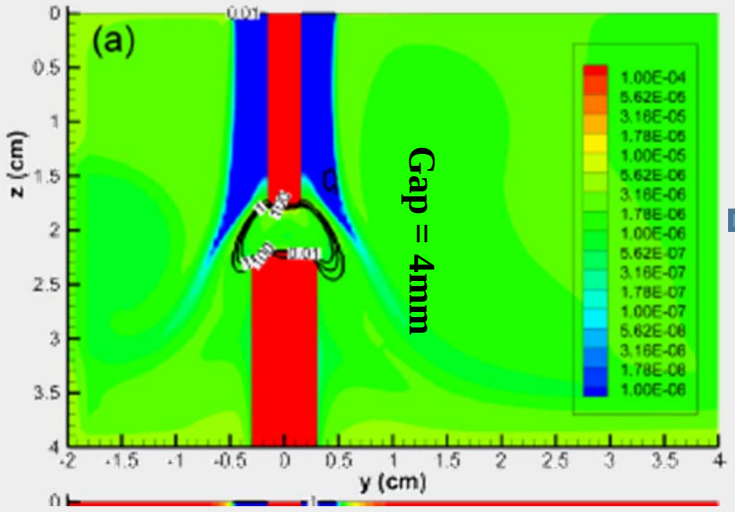


Région bleue : absence de carbone, là où entre He
Passage au vert: ablation du carbone
Isolines de saturation en carbone proches
Petites nanoparticules car faible condensation

Le courant total et le flux d'hélium influencent fortement la densité de masse et la saturation en carbone, affectant la taille des nanostructures.

**Densité de masse (g/cm$^3$) du carbone 200A, 2.4L/min**

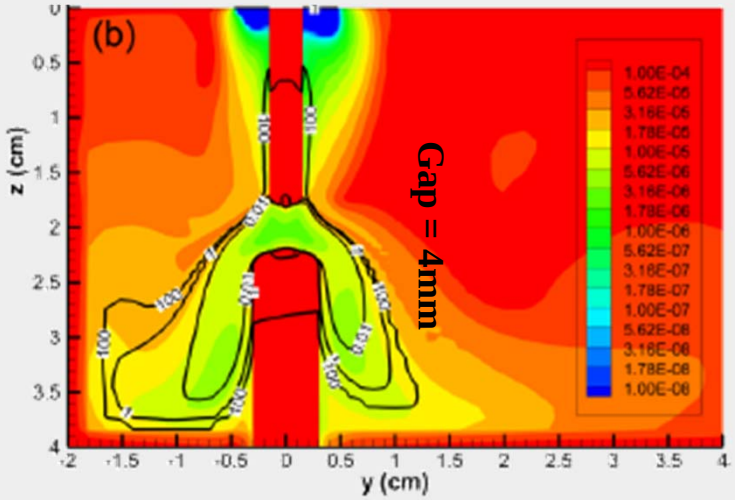


Fort courant = ablation rapide des électrodes
Augmentation rapide de la densité de masse du carbone
Isolines éloignées, nanostructures plus larges

La forte densité près des parois est due au refroidissement
du milieu (gaz dense), prise en compte des molécules $C_x$ dans le modèle.

5

# EVALUATION OF PRECURSOR EVAPORATION IN SI NANO-PARTICLE SYNTHESIS BY RADIO-FREQUENCY INDUCTION THERMAL PLASMAS

Vittorio Colombo[1,2], Emanuele Ghedini[1,2], Matteo Ghezzi[1], Paolo Sanibondi[1]

[1] Department of Industrial Engineering (DIN)

[2] Industrial Research Centre for Advanced Mechanics and Materials (C.I.R.I..M.A.M.)

Alma Mater Studiorum • Università di Bologna

Via Saragozza 8, 40123 Bologna, Italy

WWW.SIMBA-PROJECT.EU

## Abstract

The evaporation of micrometal silicon solid precursor in a laboratory scale radio-frequency inductively coupled thermal plasma reactor for nanoparticles synthesis has been investigated with the aim of increasing the production yield of the process, which is one of the most critical issues in making the technology successful on an industrial scale.

A plasma thermo-fluid-dynamic model coupled with a Lagrangian precursor particle tracking model has been implemented in the commercial CFD code ANSYS FLUENT® to gain a deeper insight on the evaporation process [1-3].

Different models that can considerably influence the estimation of vapour production have been investigated:

- Two turbulence models: standard k-ε or Reynolds Stresses Model
- Two models for particle evaporation: boiling or vaporization model.

## Thermo-fluid-dynamic and electromagnetic model

Continuity $\nabla \cdot (\rho \vec{u}) = 0$

Momentum $\nabla \cdot (\rho \vec{u}\vec{u}) = -\nabla p + \nabla \cdot \tau + \rho \vec{g} + \frac{1}{2} Re\left[\vec{J} \times \vec{B}^*\right]$

Energy $\nabla \cdot (\rho \vec{u} h) = \nabla \cdot \left(\frac{\lambda_{eff}}{c_p} \nabla h\right) + \frac{1}{2} Re\left[\vec{J} \cdot \vec{E}^*\right] - Q_r$

Species $\nabla \cdot (\rho \vec{u} Y_i) + \nabla \cdot \vec{J}_i = 0$

Vector potential $\nabla^2 A - i\omega\mu_0\sigma A + \mu_0 J_{ext} = 0$

### Turbulence models

**Standard k-ε (KE):**

Turbulent kinetic energy $\nabla \cdot (\rho \vec{u} k) = \nabla \cdot \left(\left(\alpha + \frac{\mu_t}{\sigma_k}\right) \nabla k\right) + G_k - \rho\varepsilon$

Dissipation rate $\nabla \cdot (\rho \vec{u} \varepsilon) = \nabla \cdot \left(\left(\alpha + \frac{\mu_t}{\sigma_\varepsilon}\right) \nabla \varepsilon\right) + C_{1\varepsilon} \frac{\varepsilon}{k} G_k - C_{2\varepsilon} \rho \frac{\varepsilon^2}{k} + S_\varepsilon$

where $G_k$ is the generation of turbulence kinetic energy due to the mean velocity gradients.

**Reynolds Stresses Model (RSM):**

Reynolds stresses $\nabla \cdot (\rho \vec{u} \overline{u_i' u_j'}) = \nabla \cdot (\mu \nabla \overline{u_i' u_j'}) + D_{T,ij} + P_{ij} + G_{ij} + \phi_{ij} + \varepsilon_{ij}$

where $D_{T,ij}$ represents the turbulent diffusion, $P_{ij}$ is the stress production, $G_{ij}$ is the production term due to buoyancy, $\phi_{ij}$ is the pressure-strain term and, finally, $\varepsilon_{ij}$ is the dissipation source.

**For both models:**

Dissipation rate $\nabla \cdot (\rho \vec{u} \varepsilon) = \nabla \cdot \left(\left(\alpha + \frac{\mu_t}{\sigma_\varepsilon}\right) \nabla \varepsilon\right) + C_{1\varepsilon} \frac{\varepsilon}{k} G_k - C_{2\varepsilon} \rho \frac{\varepsilon^2}{k} + S_\varepsilon$

$C_{1\varepsilon}$, $C_{2\varepsilon}$, $\sigma_k$ are constants; $f_\mu$ reduces turbulent dissipation in high-Y regions.

## Operating conditions

**FIXED parameters**

Gas flow rates [slpm]: Sheath: 60; Axial: 0; Plasma: 12; Carrier: 4.50

Pressure = 0.4 atm

Frequency = 13.56 MHz

**CASES have been investigated changing 3 parameters:**

Power couple to the torch (P)

Precursor mean diameter (d mean)

Precursor feed rate (F)

| P | d mean | F |
|---|---|---|
| 10 kW | 10 μm | 1, 2, 3.5, 5 g/min |
| 25 kW | 30 μm | 1, 2, 3.5, 7 g/min |
| 35 kW | 50 μm | 1, 2, 3.5, 7 g/min |

## Precursor particle size distribution

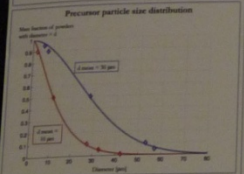


## 3D simulation of thermal and fluid-dynamic field

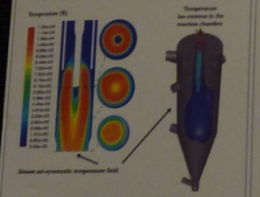


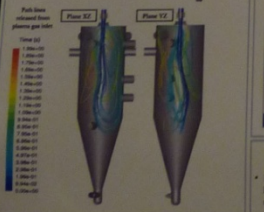


## "Cool" central channel induced by high feed rate


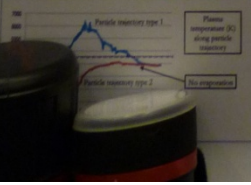



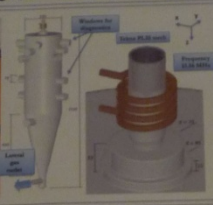


## Lagrangian precursor tracking model

Particle trajectory $\frac{d\vec{x}_p}{dt} = \vec{u}_p = \left(\frac{3\rho C_D}{4 d_p \rho_p}\right)(\vec{u} - \vec{u}_p)(\vec{u} - \vec{u}_p) + \vec{g}$

Heat flux to particle $q = A_p h_c (T - T_p) - A_p \varepsilon \sigma \left(T_\infty^4 - T_p^4\right)$

Particle heating $\frac{dT_p}{dt} = \frac{q}{m_p c_p}$

Particle cooling $\frac{dm_p}{dt} = \frac{q}{\rho_p c_p}$

## Precursor evaporation models

**Vaporization model**

mass transfer between the particle and the plasma starts when vapour concentration at the surface ($C_s$) < vapour concentration in the plasma ($C_\infty$)

Particle mass flux $\frac{dm_p}{dt} = -k_c (C_s - C_\infty)$

Particle heating $\frac{dT_p}{dt} = \frac{q}{m_p c_p} - \frac{\lambda_v}{m_p c_p} \frac{dm_p}{dt}$

**Boiling model**

mass transfer starts when the particle material reaches its boiling point

Diametric reduction $\frac{dd_p}{dt} = -\frac{2q}{\rho_p h_v}$

## Results

### KE-boiling model

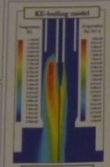

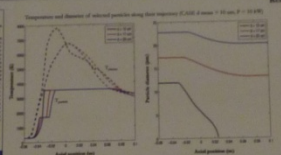


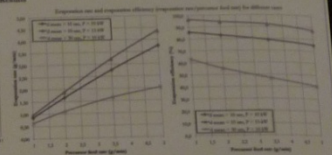


### RSM-boiling model

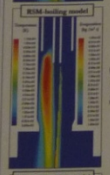

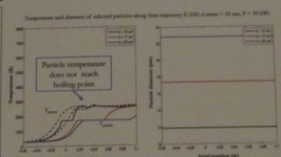


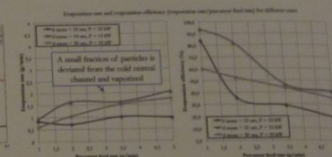


### KE-vaporization model

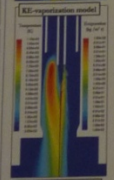

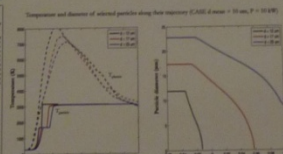


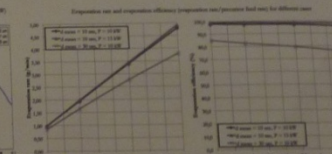


### RSM-vaporization model

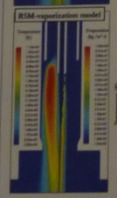

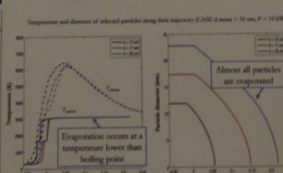


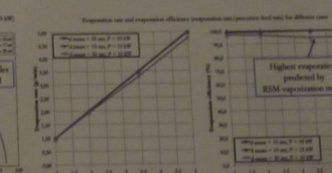


## COMMENTS:

- KE model induces a lower loading effect and a shorter plume with respect to RSM
- Boiling model predicts a lower evaporation rate with respect to vaporization model
- Very different precursor evaporation efficiencies are predicted with different models

## Comparison between different turbulence and evaporation models

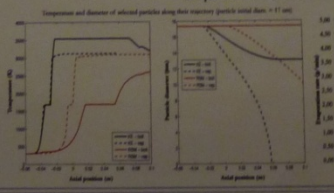


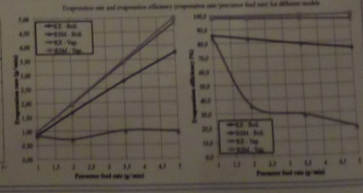


## Conclusions

It is shown that modelling of **precursor evaporation** in inductively coupled plasma torches depends strongly on the **choice of the turbulence and evaporation models** adopted.

Since plasma temperature along precursor trajectory is close to the boiling point of the treated material, **boiling model** predicts a lower evaporation rate than **vaporization model.**

Higher loading effect is predicted by boiling model than by vaporization model.

**Standard k-ε model predicts turbulent flow inside the torch:**
enhanced heat transport due to turbulence reduces the plasma cooling effects of high precursor loading conditions, resulting in higher evaporation efficiency.

**Reynolds Stress Model predicts an almost laminar flow inside the torch:**
loading effects are higher and temperature in the central channel is decreased below silicon boiling point. In combination with boiling model, the evaporation efficiency is strongly reduced.

## Selected references

[1] Colombo V, Ghedini E, Gherardi M, Sanibondi P "Evaluation of precursor evaporation in Si nanoparticle synthesis by radiofrequency coupled thermal plasma" Plasma Sources Sci. Technol. 21 045002 (2012)

[2] Colombo V, Ghedini E, Gherardi M, Sanibondi P "Modelling for the optimization of a silicon nanopowder synthesis reactor by a radio-frequency inductively coupled thermal plasma" Plasma Sources Sci. Technol. 23 045007 (2014)

[3] Colombo V, Concetti C, Ghedini E, Gherardi M, Jaroszyk P, Laurenzi S, Vicini V and Sanibondi P "Fluid-dynamic characterization of a radio-frequency inductively coupled plasma system for nanoparticle synthesis" Plasma Sources Sci. Technol. 23 045010 (2014)

# Synthesis of graphene-based conductive thin films by plasma-enhanced chemical vapor deposition in a $CO/H_2$ microwave discharge system

Department of Chemical Engineering,
Tokyo Institute of Technology

Youhei Anekawa, Shinsuke Mori and Masaaki Suzuki

## 1. introduction

**What is graphene ?**

⇒one layer of graphite consisting of $sp_2$ bonds

- very high conductivity in the room temperature
- high transmittance ranging from visible to infrared light

**Application for transparent conducting films**

example: solar panel and touch panel etc…

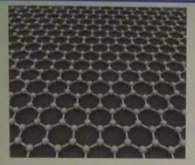

molecular model of graphene

**Problem in synthesis of graphene**

metal catalysis is necessary → transfer process is indispensable

⇒very complicated!! (coating of protection film→heating→removal of catalysis→separation→transfer→removal of protection film)

**We focused on carbon nanowall(CNW)**

**What is CNW ?**

⇒stacked graphene sheets standing vertically on the substrate (three-dimensional nanostructure)

- high conductivity
- possible to synthesize without any catalysts
- not transparent because of stacking

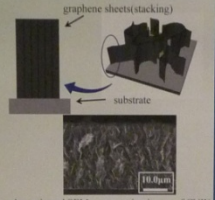


schematic and SEM cross section image of CNW

**<The purpose of this study>**

●synthesize graphene-based conductive thin film rapidly without any catalyst by decreasing of CNW layers

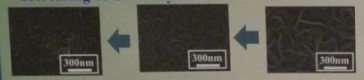


SEM surface image of CNW(left=thin, center=medium, right=thick)

✓decreasing of CNW layers
⇒ increasing of "wall" thickness
⇒decreasing of "wall" length

## 2. Experimental setup

**<MWPECVD apparatus>**

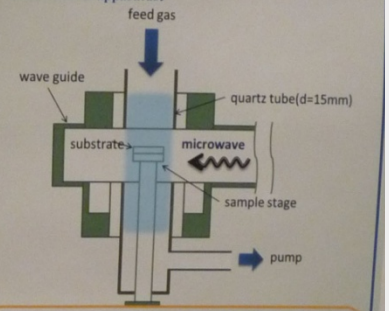


**<experimental condition>**

| | |
|---|---|
| substrate | quartz(9×9mm²) |
| sample stage | quartz(9×9mm²) |
| total flow rate | 50sccm |
| $CO/H_2$ flow ratio | 92%CO |
| pressure | 250Pa |
| input microwave power | 80W |
| deposition time* | 19s～60s |

*$CO/H_2$ flow ratio:

$$a\%CO = \frac{CO\ flow\ rate}{total\ flow\ rate}$$

*thickness of CNW layers
→controlled by deposition time

**<evaluation parameter>**

✓transmittance
→ uv-vis spectrometer

✓sheet resistance
→4-probe method

## 3. results and discussion

### 3-1. transmittance-sheet resistance curve

◆ base sample(typical CNW)

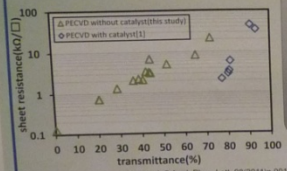


[1] Kim J. S Appl. Phys. Lett. 98(2011)p.091502

✓sheet resistance ∝transmittance

decreasing of deposition time
→high transmittance conductive film

✓measurement value is worse than reference

It needs improvement of film quality(crystalline)

change two parameters respectively
a. input power
b. $CO/H_2$ flow ratio

◆ a. change input power

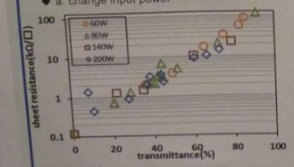


✓increasing input power
→sheet resistance is decreased at high transmittance.
reason: increment of substrates temperature

→independent at low resistance

◆ b. change $CO/H_2$ flow rate

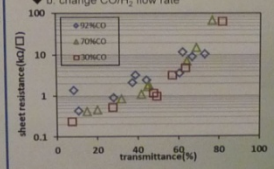


input power: 200W (because of a. result)

✓decreasing $CO/H_2$ flow ratio
→sheet resistance is decreased at low transmittance
reason: increment of $H_2$ etching effect for amorphous carbon removal

→independent at high resistance

### 3-2. emission spectroscopy

◆ b. change $CO/H_2$ flow rate

1.investigate each component in $CO/H_2$plasma

2.calculate the ratio of each component from the ratio of each intensity

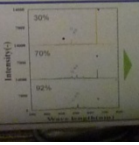


✓ component C2, CO, Hα, Hβ, Hγ were confirmed.

✓ the ratio of C2 to H are 0.08, 0.4 and 2.7 in 30%, 70% and 92%CO respectively

### 3-3. crystalline of films

●It is investigated by Raman spectroscopy to find the clue that improve film quality.

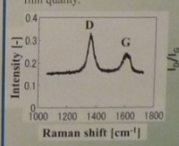


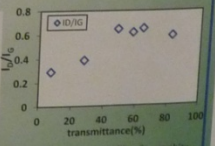


$I_D/I_G$ index of crystalline for graphitic

✓increasing transmittance → $I_D/I_G$ increased and reached constant.

the deterioration of films was proportional to transmittance but was independent at high transmittance region

### 3-4. early growth stage of CNWs

●It is observed by TEM to find out the reason of the independence of film quality at high transmittance.

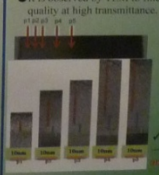

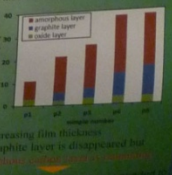


✓decreasing film thickness
→ graphite layer is disappeared but amorphous layer remained

crystallization of amorphous layer at early growth stage is needed to synthesize the higher performance transparent conductive film

### 4. conclusion

✓By optimizing input power and CO/H2 flow ratio, the low-resistance films were successfully synthesized without post-treatment.

✓Further high performance films need to promote the crystallization of amorphous layer at early growth stage.

# RF *inductively coupled thermal plasma synthesis of ceramic nanoparticles for the production of Al-based metal matrix nanocomposites*


**M. Boselli[2], L. Ceschini[1,2], V. Colombo[1,2], E. Ghedini[1,2], M. Gherardi[1], A. Morri[1,2], F. Rotundo[2], P. Sanibondi[1], S. Toschi[1]**

ALMA MATER STUDIORUM
UNIVERSITÀ DI BOLOGNA

*Alma Mater Studiorum – Università di Bologna, V.le Risorgimento 2, 40136 Bologna, Italy*
[1] *Department of Industrial Engineering (D.I.N.)*
[2] *Industrial Research Center for Advanced Mechanics and Materials (C.I.R.I.-M.A.M.)*


BUILDING OUR FUTURE TOGE

## SUMMARY OF THE WORK


The present study aims at testing the effectiveness of ceramic nanoparticles synthetized by means of RF thermal plasma technology for the production of Al-based nanocomposites (Al-MMNCs), evaluating the strengthening effects induced by their addition to the matrix. Ceramic micro and nanoparticles were produced using a lab-scale RF inductively coupled thermal plasma starting from micrometric raw solid precursors of the same material; process design has been assisted by simulation, as to optimize the plasma operating conditions and reactor geometry, in order to optimize quenching conditions during the nanoparticle synthesis process. Nanopowders samples were collected downstream the plasma reactor using a filter and successively characterized using BET analysis for specific surface area measurement and SEM-EDS microscopy for morphology and composition analysis. Samples of Al-MMNCs were prepared by stir-casting with ultrasonic treatment of the melt to enhance particle dispersion. The microstructure of cast MMNC samples was investigated by optical microscopy and SEM/FEG (Field Emission Gun)-EDS. Hardness tests were performed to assess the enhancement in mechanical properties induced by the addition of the ceramic micro and nanoparticles, with respect to the unreinforced A356 (Al-Si-Mg) matrix.


## SELECTED REFERENCES


V. Colombo, E. Ghedini, M. Gherardi, P. Sanibondi , Plasma Sources Sci. Technol. 21 (2012) 055007
V. Colombo, C. Deschenaux, E. Ghedini, M. Gherardi, C. Jaeggi, M. Leparoux, V. Mani, P. Sanibondi, Plasma Sources Sci. Technol. 045010
V. Colombo, E. Ghedini, M. Gherardi, P. Sanibondi, Plasma Sources Sci. Technol. 22 (2013) 035010
M. Boselli, L. Ceschini, V. Colombo, E. Ghedini, M. Gherardi, A. Morri, F. Rotundo, P. Sanibondi, S. Toschi, Cast Al-based nanoco reinforced with thermal plasma-synthesized ceramic nanoparticles, accepted at THERMEC 2013, Dec. 2-6, Las Vegas, US
D. Vollath, Plasma synthesis of nanopowders, Journal of Nanoparticle Research 10 (2008) 39-57
Hai Su, Wenli Gao, Zhaohui Feng, Zheng Lu, Materials and Design 36 (2012) 590–596
S.C. Tjong Adv. Eng. Mater. 9, No. 8 (2007) 639-652.
Yong Yang, Jie Lan, Xiaochun Li, Mater. Sci. Eng. A380 (2004) 378–383.
A. Mazahery, H.R. Baharvandi, H. Abdizadeh, Mater. Sci. Eng. A518 (2009) 23–27.
S.A. Sajjadi, H.R. Ezatpour, M. Torabi Parizi, Materials and Design 34 (2012) 106–111


## NANOPOWDER PRODUCTION AND CHARACTERIZATION

**Production: nanopowder synthesis by radio-frequency inductively coupled thermal plasma**

### How it works

- Injected precursor (solid microsized powders) is fully evaporated passing through high temperature plasma
- Quenched vapours are condensed in nanoparticles downstream the plasma jet

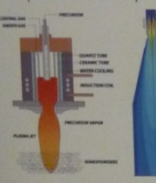

Schematic of the plasma process for nanopowder production

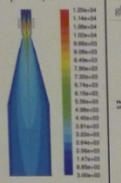

Temperature distribution in the plasma system (K)

### Plasma system at D.I.N. laboratories

- Lab-scale 35 kW - 3 MHz inductively coupled plasma system
- Feeding systems for gas/liquid/solid precursors
- Plasma reactor designed and optimized for nanoparticle synthesis through modelling
- Nanoparticle sampling system under controlled atmosphere in glove-box

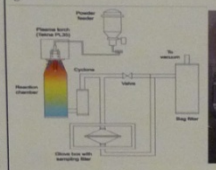

Schematic of the RF inductively coupled thermal plasma system for nanoparticles production

Plasma system during nanoparticle production

**Characterization: SEM-EDS analysis and specific surface area using BET technique**

| Characterization of the solid micrometric precursor: | Characterization of the produced μ-powders: | Characterization of the produced nanopowders: |
|---|---|---|
| •Specific surface area (BET) = 0.9 $m^2/g$<br>•Diameter from BET analysis = 2 μm<br>•Diameter from SEM analysis = 10-30 μm | •Specific surface area (BET) = 1.7 $m^2/g$<br>•Diameter from BET analysis = 0.9 μm<br>•Diameter from SEM analysis = 0.8-20 μm | •Specific surface area (BET) = 18 $m^2/g$<br>•Diameter from BET analysis = 80 nm<br>•Diameter from SEM analysis = 50-100 nm |
| • Element Atomic %:<br>• O: 67.42<br>• Al: 32.58<br>→ Pure $Al_2O_3$ micropowders | • Element Atomic %:<br>• O: 60.25<br>• Al: 39.75<br>→ Pure $Al_2O_3$ micropowders | • Element Atomic %:<br>• O: 69.67<br>• Al: 30.33<br>→ Pure $Al_2O_3$ nanopowders |

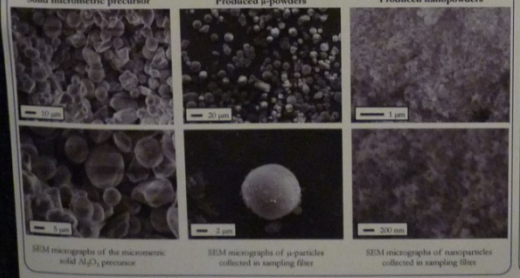


SEM micrographs of the micrometric solid $Al_2O_3$ precursor

SEM micrographs of μ-particles collected in sampling filter

SEM micrographs of nanoparticles collected in sampling filter

## COMPOSITE PRODUCTION AND CHARACTERIZATION

**Production: ceramic powder distributed in molten Al by stir casting and ultrasonic vibration**

### Production route

- $Al_2O_3$ particles and A356 (Al-Si-Mg) were mixed in a ceramic crucible (layer-feeding method) in the solid state.
- Al matrix is molten at 740 °C and mechanical stirring (MS) at 120 rpm is performed to improve particles dispersion.
- A Ti-based ultrasonic probe is pre-heated at 300 °C, then dipped into the melt at 730 °C.
- The melt is treated through ultrasonic vibration (US) for 3 min, at 20 kHz and 38 μm of vibrational amplitude
- Crucible is moved to a sand case for solidification.

| Sample | Matrix | Reinforcement (wt. %) | Treatment |
|---|---|---|---|
| A356 | A356 | - | - |
| A356_US | A356 | - | MS+US |
| 2-μ | A356 | 2% μ-$Al_2O_3$ | MS+US |
| 5-μ | A356 | 5% μ-$Al_2O_3$ | MS+US |
| 8-μ | A356 | 8% μ-$Al_2O_3$ | MS+US |
| 1-n | A356 | 1% nano-$Al_2O_3$ | MS+US |
| 1-n_3-μ | A356 | (1% n + 3% μ)-$Al_2O_3$ | MS+US |

Matrix: *A356 casting aluminum alloy*

| Element | Si | Mg | Cu | Ti | Fe | Mn | Zn | Al |
|---|---|---|---|---|---|---|---|---|
| wt% | 7 | 0.4 | 0.15 | 0.15 | 0.1 | 0.08 | 0.08 | Balance |

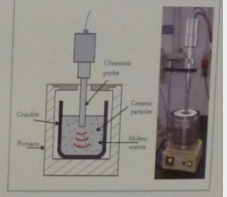


**Characterization: SEM/FEG-EDS analysis**

### A356/μ-$Al_2O_3$ composites

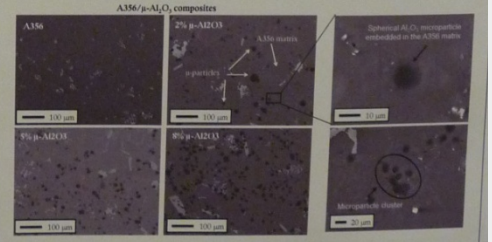


### A356/nano-$Al_2O_3$ composites

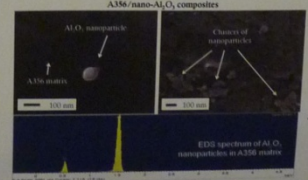


- SEM/FEG analyses showed the presence of micro and nanoparticles successfully dispersed within the A356 matrix.
- A good matrix-reinforcement adhesion was observed, without undesired brittle phases at the interface.
- Nanoparticle dispersion seems more challenging with respect to microparticles, due to their higher surface energy and tendency to agglomerate, leading to an increased number of nanoparticle clusters.

## HARDNESS MEASUREMENTS

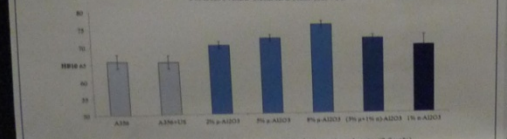


- Hardness increases proportionally to the μ-reinforcement content in the investigated range (2-8 wt%)
- 1wt% of n-reinforcement led to an hardness increase equal to that achieved with 2 wt% of μ-reinforcement

## CONCLUSIONS & FUTURE WORKS

- $Al_2O_3$ nanopowders have been produced starting from solid microsized precursor, using RF inductively coupled thermal plasma.
- Plasma produced micro (0.8-20 μm) and nanopowders (< 100 nm) are suitable for MMNC production.
- A356-based composites were produced by adding $Al_2O_3$ microparticles (ranging from 2 to 8 wt%), nanoparticles (1 wt%) and a combination of the two (1wt% n + 3wt% μ-particles).
- Both micro and nano-particles were successfully distributed through mechanical stirring and ultrasonic vibration in the Al molten matrix, although some nanoparticle clusters were found.
- The hardness increase, with respect to the unreinforced A356 matrix, was found to be proportional to the micro-reinforcement content, in the considered range (2-8 wt%). 1wt% of nanoparticle reinforcement led to an hardness increase equal to that achieved with 2 wt% of μ-reinforcement.
- Future works will be focused on the production of innovative and tailored nano-reinforcements, which will include functionalized oxide and metallic nanoparticles as well as carbon based nanomaterials (graphene, fullerenes, nanotubes) for the production of enhanced metal matrix nanocomposites.

# Autres POSTERS

# *Design and characterization of the linear atmospheric pressure DC ARC plasma source for flue gas treatment*

V. Valinčius, V. Grigaitienė, P. Valatkevičius

Plasma Processing Laboratory, Lithuanian Energy Institute, Breslaujos 3, LT-44403 Kaunas, Lithuania

## PLASMA SOURCES AND REACTORS

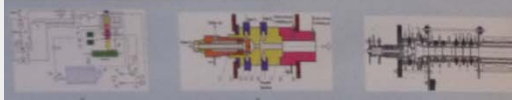

a b c

Schematic view of the experimental set-up (a) and plasma sources of different capacity: b – 90 – 120 kW, c – 1.5 – 2 MW.

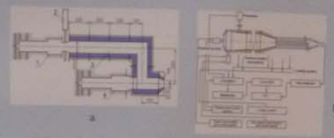

a b

Schemes of plasma chemical reactors. a – plasma jet reactor for flue gas treatment, b – for the treatment of hazardous substances

Plasma sources in operation. $P$ = 35–90 kW, arc current $I$ = 150–250 A, voltage $U$ = 200–350 V, total gas flow rate $G$ = 5–23 g s$^{-1}$. The working gas – air, argon, hydrogen, hydrocarbons, acetylene, water vapour.

## ATMOSPHERIC PRESSURE DC ARC PLASMA GENERATOR

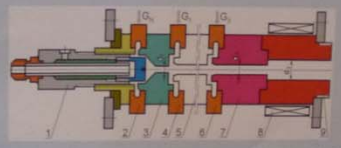

The schematic presentation of linear 50 kW DC PT. 1– cathode junction with hafnium emitter; 2, 4, 6 – insulating rings with gas injection; 3 – intermediate anode; 5 – neutrode; 7, 9 – step-formed anode; 8 – magnetic coil

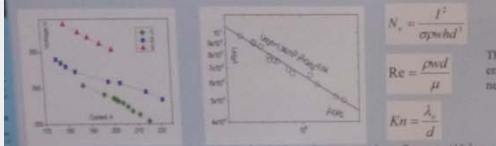

Plasma torch VCC with tangential air injection in dependence on total gas flow rate ($10^{-3}$ kg s$^{-1}$), respectively: 1 – 7.0, 2 – 8.0, 3 – 10.0

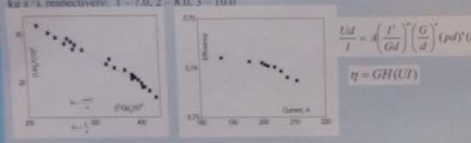

Generalized VCC with radial air injection at gas flow rate of (7.0 – 10.0) $10^{-3}$ kg s$^{-1}$

| | |
|---|---|
| Power, $P$ (kW) | 33-79 |
| Arc current, $U$ (A) | 175-245 |
| Arc voltage, I | 160-335 |
| Cooling water flow rate, $G_W$ (kg s$^{-1}$) | 0.16-0.18 |
| Water temperature increment (deg): plasma torch | 15-25 |
| cathode | 1.1-1.53 |
| ignition section | 1.08-2.16 |
| neutrode | 13.0-19.3 |
| anode | |
| Source gas flow rate (kg s$^{-1}$): cathode, $G_0$ | 0.54-1.0 |
| neutrode, $G_1$ | 1.85-7.6 |
| anode, $G_2$ | |
| Plasma jet temperature (K): average | 3460-5200 |
| max | |

| | |
|---|---|
| Plasma jet velocity, w (m s$^{-1}$) | 350-1000 |
| Efficiency, $\eta$ | 0.58-0.78 |
| Reaction chamber diameter ($10^{-2}$ m): $d_1$ | 4.0 |
| $d_2$ | 8.0 |
| $d_3$ | 12.0 |

## PLASMA DIAGNOSTICS

Plasma diagnostics. a – Calorimetric probe, b – Langmuir probe, c – temperatures of electron (1, 2) and heavy particles (3), d – velocity profiles in two-phase jet, e – non-dimensional enthalpies (1,2) and velocities (3), f – electron densities.

## SAMPLES OF THE DC PLASMA TORCH APPLICATION

Flue gas treatment

Biomass and fuels conversion in water vapour plasma

Reactions in presence of oxygen:

$C + O_2 \rightarrow CO_2 + 395.4$ MJ/kg

$2C + O_2 \rightarrow 2CO + 221.5$ MJ/kg

Boudouard reaction:

$CO_2 + C \rightarrow 2CO + 173$ MJ/kmol

Water shift reaction:

$CO_2 + H_2 \rightarrow CO + H_2O - 41$ MJ/kmol

Water steam reaction at 500–600 °C temperature:

$C + 2H_2O \rightarrow CO_2 + 2H_2 - 88$ MJ/kg

And at ~900 °C temperature:

$C + H_2O \rightarrow CO + H_2 + 130$ MJ/kmol

Catalytic coatings and catalytic converter

Micro- and nano-dispersed particles and fiber

Tribological coatings, deposited at different injection locations of dispersed particles into plasma jet: a – injection into the reactor, b – into the arc

Ceramic granules and mineral fibre

Plasma-sprayed $Al_2O_3$ granules and mineral fibre deposited at 2300 °C

Porous carbon coatings

Carbon films deposited at $Ar$+$C_2H_2$=100:1 at atmospheric pressure, a) d=0.005 m, b) d=0.01 m

## CONCLUSIONS

Generalization of characteristics based on the principles of dynamic similarity theory was found to be reasonable successful. The designed and manufactured PT is suitable for flue gas treatment in the system of thermal treatment of flue gas, hazardous substances and waste. The generalized electric and thermal characteristics of the PT permit determination of plasma flow parameters needed for plasma treatment of combustion products and selection of optimal operating modes.

The intensity of convection heat transfer in the plasma generator is directly proportional to the strength of the electric field. Heat transfer is most intense in the anode part of the plasma generator due to the arc spot and convection. In order to improve the efficiency of the plasma generator, it is necessary to reduce heat transfer by radiation between the electric arc and the PG anode walls.

The use of the non-equilibrium plasma technology demonstrates the ability to process wide range of waste substances and gases to obtain new products with specific structure and characteristics. Plasma technology allows the synthesis of catalytic, tribological and protective films, micro- and nanostructured particles, coatings and composites with controlled characteristics for specific applications.

# Coupling of high frequency oscillations in a non-transferred dc plasma torch

Jinwen Cao, Heji Huang, Wenxia Pan
*Institute of Mechanics, Chinese Academy of Sciences, Beijing, 100190, China*

## 1.Abstract

The coupling among high-frequency oscillations of arc voltage, arc current and cathode cavity pressure in a *non-transferred dc plasma torch with inter-electrode inserts* were observed experimentally. These oscillations co-occur with the same frequency of 4 kHz in an argon plasma. The oscillation of cathode cavity pressure is inspired by the input electric power when the electric power increases to a threshold value. And the relationship between the amplitudes of arc voltage oscillation and arc current oscillation is also obtained.

## 2. Experimental details

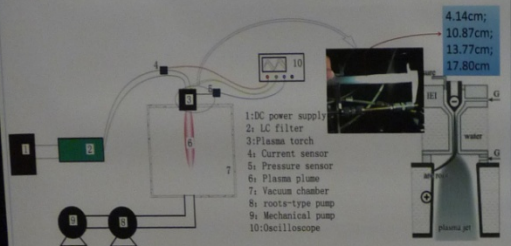


**Fig. 1.** schematic diagram of the experimental system and the plasma torch[1]

**Table 1.** experimental condition

| Gas | Gas flow-rate | Chamber pressure | Arc current |
|---|---|---|---|
| Pure Argon | 6 slm | < 500Pa | 80~120A |

The distance from pressure sensor to cathode cavity was varied with different length copper tubes to study the phase-shift phenomena between pressure and arc voltage, as shown in figure 1. *The distance varied among ζ+4.14cm, ζ+10.87cm, ζ+13.77cm and ζ+17.80cm.* ζ related to other parts of the pressure sensor and was constant.

## 3. Results and discussion

### (a) Coupling of arc voltage and cathode cavity pressure

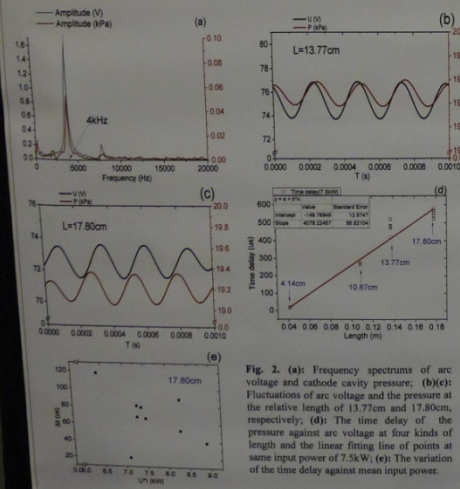


**Fig. 2. (a):** Frequency spectrums of arc voltage and cathode cavity pressure; **(b)(c):** Fluctuations of arc voltage and the pressure at the relative length of 13.77cm and 17.80cm, respectively; **(d):** The time delay of the pressure against arc voltage at four kinds of length and the linear fitting line of points at same input power of 7.5kW; **(e):** The variation of the time delay against mean input power.

The phase difference was changed with different tube lengths. The variation of time delay at the same length was mainly caused by variation of input power: larger the input power was, smaller the time delay was. The red hollow points are of 7.5kW and the slope of their linear fitting is 4078±89μs/m, corresponding to a propagating velocity of 245±5m/s, much lower than the acoustic velocity of argon in room temperature.

### (b) Coupling of arc voltage and arc current

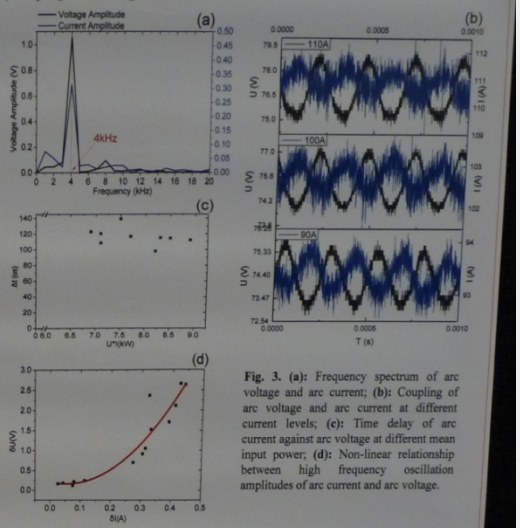


**Fig. 3. (a):** Frequency spectrum of arc voltage and arc current; **(b):** Coupling of arc voltage and arc current at different current levels; **(c):** Time delay of arc current against arc voltage at different mean input power; **(d):** Non-linear relationship between high frequency oscillation amplitudes of arc current and arc voltage.

The high frequency vibrations of arc current and arc voltage had almost inverse phase.

The time delay varied very slow with the mean input power comparing to that of the pressure, which probably means a different coupling mechanism.

A non-linear relationship between high frequency oscillation amplitudes of arc current and arc voltage were found, which indicates that the arc may have inductive or capacitive impedance.

### (c) Relationships of input power with arc voltage and cathode cavity pressure

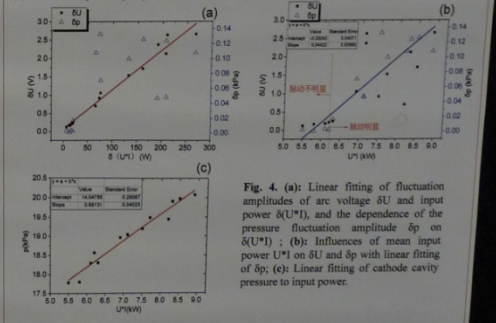


**Fig. 4. (a):** Linear fitting of fluctuation amplitudes of arc voltage δU and input power δ(U*I), and the dependence of the pressure fluctuation amplitude δp on δ(U*I) ; **(b):** Influences of mean input power U*I on δU and δp with linear fitting of δp; **(c):** Linear fitting of cathode cavity pressure to input power.

The pressure fluctuation amplitude δp was proportional to U*I other than δ(U*I), and the slope of fitting line is 0.0442Pa/W. When the mean input power was larger than some threshold value, 6.2kW in the experiments, those fluctuations started becoming obvious. The mean cathode cavity pressure varied linearly against mean input power with a fitting line slope of 0.691Pa/W, which was explained by [2]:

$$p = p_c + \frac{\gamma-1}{2\gamma}\frac{\dot{m}}{p_c s^2}(1+\alpha L)\cdot(U*I-P_w) \Rightarrow \frac{\delta p}{\delta(U*I)} = 0.691\,\mathrm{Pa/W}$$

$$\delta(pV^{\gamma}) = 0 \Rightarrow \delta p = -p\gamma_c\frac{\delta V}{V_0} = -\gamma_c\frac{s\cdot\delta l}{V_0}p \Rightarrow \frac{\delta(\delta p)}{\delta(U*I)} = -\gamma_c\frac{s\cdot\delta l}{V_0}\frac{\delta p}{\delta(U*I)} = 0.0442\,\mathrm{Pa/W} \Rightarrow \delta l = 0.97cm$$

$$\gamma_c = 1.67, s = 0.502cm^2, V_0 = 12.67cm^3$$

$\delta l$ is the amplitude of Helmholtz oscillation of plasma in channel.

## 4. Acknowledgement

This work is supported by the National Natural Science Foundation of China. (No. 11175226)

## 5.References

[1] Heiji Huang, Wenxia Pan, Chengkang Wu 2011 Plasma Chem Plasma Process **32**:65-74.
[2] J F Coudert, V Rat, D Rigot 2007 J.Phys. D: Appl. Phys. **40** 7357-7366.

# Modeling study on the nonequilibrium expansion process of plasma arc through a nozzle

Fu-Zhi Wei, Hai-Xing Wang, Wei-Ping Sun

*School of Astronautics, Beijing University of Aeronautics and Astronautics, Beijing 100191, China*
*(Corresponding author. E-mail: whx@buaa.edu.cn)*

## Abstract

A two-temperature thermal and chemical nonequilibrium model is applied to investigate the expansion processes of an argon plasma arc through a Laval nozzle. It is found that the plasma is far from thermodynamic equilibrium in the entire arc expansion process through a nozzle, especially in the cooler outer region. Although the number density of excited argon atoms ($Ar^*$) is much lower than that of other species in the argon plasma, $Ar^*$ plays an important role in the arc attachment to the anode.

**Keywords:** nonequilibrium, expansion, argon plasma arc, modeling study

Table 1 Chemical reactions considered in the model

| No. | Reaction | Rate coefficient $K_f$ | $\Delta E_f$ (eV) |
|---|---|---|---|
| 1 | $e + Ar \rightarrow e + e + Ar^+$ | $4.8\times10^{-19}T_e[eV]^{1/2}\exp\left(-\frac{11.81}{T_e[eV]}\right)$ $(m^3s^{-1})$ | 11.81 |
| 2 | $e + Ar^+ \rightarrow e + e + Ar$ | $4.8\times10^{-19}T_e[eV]^{1/2}$ $(m^3s^{-1})$ | -11.81 |
| 3 | $e + Ar^* \rightarrow e + e + Ar^+$ | $2\times10^{-14}\exp\left(-\frac{4.2}{T_e[eV]}\right)$ $(m^3s^{-1})$ | 4.33 |
| 4 | $Ar^* + Ar^* \rightarrow Ar^+ + Ar + e$ | $3\times10^{-16}\left(\frac{T_e[K]}{300}\right)^{1/2}$ $(m^3s^{-1})$ | 7.54 |
| 5 | $e + e + Ar^+ \rightarrow e + Ar^*$ | $8.75\times10^{-39}T_e[eV]^{-4.5}$ $(m^6s^{-1})$ | -4.33 |
| 6 | $e + Ar + Ar^+ \rightarrow Ar + Ar^*$ | $1.5\times10^{-43}\left(\frac{T_e[K]}{300}\right)^{-1.5}$ $(m^6s^{-1})$ | 4.33 |
| 7 | $e + Ar^+ \rightarrow Ar + h\nu$ | $2.174\times10^{-14}(T_e[K])^{-0.5}$ $(m^3s^{-1})$ | -15.76 |
| 8 | $Ar + Ar \rightarrow Ar^+ + Ar$ | $1.68\times10^{-16}T_e[K]^{0.5}(1+\frac{17500}{T_e[K]})\exp(-\frac{135000}{T_e[K]})$ $(m^3s^{-1})$ | 11.81 |
| 9 | $Ar^* + Ar \rightarrow Ar + Ar$ | $3.0\times10^{-17}$ $(m^3s^{-1})$ | -11.81 |

## Acknowledgment

This study was supported by the National Natural Science Foundation of China (No. 50936007, 11072029, 11275021).

## *Results and Discussions*


Fig. 1 Comparison of computed electron and heavy species temperature distributions in argon arcjet. (arc current: 8 A, mass rate: 115 mg/s )

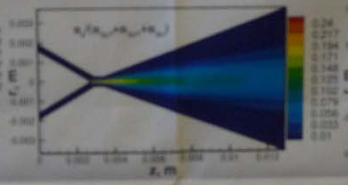


Fig. 3 Computed ionization fraction contours within the arcjet. (arc current: 8 A, mass rate: 115 mg/s )

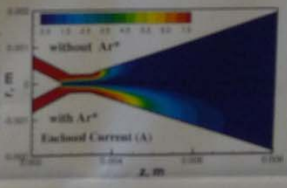


Fig. 5 Comparison of predicted enclosed current contours without and with the excited species within the arcjet. (arc current: 8 A, mass rate: 115 mg/s )

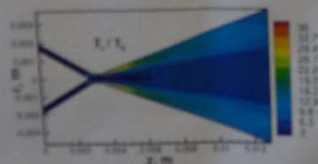


Fig. 2 Computed thermal nonequilibrium parameter ($T_e/T_h$) distribution in argon arcjet. (arc current: 8 A, mass rate: 115 mg/s )

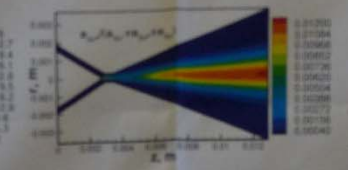


Fig. 4 Computed excited atom mass fraction contours within the arcjet. (arc current: 8 A, mass rate: 115 mg/s )

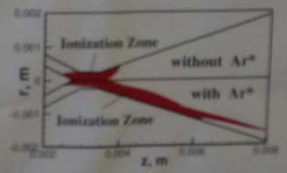


Fig. 6 Comparison of net ionization rate contours without and with the excited species within the arcjet. (arc current: 8 A, mass rate: 115 mg/s )

## Conclusions

A two-dimensional nonequilibrium plasma model has been employed to investigate the thermodynamic and chemical nonequilibrium characteristics of the argon plasma arc expansion through an arcjet nozzle. Numerical results show that considerable thermal nonequilibrium exists in the entire arc expansion process through a nozzle, especially in the near anode/nozzle wall region. The thermal nonequilibrium increases as the radial distance toward to the anode wall increases. Strong departures from excitation and ionization equilibrium are found in high-velocity plasma arc expansion processes. The ionization degree in arc core is about 0.24 in the constrictor of arcjet nozzle, much lower than that in chemical equilibrium. The role of excited species in the arc attachment on anode has been studied. It is found that the presence of the excited species promotes a diffuse type of attachment, extending the arc root further downstream, while the absence of excited species would lead to the formation of a constricted arc root on the upstream end of the nozzle. Although the number density of excited species of argon ($Ar^*$) is much lower than those of other species of the argon plasma, it plays an important role in determining the arc attachment mode to the anode.

# Collisional-radiative model of atomic hydrogen in high velocity plasma flow

Su-Rong Sun, Hai-Xing Wang*

*School of Astronautics, Beijing University of Aeronautics and Astronautics, Beijing 100191, China*
( *Corresponding author. E-mail: whx@buaa.edu.cn)

## Abstract

A collisional-radiative model is applied to investigate the physical kinetic processes of hydrogen plasma arcjet. The results show that in the constrictor region of arcjet, the electron impact excitation and ionization are dominant. In the downstream region of arcjet, it is found that electron impact de-excitation and recombination processes are dominant. For low lying excited states, radiative processes are very important, while for high lying excited states, electron impact processes are dominant.

**Keywords: collisional-radiative model, atomic hydrogen, high velocity plasma flow.**

## Results and discussions

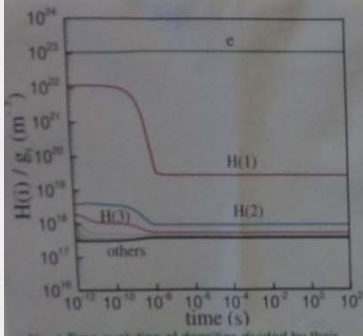


Fig. 1 Time evolution of densities divided by their statistical weight in the constrictor region of arcjet

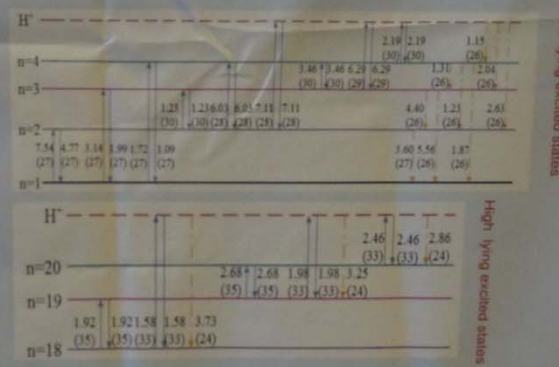


Fig. 3 Flows of electrons for low lying excited states and high lying excited states ($m^{-3}s^{-1}$). The straight arrows denote the non-radiative processes and the dashed arrows represent the radiative processes. The brackets denote the power of 10 by which the number should be multiplied ($t=1.0\times10^{-6}$ s)

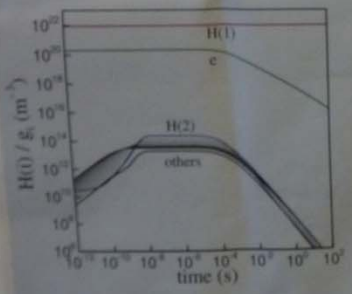


Fig. 2 Time evolution of densities divided by their statistical weight in the downstream region of arcjet

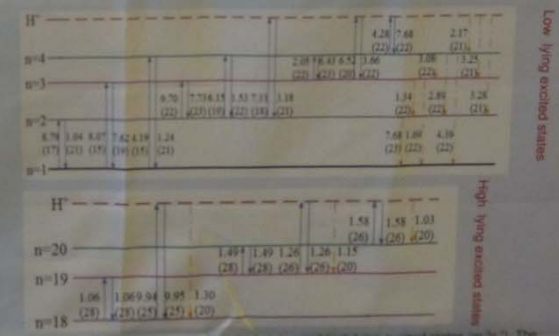


Fig.4 Flows of electrons for low lying excited states and high lying excited states ($m^{-3}s^{-1}$). The straight arrows denote the non-radiative processes and the dashed arrows represent the radiative processes. The brackets denote the power of 10 by which the number should be multiplied ($t=1.0\times10^{-6}$ s).

**Acknowledgment**

This work was supported by the National Natural Science Foundation of China (No. 10376001, 10535010, 10635070).

**Reference**

**A. Bultel, B. van Ootegem, A. Bourdon, et al., Physical Review E, 65, 046406 (2002).**

## Conclusions

A collisional-radiative model is applicable to hydrogen plasma arcjet thruster to investigate the kinetic processes in different regions of arcjet. It is found that in the constrictor region of arcjet the population densities of hydrogen excited states follow the Boltzmann distribution. The electron impact processes are dominant and radiative processes can be neglected. In the downstream region of arcjet, the electron impact deexcitation and recombination processes are dominant. The calculated population densities suggest low lying excited states deviate from Boltzmann distribution, while high lying excited states follow Boltzmann distribution. It is found that for ground state, spontaneous emission is dominant, while for low lying states, the electron impact deexcitation from adjacent states are dominant processes.

# ADAPTATION OF AN INDUCTIVELY COUPLED PLASMA FOR CHLORINATED ORGANIC LIQUID WASTES DESTRUCTION

S. FRANCOIS, G. KAMGANG-YOUBI, K. POIZOT and F. LEMONT

*French Alternatives Energies and Atomic Energy Commission – CEA Marcoule – DEN/DTCD/LPIC, F30207 Bagnols sur Cèze, France*

## ABSTRACT

The IDOHL (Installation for the Destruction of Organo-Halogenated Liquids) process has been specifically designed and patented ([1]) by the CEA to ensure the destruction of radioactive organic liquids thanks to inductively coupled plasma. In the original design ([2], [3]), liquid water, preliminary added to the organic waste, was used as oxidant agent. But, the destruction rate could be affected by problems of wastes miscibility or solubility in water. Moreover, the plasma energy spent to heat up and vaporize the liquid water increases the total energy consumption and decreases the maximum throughput. In order to improve the general performances of the process, liquid water has been replaced by O2 gas (dry or humidified) as oxidant agent in this study. Potential expected negative effect is the production of toxic chlorinated oxygenated gas (like phosgene (COCl2)), therefore the quality of the exhaust gases has been followed. The Chloroform ($CHCl_3$) has been chosen as model of organochlorine.

## Plasma general details

- High Tension : 5000V,
- High frequency : 64MHz,
- Electrical power : 4kW, around 2kW transferred as heat to the gas

→ Around 3500°K at the torch outlet

## Plasma generator details

- 7 turns copper coils, cooled down by air
- Plasma gas : Argon
- Several lighting systems tested

Original lighting system : point's effect (tungsten wire) :

In order to improve reliability and to avoid maintenance operations in radioactive internal area, an external system has been installed

Optimized lighting system : High Voltage spark :

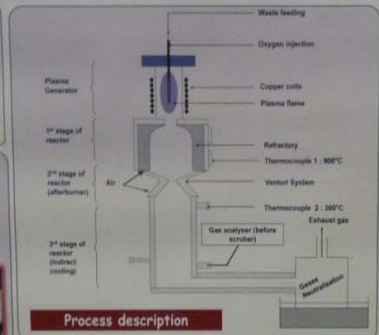


## Process description

## Injection probes

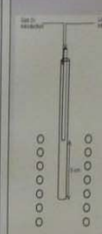

The probe is made of two alumina tubes. The internal tube for the liquid waste injection and the external one for the oxygen introduction. Water steam can be added to the oxygen up to 10%v. Inside tube is 5cm shorter, external tube end position is between the 5th and the 6th coil.

Good mixing between Oxygen and waste. The combustion starts in the lower part of the probe (hot area)

## Thermodynamic calculations for $CHCl_3$ oxidation

Equilibrium with dry oxygen as oxidant

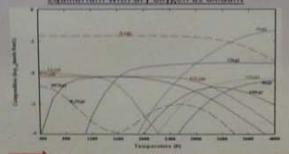

Equilibrium with humidified oxygen as oxidant

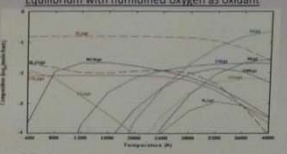

→ In both cases, the calculations show that the initial waste is fully decomposed at high temperature

## Experimental results Table

Summary Table: Gas analysis before the neutralisation device

| | PARAMETERS | | | | RESULTS | | |
|---|---|---|---|---|---|---|---|
| Oxidant | $CHCl_3$ feed rate ($g.h^{-1}$) | Initial $CHCl_3$ (ppm) | Ratio $O_2/CHCl_3$ | $O_2$ moisture (%) | Residual $CHCl_3$ (ppm) | HCl (ppm) | $COCl_2$ (ppm) |
| Dry Oxygen | 100 | 7128 | 20 | 0 | 35 | 2988 | 5 |
| | | 6648 | 30 | 0 | 2 | 2801 | 2 |
| | 200 | 12382 | 20 | 0 | 26 | 4655 | 13 |
| | | 11652 | 25 | 0 | 2 | 4710 | 8 |
| | 400 | 11003 | 30 | 0 | 1 | 4257 | 30 |
| | | 21747 | 15 | 0 | 1 | 7947 | 9 |
| | | 19408 | 20 | 0 | 1 | 7862 | 4 |
| Wet Oxygen | 100 | 7128 | 20 | 8 | 47 | 5426 | 11 |
| | | 7128 | 20 | 10 | 15 | 6180 | 28 |
| | | 6648 | 30 | 8 | 1 | 5184 | 15 |
| | | 6648 | 30 | 8 | 1 | 5837 | 30 |

The decomposition was performed with changing the $CHCl_3$ feed rate and the Oxygen quantity. Up to $400 g.h^{-1}$, if the Oxygen quantity is sufficient, the destruction rate of the chloroform is at least 99% with a conversion into HCl, $Cl_2$, $CO_2$ and $H_2O$.

To limit the formation of $Cl_2$, wet Oxygen was used and the conversion yield to HCl was around twice higher.

## Exhaust gases analysis : FTIR spectra

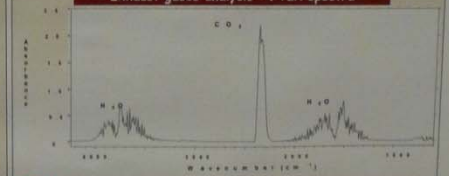


→ After the neutralization step, $CO_2$ and $H_2O$ are the main exhausted species

## CONCLUSIONS

- Up to $400 g.h^{-1}$ of the initial waste is fully decomposed, which gives 100g/kWh as energy efficiency, much higher than the 20g/kWh obtained in the previous study ([2]) when the liquid water was used as oxidant,
- The production of toxic chlorinated oxygenated gas, as phosgene $COCl_2$ is very low with less than $1 g.h^{-1}$, means at least ten times lower than the limit given by the french legislation ([4]).
- Even if it is possible to reduce the $Cl_2$ production by using humidified $O_2$, whatever the conditions the chlorinated gases are successfully trapped in the neutralization vessel,
- After remaining optimizations as external plasma lighting system, in order to limit difficult maintenance operations, the process can be installed in radioactive area, to test the destruction of actual wastes.

International Symposium on Plasma Chemistry

References

# Influence of plasma generation conditions on flow field of a plasma jet and particle in-flight behavior and oxidation in water-argon plasma spraying

T. Kavka, A. Mašláni, P. Ctibor, J. Matějíček

Institute of Plasma Physics AS CR, Za Slovankou 3, Prague 8, Czech Republic

## Motivation

- Plasma spraying is a prospective technology for production of plasma facing components of fusion reactors as it allows to coat large areas, even of complicated shapes, and to produce graded layers with varying composition.
- Tungsten, with its high melting point and low sputtering rate, can provide a plasma facing surface in a tokamak, where it will be subjected to large heat and particle fluxes and protect underlying components. Due to its refractory nature, it is challenging for the deposition process.
- Copper, with its high thermal conductivity, represents a suitable candidate for heat removal.
- Besides undergoing phase changes (melting in plasma and solidification after impact), the sprayed material may also experience chemical changes, e.g. oxidation for metals.
- Both materials have been sprayed by water stabilized plasma, which is characterized by high enthalpy and material throughput
- Process of particle oxidation was a subject of the research.

## Argon-water DC arc plasma torch and the spraying process

Arc current – 200 600 A
Arc power – up to 200 kW
Torch efficiency – 50 65%

Powder:
W – 63-80 μm, Cu – 100-125 μm
Powder feed rate:
- in-flight tests: W – 13.5 kg/h, Cu – 8.5 kg/h
- spray tests: W – 27.1 kg/h, Cu – 17.1 kg/h

Feeding distance: 25 – 60 – 90 mm
Carrier gas: Ar with 5.9 slm
Substrate: grid-blasted Cu and carbon steel

Diagnostics & Characterization
- plasma: OES
- particles: DPV-2000, $O_2$ content by inert gas fusion
- coatings: SEM, xenon flash method

## Properties of generated plasma

Plasma properties at the torch exit

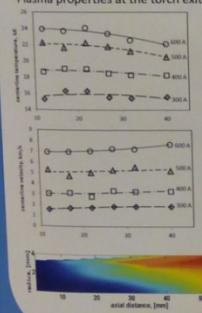

Total enthalpy of the generated plasma

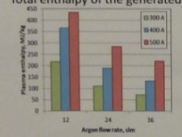

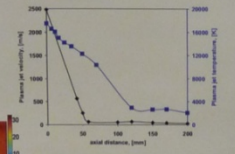

Air content in vol. % in plasma jet

Axial development of plasma jet: I = 300 A, Ar = 12.5 slm

## Particle in-flight behavior

Effect of plasma torch parameters on particle in-flight parameters (FD: W – 25 mm, Cu – 60 mm; Ar: green – 12 slm; black – 24 slm, red – 36 slm)

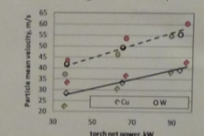

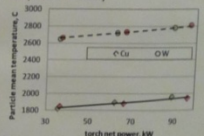

Characteristic correlation of particle mean temperature and velocity at SD = 320 cm

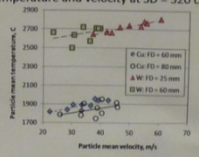

Oxide content in Cu particles collected in liquid nitrogen after flight through plasma (oxide in feedstock material – 0.41%wt.)

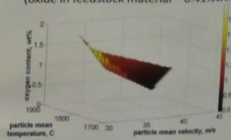

Typical splat morphologies: Tungsten Copper

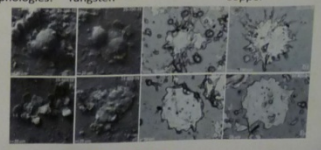

## Conclusions

Copper basic spraying parameters:

Feeding distance: FD = 90 mm
Arc current: I = 300 A
Argon flow rate: Ar = 36 slm
*Oxygen content:* $O_2$ = 1.06 wt%

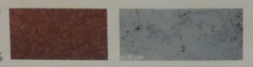

increase of current → I = 500 A

decrease of argon flow rate → Ar = 12 slm

decrease of feeding distance → FD = 60 mm

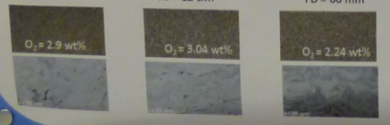


## Coatings

Effect of argon flow on coating properties

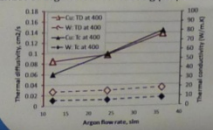

Oxygen content in Cu coatings

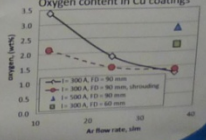

# *21th International Symposium on Plasma Chemistry*

*Cairns, Australie*, ***Août 4 - 9, 2013***